DEVELOPMENT OF LIQUID CRYSTAL BASED NANOPARTICLE SENSORS

A THESIS SUBMITTED TO
THE GRADUATE SCHOOL OF NATURAL AND APPLIED SCIENCES
OF
MIDDLE EAST TECHNICAL UNIVERSITY

BY

ASLI KARAUSTA

IN PARTIAL FULFILLMENT OF THE REQUIREMENTS
FOR
THE DEGREE OF DOCTOR OF PHILOSOPHY
IN
CHEMICAL ENGINEERING

JANUARY 2025

Approval of the thesis:

**DEVELOPMENT OF LIQUID CRYSTAL BASED NANOPARTICLE
SENSORS**

submitted by **ASLI KARAUSTA** in partial fulfillment of the requirements for the
degree of **Doctor of Philosophy** in **Chemical Engineering, Middle East Technical
University** by,

Prof. Dr. Naci Emre Altun
Dean, **Graduate School of Natural and Applied Sciences** _____

Prof. Dr. Yusuf Uludağ
Head of the Department, **Chemical Engineering** _____

Assoc. Prof. Dr. Emre Büküşoğlu
Supervisor, **Chemical Engineering, METU** _____

Prof. Dr. Nihal Aydoğan
Co-Supervisor, **Chemical Engineering, Hacettepe University** _____

Examining Committee Members:

Prof. Dr. Nuray Yıldız
Chemical Engineering, Ankara University _____

Assoc. Prof. Dr. Emre Büküşoğlu
Chemical Engineering, METU _____

Assoc. Prof. Dr. Berna Topuz
Chemical Engineering, Ankara University _____

Assoc. Prof. Dr. Simge Çınar Aygün
Metallurgical and Materials Eng., METU _____

Asst. Prof. Dr. Necip Berker Üner
Chemical Engineering, METU _____

Date: 09.01.2025

I hereby declare that all information in this document has been obtained and presented in accordance with academic rules and ethical conduct. I also declare that, as required by these rules and conduct, I have fully cited and referenced all material and results that are not original to this work.

Name Last name : Aslı Karausta

Signature :

ABSTRACT

DEVELOPMENT OF LIQUID CRYSTAL BASED NANOPARTICLE SENSORS

Karausta, Aslı
Doctor of Philosophy, Chemical Engineering
Supervisor: Assoc. Prof. Dr. Emre Büküşoğlu
Co-Supervisor: Prof. Dr. Nihal Aydoğan

January 2025, 118 pages

Liquid crystal (LC) exhibits both the flow properties of liquids and long-range orientational ordering of crystalline solids. Since the ordering of LCs can be controlled by the fine scale of energetics, they have remarkable sensitivity. In this study, we used LC to be able to get response to nanomaterials. Firstly, we aimed to examine the interparticle interactions and self-assemblies of nanoparticles by using the confined systems. We used LC droplet as a confined medium and analyzed the interparticle and LC-nanoparticle interactions at LC-aqueous interface by using gold nanoparticles. Then, we developed a method to determine LC configuration within the microwells with shape of circle, square, triangle, rectangle and star. Lastly, we prepared stable, three-dimensional and water insoluble platform for analyzing LC-aqueous interface by using soft-lithography. The LC configuration within microwells was examined under polarized optical microscope, revealing interfacial tilting and defect formation. Sodium dodecyl sulfate (SDS) molecules were used as a model analyte, demonstrating that change in interfacial tilting due to surfactant adsorption. Depending on the interfacial anchoring, metastable configurations having defect structures which were point defects and disclination lines were formed. Also, the response of LC to the adsorption of silica nanoparticles functionalized with silane and dye molecules were studied and found that concentration of dye molecules

on the nanoparticle surface, in the range of ppb, could be detected via changes in the tilting at the LC-aqueous interface. These findings suggest a potential for sensor applications, a stable platform was developed for detecting various analytes like molecules or colloids.

Keywords: Liquid Crystal, Confinements, Topological Defects, Sensor, Stability.

ÖZ

SIVI KRİSTAL BAZLI NANOPARTİKÜL SENSÖRLERİNİN GELİŞTİRİLMESİ

Karausta, Aslı
Doktora, Kimya Mühendisliği
Tez Yöneticisi: Doç. Dr. Emre Büküşoğlu
Ortak Tez Yöneticisi: Prof. Dr. Nihal Aydoğan

Ocak 2025, 118 sayfa

Sıvı kristaller, hem sıvıların akış özelliklerini ve kristal katıların uzun mesafeli yönsel düzenlerini sergileyen duyarlı malzemelerdir. Sıvı kristallerin oryantasyonu, enerji seviyelerinin kolaylıkla kontrol edilebilmesi sayesinde son derece hassas duyarlılık gösterirler. Bu tez çalışmasında, nanomalzemelere karşı tepki almak amacıyla sıvı kristal kullanılmıştır. Sınırlı sistemler içerisine hapsedilmiş sıvı kristalin konfigürasyonunun tespit edilmesi üzerine yöntem geliştirilerek nanopartiküllerin arasındaki etkileşimlerin ve kendiliğinden oluşturdukları yapıların incelenmesi amaçlanmıştır. Sıvı kristal damlacıkları sınırlama olarak kullanarak, altın nanopartikülleriyle sıvı kristal-su arayüzünde nanopartikül ve sıvı kristal arasındaki etkileşimler analiz edilmiştir. Ardından, daire, kare, üçgen, dikdörtgen ve yıldız şekillerinde mikrokuyularda sıvı kristal konfigürasyonlarını belirlemek için bir yöntem geliştirdik. Son olarak, yumuşak litografi kullanarak sıvı kristal-su arayüzünü analiz etmek için stabil, üç boyutlu ve suya çözünmeyen bir platform hazırlanmıştır. Mikrokuyulardaki sıvı kristal konfigürasyonları polarize optik mikroskop altında incelenerek arayüzdeki eğilme ve defekt oluşumu gözlemlenmiştir. Sodyum dodesil sülfat (SDS) molekülleri, yüzey aktif madde adsorpsiyonuna bağlı olarak arayüzdeki eğilmedeki değişiklikleri gösteren bir model

analizörü olarak kullanılmıştır. Arayüz bağlanmasına bağlı olarak, nokta defektleri ve disklinkasyon hatları gibi defekt yapıları içeren metastabil (kararsız) konfigürasyonlar oluşmuştur. Ayrıca, silan ve boya molekülleri ile işlevsel hale getirilmiş silika nanopartiküllerinin adsorpsiyonuna karşı sıvı kristalin tepkisi incelenmiştir ve nanopartikül yüzeyindeki boya moleküllerinin konsantrasyonunun (ppb seviyesinde) sıvı kristal-su arayüzündeki eğilme değişiklikleri ile tespit edilebileceği bulunmuştur. Bu bulgular, sensör uygulamaları için bir potansiyel sunduğunu ve molekül veya kolloidlerin tespiti için stabil bir platform geliştirildiğini göstermektedir.

Anahtar Kelimeler: Sıvı Kristal, Topolojik Kusurlar, Mikro-sınırlandırma, Stabilite, Sensör

To my family

ACKNOWLEDGMENTS

Firstly, I would like to express my deepest appreciation to my supervisor Asst. Prof. Dr. Emre Büküşoğlu for his endless patience, support, guidance, advices and encouragements during this study. It was an honor for me to work with him as his student and I sincerely appreciate the time and effort he has taken during my graduate education. I would also like to show my gratitude to my co-supervisor Prof. Dr. Nihal Aydoğan for her helpful suggestions.

I must also express my sincere gratitude to Dr. Cevdet Öztin, Prof. Dr. Levent Yılmaz, Assoc. Prof. Dr. P. Zeynep Çulfaz Emecen, Prof. Dr. Nuray Yıldız and Asst. Prof. Dr. Necip Berker Üner for their valuable tutorship.

I would like to thank to Soft and Functional Materials Research Group current and alumni members; Ayşe Nurcan Özşahin Işılak, Gülce İlhan, Cansu Erdil, Cansu Dedeoğlu, İrem Özen, Deniz Karaman, Burak Akdeniz, Özge Batır, Deniz Işınsu Avşar, Selin Şengül, Ramazan Umut Dinç and Ceren Kocaman for their partnership, help and support during my study.

I would like to thank my dear friends Aykut Yavuz, Nur Ber Emerce, Soner Yaşar, Yağmur Çulhacıoğlu, Merve Sarıyer, Bilgehan Yayık, Almira Çaldıklıoğlu, Merve Özkutlu, Seda Sivri, Ezgi Yavuzyılmaz, and Fatma Şahin for their friendship, endless support, encouragements, understanding, helps, suggestions and motivations. I have felt lucky to know each of them all the time.

Last but not the least, I want to express my sincere gratidute to my family; Coşkun, Gönül and Sıla Karausta for loving, supporting and encouraging me all through my life. They have been secret heroes of not only this study but also my whole life.

TABLE OF CONTENTS

APPENDICES

LIST OF FIGURES

xxiii

LIST OF ABBREVIATIONS

ABBREVIATIONS

APTES	Aminopropyltriethoxysilane
AuNP	Gold Nanoparticle
BF	Bright Field
CAC	Critical Assembly Concentration
CLS	Concenteric Loop Structure
CVD	Chemical Vapor Deposition
C10	Decanethiol
C16	Hexadecanthiol
DLS	Dynamic Light Scattering
DMF	N,N-dimethylformamide
DMOAP	Dimethyloctadecyl[3-(trimethoxysilyl)propyl]ammonium chloride
FCPM	Fluorescence Confocal Polarizing Microscopy
FITC	Fluorescein-5-isothiocyanate
LC	Liquid Crystal
MML	Mixed Monolayer
MO	Methyl Orange
MUA	Mercaptoundecanoicacid
NP	Nanoparticle
OTS	Trichloro(octadecyl)silane
PDMS	Poly(dimethylsiloxane)
PE	Polyethylene
PFDTS	Perfluorodecyltrichlorosilane
PI	Polyimide
PL	Polarized Light

POM	Polarized Optical Microscope
PS	Polystyrene
PVA	Polyvinylalcohol
SDS	Sodiumdodecylsulfate
SEM	Scanning Electron Microscopy
TEM	Transmission Electron Microscopy
TEOS	Tetraethoxysilane
TSC	Trisodium citrate
UV	Ultraviolet

CHAPTER 1

INTRODUCTION

In recent years, the advances made in the science and technology have brought an inevitable and rapid rise in the field of nanotechnology. The fundamental component of nanotechnology is the nanoparticles and the number of studies focused on the use of nanoparticles is increasing day by day[1,2].

Nanoparticles (NPs) are particulate matters with at least one dimension that is less than 100 nm. Therefore, the size range of nanoparticles is in between a single molecule and bulk materials, as shown in Figure 1.1, so they have size-dependent properties different from these two sides since they have high surface to volume ratio[3].
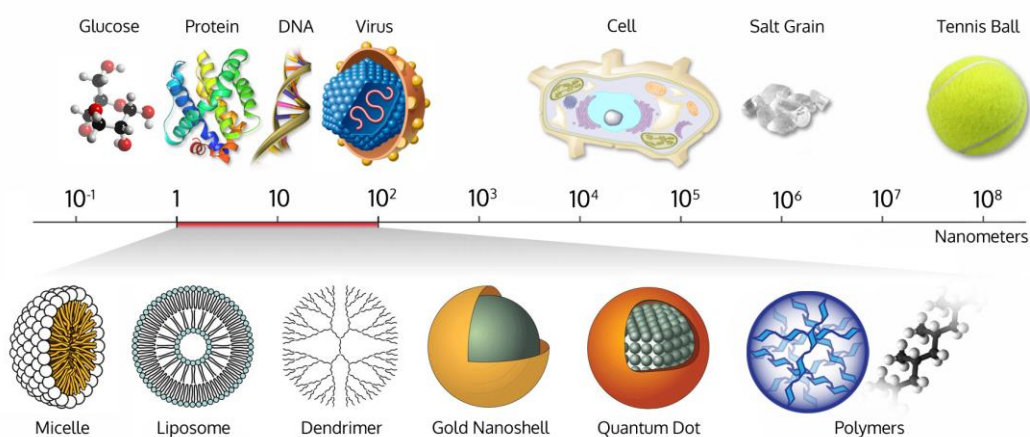
Figure 1.1. Schematic illustration for the size range of the materials and the position of nanoparticles in this scale[4]

The reason of preferability of nanoparticles is directly related with their advantageous electrical, optical, magnetic, mechanical and thermal properties due to the quantum effect arising from their sizes[5]. These properties can be summarized as follows: chemical stability, high saturation magnetization, high magnetic

susceptibility, high electrical and thermal conductivity, catalytic activity and enhanced optical properties etc. In addition to quantum properties, NPs have ability to adsorb and carry other compounds[6]. Because of these properties, nanoparticles have broad application area such that they are used for electronics, sensors, catalysis, medicine, textile, food, construction materials, cosmetics and sunscreens and energy harvesting[7–11].

In order to improve existing applications and create new application areas, the interactions between NPs and also their assemblies should be investigated, firstly. For this purpose, we aimed to analyze the interparticle interactions and also their assemblies. In order to perform these analyses, using of confined systems is reasonable to allow controlling the parameters that affect the interactions between the NPs and providing a pre-designed platform for the self-assembly of NPs. For this purpose, we decided to use liquid crystal (LC) to be able to design the confined systems and get the response against the nanoparticle assemblies and their interactions.

LC is a phase of matter in between a crystalline solid and an isotropic liquid. LC molecules flow but retain some degree of long-range order. They are classified into two groups which are thermotropic and lyotropic LCs. The phase behavior of thermotropic LCs is changed by temperature as represented in Figure 1.2.
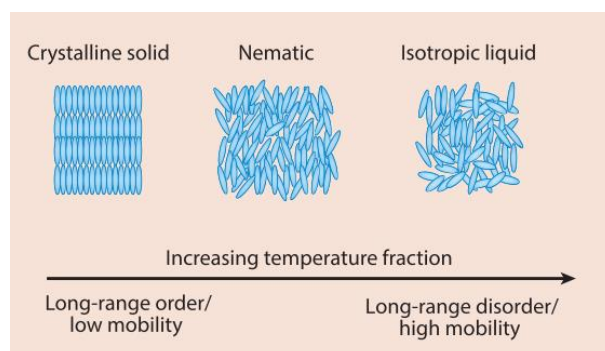
Figure 1.2. Schematic illustration of the phase behavior of thermotropic LCs[12]

As the temperature increases, thermotropic LCs start to lose their long range orientational order but gain high mobility and melt to their isotropic phases. Nematic

2

phases of thermotropic LCs possess orientational ordering towards a uniform direction called director but exhibit no long-range positional order.

The mesogens can quickly rearrange and transmit information across the bulk of the phase because they can diffuse at speeds similar to those of isotropic liquids. In addition, the long-range ordering of mesogens in LCs provides optical birefringence which gives an opportunity for the analysis of ordering just by using polarized optical microscope[12]. Due to these properties, the response of LC is widely used for the analysis of intermolecular and interparticle interactions,

There are three key concepts of LCs that require special attention during the design of pre-defined platform for the analysis of the interactions of the molecules or colloids. These concepts can be summarized as surface anchoring, elasticity and the formation of topological defects.

The surface anchoring results from the intermolecular interactions between the LCs and the surface it contacts with and the orientation of LC molecules depends on the surface anchoring. In the absence of external fields, the orientation of the LC director corresponding to the lowest free energy is defined as the easy axis (Figure 1.3a). When an external field (adsorbent, light, heat etc.) is applied, the director starts to deviate from the easy axis (Figure 1.3a). If the homeotropic anchoring is provided, the LC molecules align in a direction perpendicular to the surface and in the case of planar anchoring, the alignment of LC molecules is parallel to surface. For example, if the interfaces of LC-air and LC-aqueous medium are created, homeotropic and planar anchoring are provided, respectively. In addition to the free interfaces, it is possible to use solid surfaces made from the materials in which LC molecules have specified anchoring or to functionalize the solid surfaces to obtain predetermined LC orientation. For example, the solid surfaces functionalized with DMOAP (Dimethyloctadecyl[3-(trimethoxysilyl)propyl]ammonium chloride), PFDTS (Perfluorodecyltrichlorosilane) or OTS (Trichloro(octadecyl)silane) provide homeotropic anchoring while PVA (Polyvinylalcohol) or PI (Polyimide) provide planar anchoring[13–17].

Another key concept is the elasticity of LCs that provides the long range orientational ordering. When in contact with a surface in a confined environment, LCs may be strained in order to meet the boundary conditions (surface anchoring) set by the confined system. There are three fundamental modes of straining LC ordering which are twist, bend and splay (Figure 1.3b). A comparison of the anchoring energy ($\sim WL^2$, W is the anchoring energy, $\sim 10^{-5}$-10^{-6} J/m^2, L is the size scale of the confined system) and the elastic energy associated with a strain ($\sim KL$, K is the elastic constant of the LCs, $\sim 10^{-11}$ N) reveals a length between 1 and 10 micrometers in which there exists and interplay between elasticity and the surface anchoring. Below this range, elasticity dominates whereas above this range, anchoring energy dominates the ordering of the LCs.

The third key concept is the topological defects (Figure 1.3c). Topological defects form in LCs when internal constraints or external boundary conditions cannot be satisfied by continuous straining of the LC director. With a simple energetical consideration, which takes into account the elastic energy and the energy cost of defect formation, typical value for radius of the defect cores is approximately 5 nm. In fact, it is not possible to visualize objects at the nanometer scale using an optical microscope due to its limited resolution. However, due to the deformation caused around the defects and the birefringent properties of LCs, the defects become visible under polarized optical microscope. On the other hand, it is not always possible to determine the defect type using microscopy. For instance, defects that appear as point defects under an optical microscope could, in fact, be nanometer-sized closed loops[18] These three concepts of LC provide an opportunity to design different systems to obtain the response against the interactions of LCs with molecules or colloids and information about intermolecular or interparticle interactions.

(A) Surface anchoring

n_s (surface director)

n_e (easy axis)

interface

$$F_S = F_0 + \frac{1}{2} W_a(\theta_s - \theta_e)$$

$W_a \sim 10^{-3}$-10^{-2} mJ/m²

(B) Elasticity of liquid crystals

$$F_{el} = \frac{1}{2}K_1(\nabla \cdot \underline{n})^2 + \frac{1}{2}K_2(\underline{n} \cdot \nabla \times \underline{n})^2 + \frac{1}{2}K_3(\underline{n} \times (\nabla \times \underline{n}))^2$$

Splay   Twist   Bend

$K_i \sim 10^{-11}$ N

$L \sim K_i/W_a \sim$ 1-10 μm

(C) Topological defects

$$F_d = \int_{V_d} f_d\, dV_d \sim \frac{4}{3}\pi r_d^3\, \epsilon_d$$

$$r_d \sim \sqrt{\frac{K}{\epsilon_d}} \sim 5 \text{ nm}$$
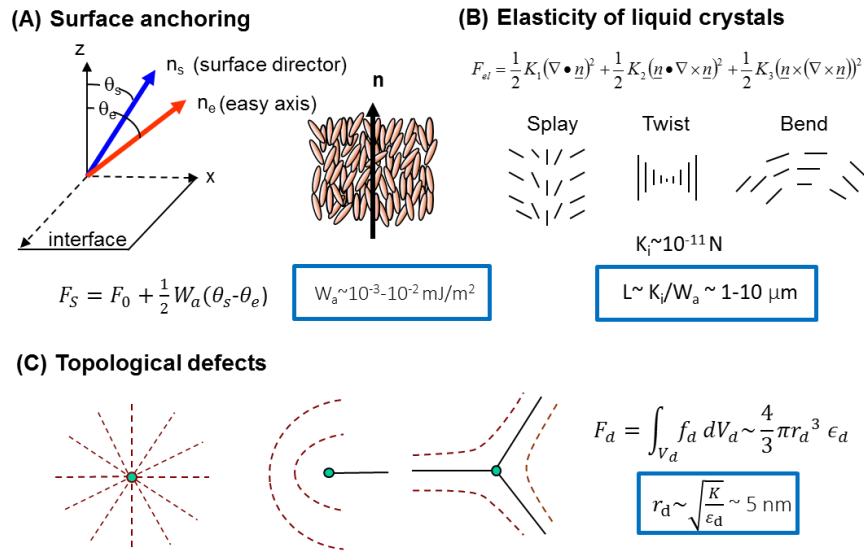
Figure 1.3 Schematic illustrations of (a) the director and easy axis of a liquid crystal (LC) anchored at a surface and expression for F_s, anchoring energy; (b) the three basic modes of deformation of a LC (splay, twist, and bend) and an expression for F_{el}, the elastic free energy density, that results from these strains; and (c) three types of topological defects that can form in a LC: (left) a point defect located at the center of a radially converging director field, and (center, right) cross-sections of line defects (disclinations). The line defects are oriented orthogonal to the plane containing the figure and F_d, represents the energy of formation of a defect.[12]

The appearance of confined LC under polarized optical microscope gives information about the orientation of LC molecules since it has birefringence[19]. The appearance under crossed polarized optical microscope becomes dark when the director is aligned with one of the polarizers. Conversely, when the director of LC is aligned in a direction different than one of the crossed polarizers, the light is refracted, resulting in brightness in the optical appearance under polarized microscope as shown in Figure 1.4. In addition to the orientation in lateral direction, the zenithal (tilt) angle affects the optical appearance under crossed polarized optical microscope. The color of confined LC appeared under polarized optical microscope depends on both the thickness of confined medium and the tilt angle, angle between the LC director and surface normal. Michel Levy Chart is used to determine the

retardance of LC with respect to the thickness of the film. When the retardance of LC is known, it can be correlated to estimate the tilt angle of LC by using Frank-Oseen equation[20]. Therefore, it is possible to determine the tilt angle by correlating with the colors and to obtain information about the configuration of LC.
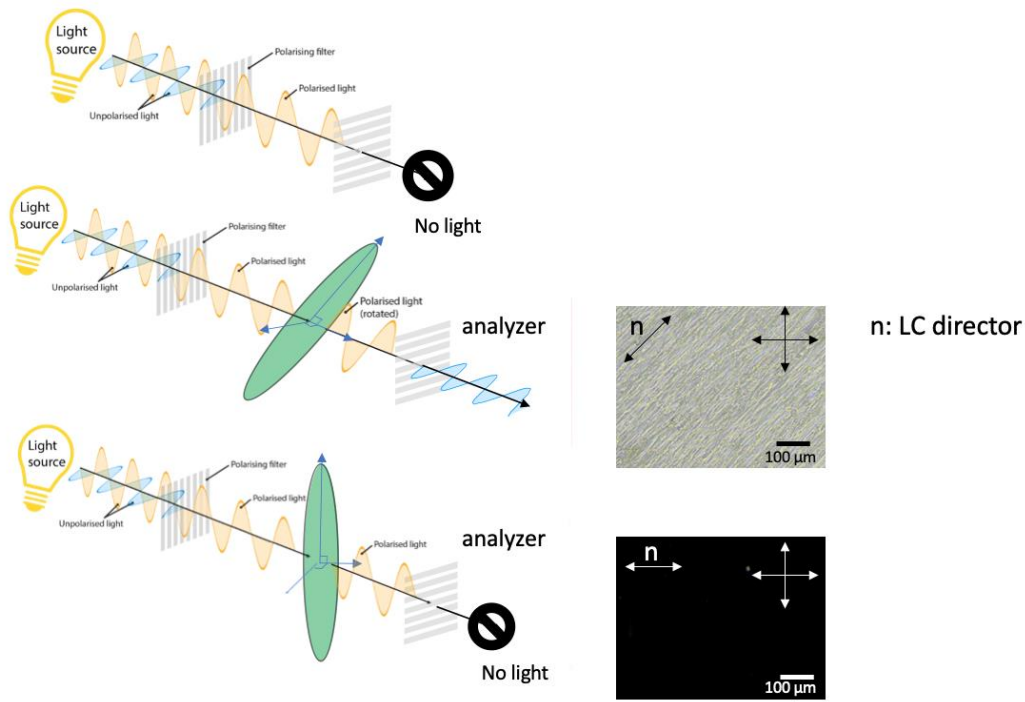
Figure 1.4 Schematics of the principle of optical analyses under polarized optical microscope with cross polarizers. Scale bars: 50 μm

The charge of topological defects occurred in LC can be defined by considering the number of rotation of director around the center[21,22]. The schematics and images of positive and negative charged point defects is shown in Figure 1.5 and Figure 1.6. Since the position of dark brushes appeared under polarized optical microscope depends on the direction of polarizers, the sign of charges can be determined easily by using an experimental method. The positions of dark brushes are followed with respect to the direction of polarizers while the polarizers were rotated. The topological defects can be defined as positively charged if the dark brushes

surrounding them orient in the same direction with the polarizers during the rotation of polarizers; if not, they can be classified as negatively charged topological defects.
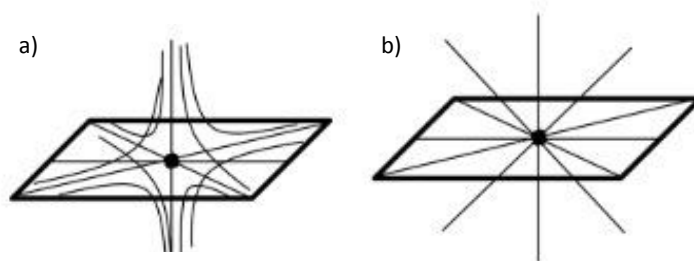
Figure 1.5 Schematics of the director around a) negative, b) positive charged point defects[21]
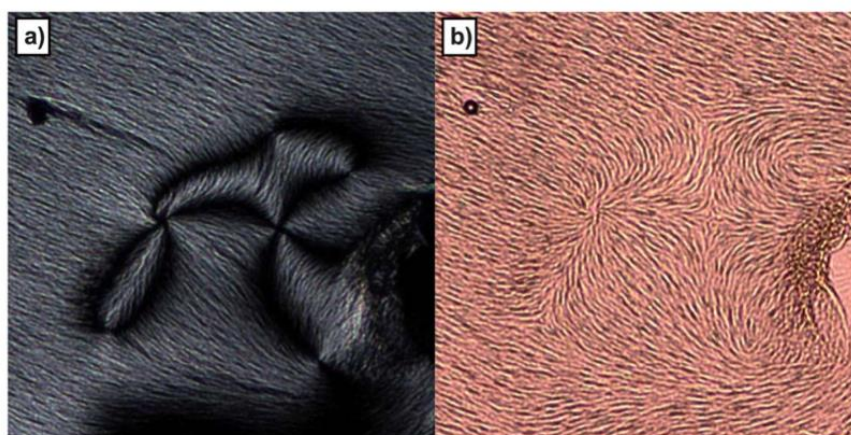
Figure 1.6 The defect director field is visualized through (a) the residual birefringence of LC and (b) reflection microscopy, both of which are non-invasive techniques. The images show the same region of a sample after polymerization of the mixture of 5% RM257 a and E7, illustrating the connection between an s = +1 defect and an s = −1 defect. These defects were formed by rapidly cooling a cell with planar boundary conditions[23].

In order to perform the analysis on the interface of LC-air and LC-aqueous medium, LC can be confined in geometries which are two dimensional such as grids[20,24–27] or three dimensional like microwells and pillars[28–30], droplets[18,31–34]. The determination of LC configuration and defect formation in these geometries is essential to be able to use these confined systems as a platform for the analyses. For example, the

droplets of LC in water can be used as a platform for the analyses of the adsorbates in aqueous medium and their configurations are dependent on the interfacial anchoring and elasticity affected by the size of droplets[35]. While the bipolar configuration has two positively charged (+1/2) point defects on the two poles of droplets, in the radial configuration a positively charged (+1) point defect is located at the center of the droplet as shown in Figure 1.7. When the interfacial anchoring is changed from planar to homeotropic, the configuration of LC droplet changes from bipolar to radial configuration. During the transition, additional equilibrium states are observed. Initially, the two defects characteristic of the bipolar configuration disappear, leading to the formation of an axial configuration, distinguished by the appearance of a line disclination on the droplet surface. Subsequently, as the anchoring strength increases, the surface line disclination transforms into a point defect positioned near the LC-water interface. This intermediate state, referred to as the pre-radial configuration, is characterized by the angle-dependent bright appearance of droplets under a polarized microscope. Finally, before the LC droplets achieve the radial configuration, the point defect shifts to a location between the center and the surface of the droplet, forming the escaped radial configuration. These transitions provide an opportunity for getting a response to exposure of adsorbates at LC-water interface since these configurations can be easily distinguished under a polarized optical microscope as shown in Figure 1.7. Therefore, it is possible to use confined LC as a platform for the sensor applications.
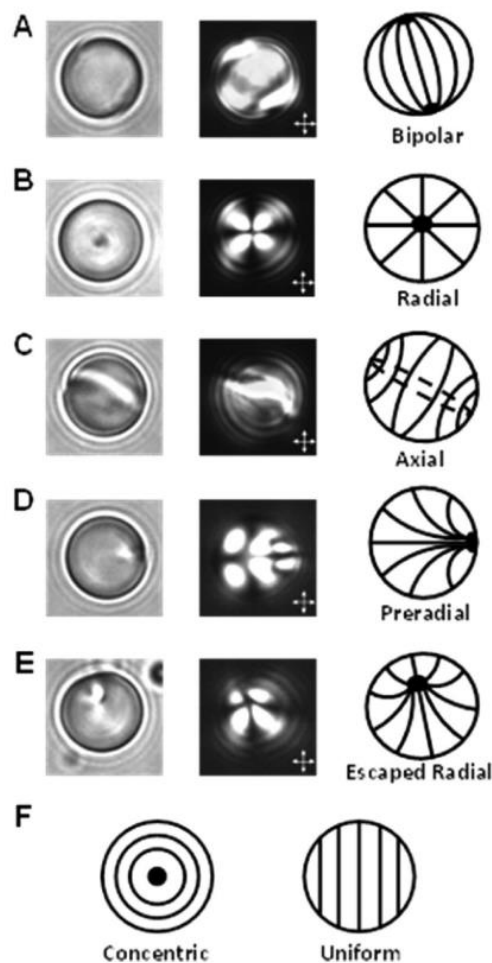
Figure 1.7 The brightfield, polarized light and schematics of the configurations of LC droplets. White arrows show the direction of analyzer and polarizer.[36]

When considering all these configuration changes and defect formations in LCs, their potential applications are highly diverse. In fact, when the key concepts of LCs are considered as design parameters and LCs are confined in specified geometries, it is possible to control the LC configuration in these confined systems. Therefore, it is possible to use LC as a tool to prepare a predesigned platform for the self-assemblies[37–41] or sensor applications[27,42–44]. By using this pre-designed platform, the assemblies of the molecules and colloids can be controlled or response based on the concentration of an adsorbate can be obtained. Our primary objective was to develop a methodology for observing the behavior of nanomaterials adsorbed at the LC-aqueous interface. Nanoparticles were chosen as model systems due to their

ability to be functionalized, as well as their size, which closely resembles that of viruses. Therefore, it is possible to mimic viruses by using functionalized nanoparticles having various surface properties without working with viruses' complex structures. To achieve this, we confined LC within two distinct geometries which were droplets and microwells, employing them as platforms for analysis. A novel approach was developed to investigate the LC configuration within these confined systems, specifically at the LC-air and LC-aqueous interfaces. Optical techniques were employed to characterize the LC alignment and assess the formation of topological defects. Functionalized nanoparticles, surfactants, and dye molecules were used as adsorbates to probe the LC response, providing insights into the potential of this system for nanomaterial sensing applications

CHAPTER 2

LITERATURE REVIEW

LC is a favored responsive phase of material that exhibits both the flow properties of liquids and long-range orientational ordering of crystalline solids. Since the ordering of LCs can be controlled by the fine scale of energetics, they have remarkable sensitivity[12]. This sensitivity of LCs provides opportunities for the sensor and actuation applications when combined with the advance in the preparation of surfaces possessing well-defined structures and properties[12,20,45–48]. The response of LC is indicated by changing the molecular orientation and this change in orientation is easily visible using a simple polarized microscope resulting from their birefringence making LCs advantageous. The effects that create changes in the orientation can be due to stimuli such as heat[49], light[50–53], chemical reactions[44,49,54,55], adsorption[13,27,38,56–58] and applied force[59].

The studies investigating the orientation of LC and defect structures created by confining LC in geometries such as grids, cells or droplets[60,61] have utilized different phases of LCs, including nematic[31,32,47,56,62,63], cholesteric[53,61,64–66], and blue phases[67,68]. These phases of LCs have distinct types of topological defects and usage areas based on their unique molecular arrangements and properties. In the nematic phase, point defects, disclination lines, and loops typically form due to boundary conditions and external fields.

Having control on the LC orientation and formation of defects at specified positions provide an opportunity to regulate the self-assembled structures of molecules[24,48,54,56] and colloids[37,38,69]. In addition to the self-assembled structures, changes in the LC orientation created by the adsorption of amphiphilic molecules[56,70–73] (such as surfactants and lipids), proteins[74], gas molecules[75,76] or nanoparticles[37–39] at the interfaces of LCs have been reported by confining LC in a geometry. To date, studies have been conducted generally by using two-dimensional geometries like TEM

grids[20,24–27] or sandwich cells[17] and 3D geometries like microwells and pillars [28,29,63], microfluidics[60,73] or droplets[31,33,34,65,77]. In these studies, the effects of geometry and interfacial phenomena on the configuration of LCs within confined systems, specifically through changes in elasticity and anchoring, were investigated, and several sensor applications were proposed.

In the study of Gupta et. al, LC was confined in the geometry of droplet[78]. In this study, to analyze the configuration of LC and topological defects occurred in the confined medium, the surface anchoring, which is one of the key concepts of LC, was tuned by the adsorption of a surfactant molecule, sodium dodecyl sulfate (SDS). This surfactant molecule changed the interfacial anchoring of LC so, surface-driven ordering transition was observed in LC droplets. In this study, to eliminate the effect of droplet size and also the temperature, the monodispersed LC droplets were synthesized at constant temperature and their configuration was analyzed by using polarized optical microscope (POM) as shown in Figure 2.1. It was shown that as the interfacial anchoring was changed, the location of the topological defects was also changed and the configuration of LC droplets changed depending on the concentration of surfactant molecule. Therefore, it was shown that the orientation of LC and topological defects can be controlled by tuning the medium of the LC confinement which was droplet in this study.
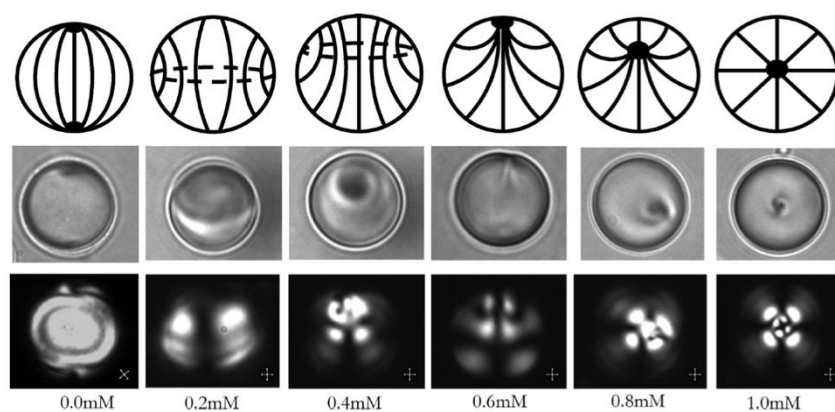
Figure 2.1 Schematics of the LC droplets (top row), BF and PL micrographs of the 5CB droplets with respect to the SDS concentration (the middle and bottom rows, respectively)[78]

Then, Wang et. al enhanced the method to specify surface anchoring on LC droplets that created a patterned LC orientation providing different configuration of LC droplets[79]. They confined LC in droplet geometry and adsorbed them at aqueous-glycerol interfaces. They used aqueous solution of SDS and glycerol to provide perpendicular and parallel alignment, respectively. When the LC droplets were adsorbed at the interfaces of SDS aqueous solution and glycerol, patterned surface anchoring was procured as designed by tuning the experimental parameters like concentration, time etc. (Figure 2.2).
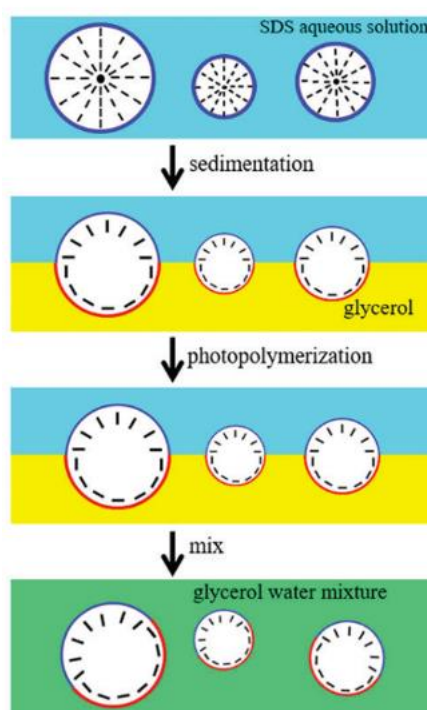
Figure 2.2 Schematic illustration of preparation method of LC droplets having patterned configuration by controlling the interfacial anchoring provided with aqueous SDS solution and glycerol interfaces[79].

The patterning of LC orientation can be also achieved by preparation of structured geometries and functionalization of these platforms. For example, micropillars have been used as a structured geometry to confine LC and to control the orientation of LC. Kim et. al used the silicon substrate with specific patterns to prepare sandwich cells as a confinement[63]. This substrate was fabricated in such a way that there was

a pattern of holes with different lattices. In these geometries, the functionalization of the walls, the sample thickness, shape of the patterns and the distance between the holes (air pillars) were varied. By filling these cells with LC, the formation of defects and their charges were investigated. It was found that the sum of the winding number of all of the defects formed on the entire sample cancelled out. In addition, they investigated the effect of isotropic to nematic to smectic transition and the cooling rate on the LC orientation. They found that in the case of rapid cooling, the more ordered defect lattice is formed.
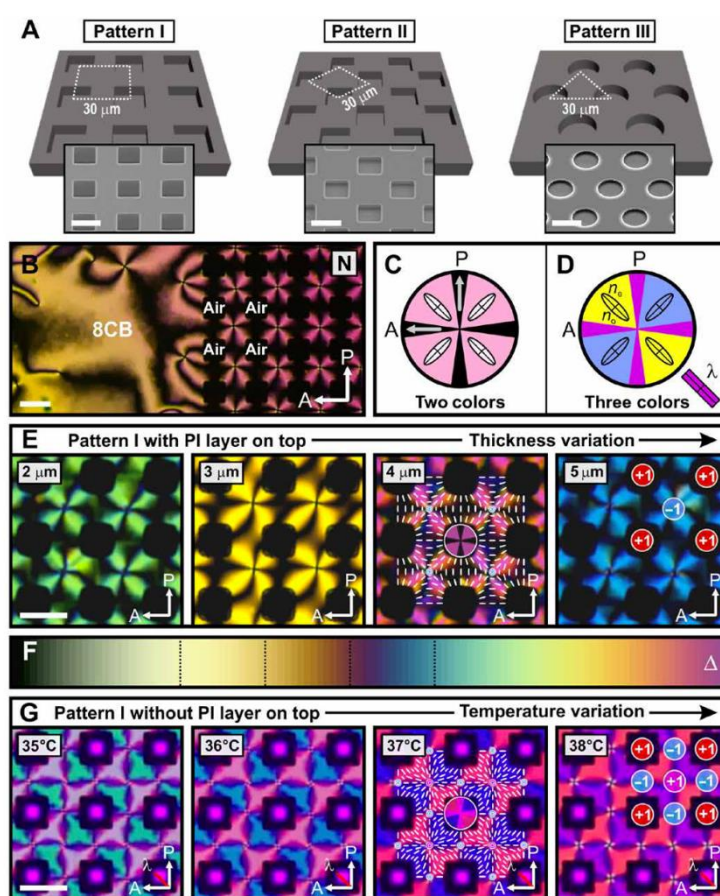
Figure 2.3 A) Schematics of the structured silicon substrate with three different patterns B) Appearance of LC under polarized optical microscope in the case of absence and existence of pattern of pillars, C,D) Schematics of direction of dark brushes and polarizer and analyzer, E) Color variation depending on the thickness of

sample, F) Michel-Lévy Chart, G) Color variation with respect to the temperature of the samples. Scale bars: 20μm[63]

Another method that has been used in the literature for the analysis of LC orientation was using the capillary tubes as a confined system. For example, Zhong et. al. used functionalized capillary tubes to design an imaging system for the analysis of the behavior of amphiphiles and ions at aqueous-LC interfaces such that after the adsorption of surfactant molecules the optical appearance of LC confined in capillary tube changed from two bright lines to four petal texture (Figure 2.4)[42].
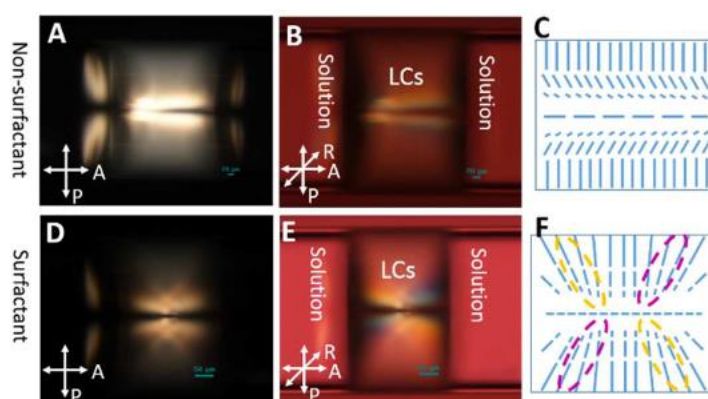
Figure 2.4 (A), (B), and (C) are the optical images and top view schematic of the microcapillary-confined LCs contacting the non-surfactant solutions; (D), (E), and (F) show the optical response and top view schematic of the microcapillary-confined LCs contacting the surfactant solutions. The purple and orange dashed circles in (F) indicate how the four-petal shape is formed.[42]

In addition to experimental[18,21,63,80–84] studies, there have been theoretical[21,22,82,84] studies on different geometries like thin films, capillary tubes, etc. to simulate the LC orientation and defect formation. Yao et. al carried out a theoretical study with the help of Onsager model[28]. With this model, they addressed the 2-D nematic defect structures of rodlike molecules, which they made an analogy with lyotropic LCs, confined in different geometries in various sizes and aspect ratios. The model focused on the minimization of the total free energy by changing the alignment of LC and thus the location and charge of topological defect. By carrying out an

algorithm for numerical solution they found several different defect patterns as shown in Figure 2.5. The outputs of this study provided insights into control over the alignment of LCs, locations and charges of the topological defects. Although there was no distinct conclusion on the parameters that define the configuration, it provided an idea about ability of locating the defects on different positions by using confined geometries with different aspect ratios or with same shape but different ordering parameters.
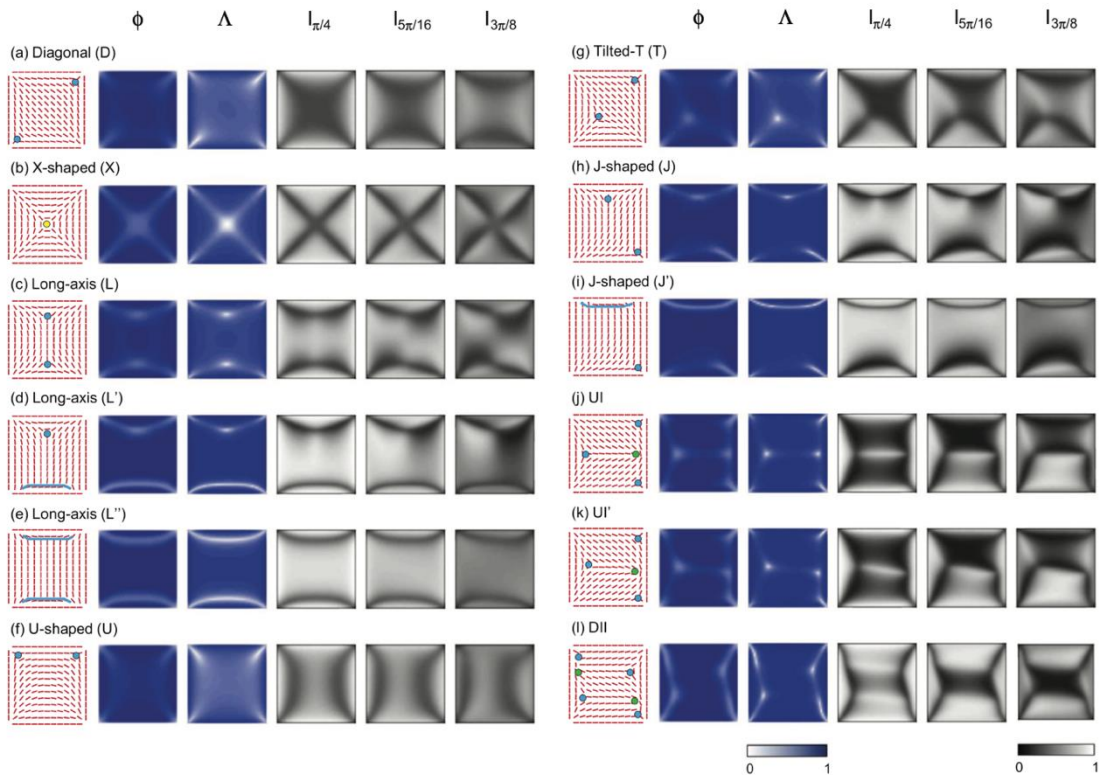
Figure 2.5 Nematic defect structures found from the solutions to the extended Onsager model in the case of aspect ratio:1.[28]

In addition to the studies on determination of LC configuration within the specified geometries, the self-assemblies of the molecules and colloids on the defects occurred in the LC were investigated. In these studies, it was shown that the topological defects in LC can be used as template for the assemblies of molecules and also the colloids so it can be possible to design pre-defined patterns for them. For example, "Saturn ring" disclination line, which is a type of line defects occurred around the

particles, was used as a template for the assemblies of the molecules. In the study of Wang et. al., Saturn ring disclination line was formed around silica microparticles. In order to form Saturn-ring defects, they functionalized the surface of silica particles such that the alignment of the LC is perpendicular to the surface of microparticles and they confined the LC in two glass slides with parallel anchoring, so a line defect occurred around the particles. Then, amphiphiles with different tail lengths were mixed with LC to analyze the adsorption. For this purpose, the critical assembly concentration (CAC) of amphiphiles were found and the assemblies of them were analyzed by conjugating to fluorescent dye, BODIPY. It was shown that the self-assembly of the amphiphiles was triggered by the environment of the LC defects (Figure 2.6)[85]. The self-assembly of amphiphiles was formed on the defect region selectively, while remaining individually dispersed in the bulk LC.
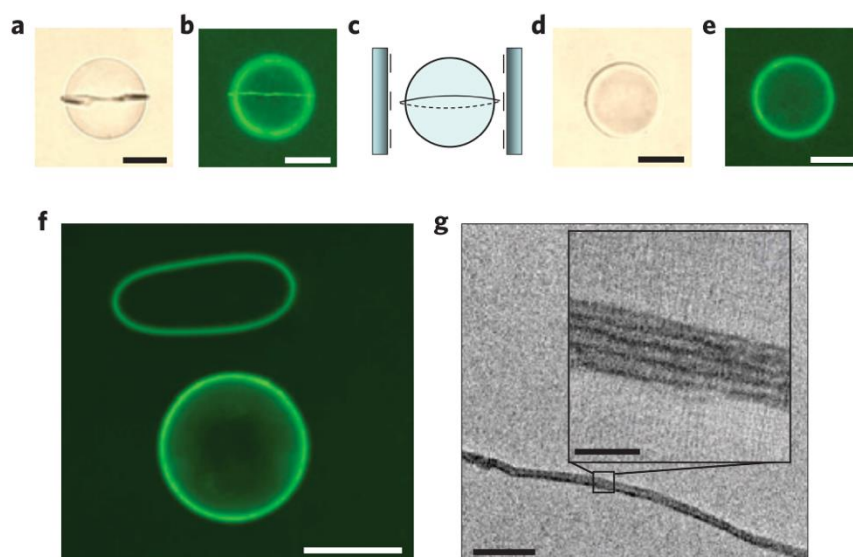
Figure 2.6 Reversible formation and in situ crosslinking of molecular assemblies of amphiphiles templated by a −1/2 'Saturn-ring' disclination line formed about microparticles. (a) Bright-field and (b) fluorescence micrographs representing the fluorescent dye doped photoreactive lipid that adsorbed on the disclination line formed in nematic 5CB, (c) Schematic illustration of a −1/2 'Saturn-ring' defect around particles dispersed in nematic LC with 0° twist. (d) Bright-field and (e) fluorescence micrographs of the fluorescent dye doped photoreactive lipid that

adsorbed on the disclination line formed in isotropic 5CB, (f) Fluorescence micrograph of a polymeric "O-ring" with a diameter of 20 nm that slipped from the equatorial plane of the microparticle. Scale bars: 50 μm. (g) TEM image of the polymeric structure obtained in f. Scale bars: 100nm (main image); 20nm (inset).[85]

In addition to disclination lines, other topological defects have been used as a template for patterning of colloids. For example, Musevic and his colleagues used a sandwich cell as a confined system with treated surface to induce parallel orientation of LC. In this system, the colloids whose surfaces were treated chemically to induce perpendicular surface orientation of LC were dispersed, so elastic distortion of LC occurred around the colloids and topological defects positioned in the vicinity of them. The colloidal particles formed two-dimensional crystal structures that were bound by topological defects, so the assemblies of the colloids can be adjusted and the patterns they formed can be designed depending on LC anchoring on the particles (Figure 2.7)[86]. In this system, the alignment of LC at the bottom and top was adjusted by functionalization of the walls (glass slide in this study) where the LC is in contact but controlling the alignment in third dimension is not possible in this geometry. Moreover, it cannot allow to get response of LC at different interfaces like LC-aqueous phase or LC-air.
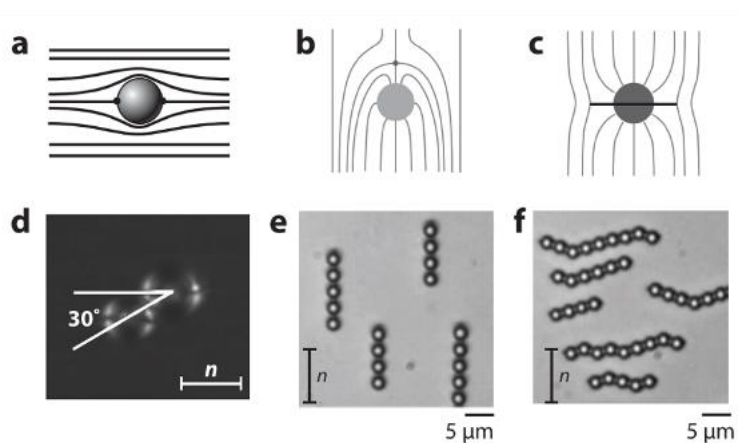
Figure 2.7 Liquid crystal-mediated colloidal self-assembly. (a-c) Schematic illustration of LC director profiles dispersed in nematic LCs with either (a) tangential surface anchoring on the particles or (b,c) homeotropic anchoring on the particles.

(d-f) Micrographs showing the assemblies of microparticles in the case of LC director profiles shown in a-c.[86]

Koenig et. al. used TEM grid to create a confined medium and they analyzed the assemblies of the colloids by controlling the orientation of LC at the interface with aqueous phase. In order to control the order of LC, they added surfactant molecules to aqueous phase and also used underlying substrate. Thus, microparticle assemblies could be patterned at the liquid-liquid interface (Figure 2.8)[87].
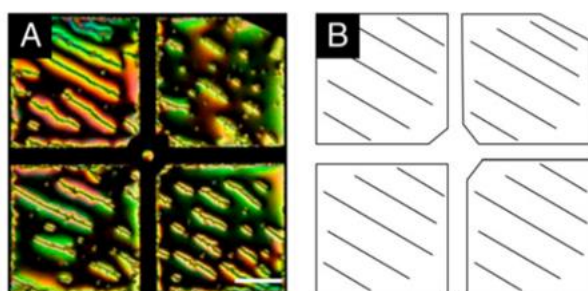
Figure 2.8 (A) Polarized optical micrograph of microparticle chains at the nematic 5CB–aqueous interface (B) Schematic representation of the azimuthal alignment of the LC. (Scale bar: 100 μm)[87]

Recently, Mukherjee et. al. showed a surface-sensitive method to classify the presence of polymeric microparticles with distinct surface properties (Figure 2.9) [88]. In this study, they analyzed the patterns of microparticles which are PS and PE and by using TEM grids in aqueous medium as a confined system and it is possible to distinguish them with the help of difference in the surface properties of these microparticles.

In the systems including the interface with air or aqueous system, there is an opportunity to design platforms with hybrid surface anchoring but thin films have a limitation on the third dimension because of their geometry. Another disadvantage of using these systems is that during the preparation of the LC thin films on the TEM grids, excess amount of LC is discarded that means wasting the LC more than necessary for the analysis. Moreover, TEM grids are so susceptible to oxidation and can be easily deformed so they are limited in terms of reusability[89].
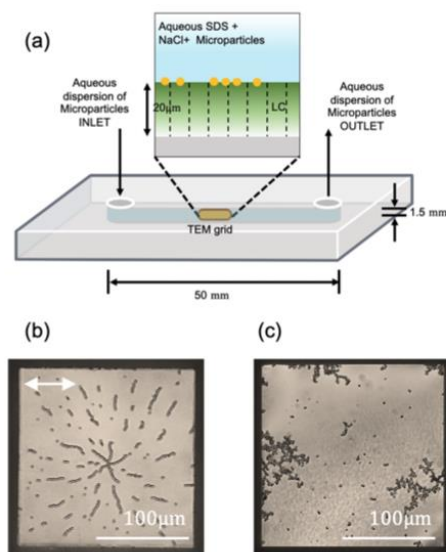
Figure 2.9 a) Schematic illustration of a millifluidic channel used to obtain the images of microparticles adsorbed to LC-aqueous interfaces. (b and c) Top view of the LC-aqueous interface decorated by PS or PE microparticles (b and c, respectively), as seen under an optical microscope (single polarizer). The aqueous phase from which the microparticles were adsorbed contained 0.3M NaCl and 0.025 mM SDS. The microparticles were adsorbed for 1 h. Scale bar is 100μm. [88]

In a recent study, Sengul et. al. used 5CB droplets as the confined medium to investigate the response of LC droplets to adsorption of silica nanoparticles which were functionalized to provide surface properties which are hydrophilicity, hydrophobicity, surface anchoring of LC, surface charge depending on pH[38]. In this study, DMOAP coated, carboxylic acid terminated and mixed monolayer coated silica nanoparticles were prepared and the response of LC droplet in the case of adsorption of these nanoparticles were investigated by using polarized optical microscope and surface characterization by using SEM. It was found that the distribution of LC configuration depended on the functionalization method and the concentration of nanoparticles and the pH of aqueous medium. When the surface charge of nanoparticles and the charge of LC droplet were opposite, the

20

concentration of nanoparticles could be high enough for the surface coverage and affect the LC configuration as shown in Figure 2.10 .
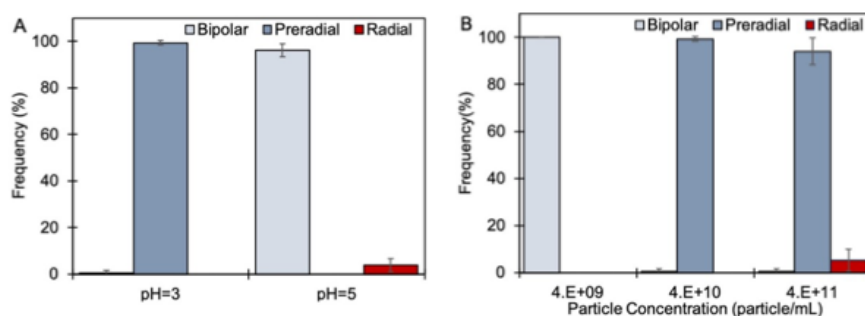
Figure 2.10 The distribution of 5CB droplet configuration dispersed in suspensions of silica particles coated with mixed monolayers of –COOH-terminated silanes and DMOAP. (A) pH of the suspension, (B) particle concentration at pH=3.[38]

In addition to nematic LC, Akman et. al. used cholesteric LC to create well-defined fingerprint assemblies of the silica nanoparticles at LC-aqueous interfaces[37]. In this study, the interplay between the elastic and electrical double layer interactions was investigated and the strategies for the adjustment of interparticle interactions were defined. It was found that the most dominant interactions were the electrical double layer forces and elastic interactions. By adjusting these interactions, fingerprint assemblies determined by the sub-interface defects of the cholesteric LC droplets were formed. The patterns of nanoparticle assemblies were tuned by controlling the surface anchoring on nanoparticles, pH and ion concentration of the medium. In order to visualize the assemblies of the nanoparticles on the droplet surfaces, the droplets were polymerized and imaged by using SEM (Figure 2.11).
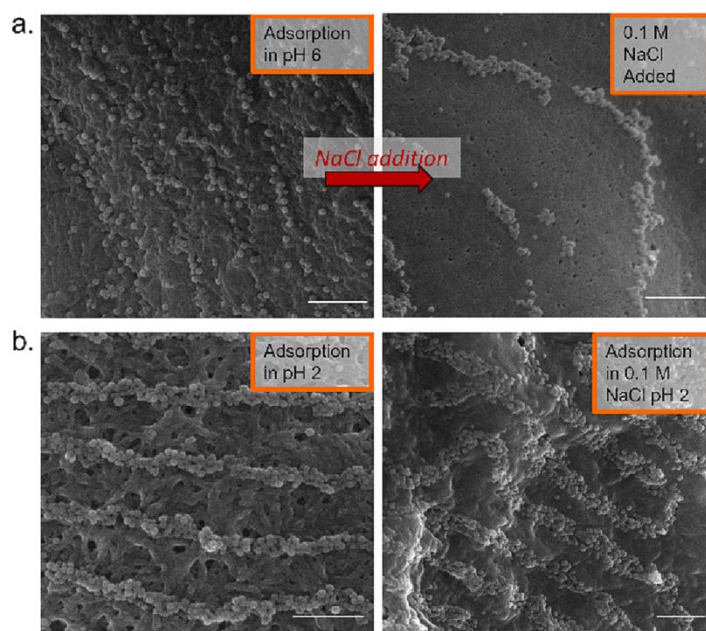
Figure 2.11 SEM micrographs of polymerized droplets with the configuration of Concenteric Loop Structure (CLS) droplet in the case of 0.1 M NaCl addition in the case of a) pH=6, b) pH=2. Scale bars: 1.5 μm[37]

In addition to the assemblies of nanoparticles, the sensor applications have been investigated by using LC droplet as a confined medium. Recently, Sezer et. al. studied the sensor application of nanoparticle assisted LC droplet for detection of molecular species[58]. For this purpose, dye molecules were selected as model analyte and adsorbed on functionalized silica nanoparticles and then the response of LC droplet upon the adsorption of these nanoparticles was investigated under polarized optical microscope. It was found that LC droplets respond to 0.01 ppb of analyte concentration which means of high sensitivity for sensor applications. Furthermore, this application method paves the way of sensing the water-soluble analytes which cannot result a direct ordering transition at the interface of LC-aqueous medium (Figure 2.12).
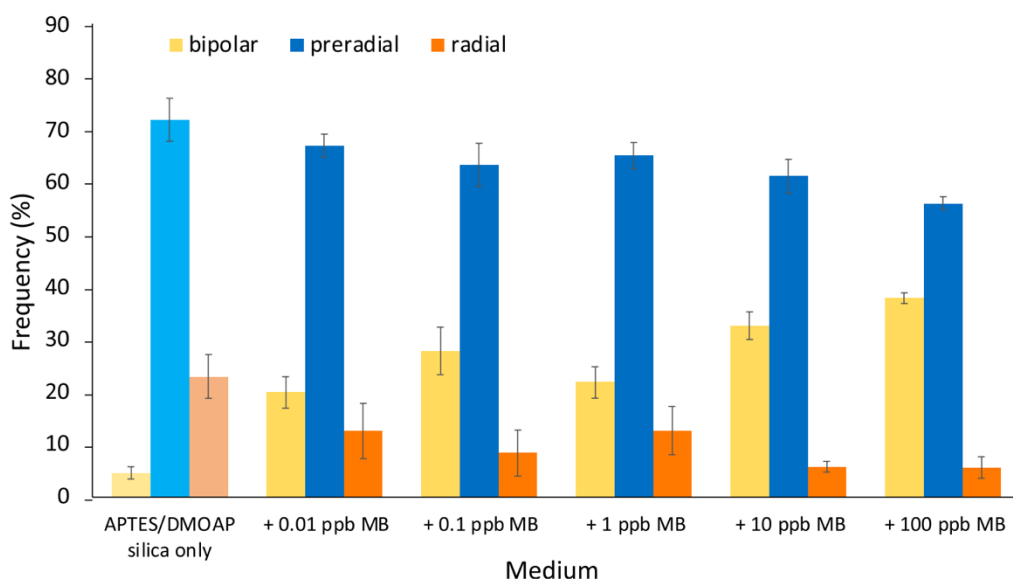
Figure 2.12 The frequency of 5CB droplet configurations in the case of adsorption methylene blue incubated APTES/DMOAP silica nanoparticles with respect to the dye concentration.[58]

Among the interfaces, the aqueous-LC interface has several unique characteristics that differentiate it from other interfaces[45,46,90]. The following characteristics can be summarized: the aqueous-LC interface is soft and easily deformed; adsorbates can migrate to the aqueous-LC interfaces via the aqueous phase; and molecular species at the aqueous-LC interface exhibit significantly higher mobility compared to those adsorbed on solid surfaces. This enhanced interfacial mobility allows for quick reorganization of molecules in response to elastic stresses within the LC films. Therefore, using the LCs to create a free interface with aqueous medium makes it possible to create the systems for analyses by considering these characteristics[56,59,65]. However, establishing a stable system underwater poses a significant challenge. Problems such as droplet formation, absorption, and de-wetting in underwater systems have rendered long-term applications unfeasible[91–93]. Bubble formation disrupts with optical characterization, while issues related to absorption and de-wetting hinder the attainment of reliable results and reproducibility. For instance, TEM grids are commonly employed as a confinement method to fabricate fast and

reliable sensors, as well as platforms for analyzing LC orientation. However, they are not suitable for in-situ operations in an aqueous medium, as achieving a uniform filling of the grids and fixing the LC anchoring without any stimuli is challenging. Additionally, they are not useful for such applications due to their inability to remain stable for long periods in aqueous environments[91].

In the light of outputs of these studies, the importance of developing useful, reusable systems that can provide a large amount of data at once, to examine the effects of different adsorbents and to provide a control over the self-assemblies that are formed has been understood, very well. The ultimate goal of this study was to develop a method for sensor applications to collect the response against the nanomaterials. For this purpose, we enhanced a method for the determination of configuration of LC confined in specifically designed systems which were stable, controlled, three dimensional geometries. In this study, we used surfactant molecules (SDS) and functionalized nanoparticles (silica and gold nanoparticles) as a model and analyzed the change in the LC configuration in the case of their adsorption on LC-water interface and also the assemblies of nanoparticles.

CHAPTER 3

EXPERIMENTAL METHODS

3.1   Materials

4-Cyano-4′-pentylbiphenyl (5CB) and 4-(3-acryloyoxy-propyloxy) benzoic acid 2-methyl-1,4-phenylene ester (RM257) were purchased from HCCH Jiangsu Hecheng Chemical Materials Co., Ltd. (China). Photoinitiator (1-hydroxycy-clohexyl phenyl ketone), anhydrous acetone, toluene, gold(III) chloride trihydrate ($HAuCl_4$), trisodium citrate (TSC), 1-decanethiol (C10), 1-hexadecanethiol (C16), 11-mercaptoundecanoicacid,   aminopropyltriethoxysilane   (APTES,   99%), tetraethoxysilane (TEOS), ammonium hydroxide (25-30%), succinic anhydride, N,N-dimethylformamide   (DMF),   Trichloro(octyl)silane   (OTS), Dimethyloctadecyl[3-(trimethoxysilyl)-propyl]ammonium   chloride   (DMOAP), Poly(dimethylsiloxane) (PDMS) were purchased from Sigma-Aldrich (St. Louis, USA). Anhydrous ethanol was purchased from Isolab (Eschau, Germany). Methyl orange (MO) was purchased from Merck (Damstadt, Germany). Epoxy was purchased from Epotek-Epoxy Technology (Augsburg, Germany). Purification of water (18.2 MΩ cm resistivity at 25 °C) was performed using Heal Force Smart Mini water purification system (Shanghai, China).

3.2   Methods

3.2.1   Synthesis of Citrate Capped Gold Nanoparticles

5.0 mg $HAuCl_4$ was dissolved in 50 ml distilled water and heated up to 100°C (until the bubbles start to form). Then, the citrate solution (10.7 mg TSC in 0.94 ml distilled water) was added and color change was observed. The color started to change from

colorless form to wine red in the order of yellow, black, purple and red. (Figure 3.1) When the color of the solution turned to wine red, the lid of the flask was opened and stayed to cool to room temperature. The solution was stored in refrigerator.
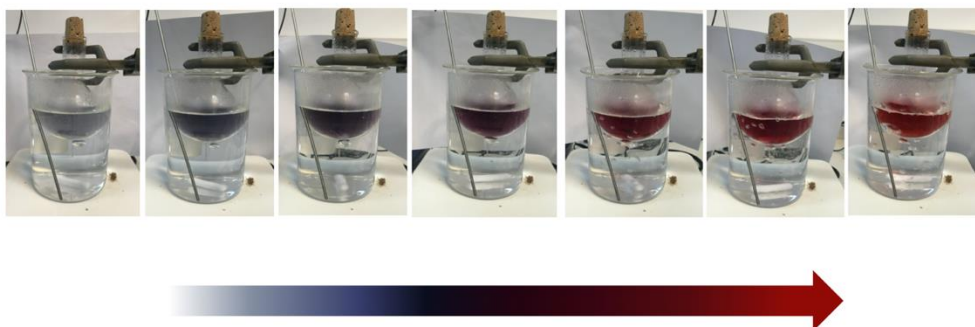
Figure 3.1 Color change during the synthesis of citrate capped gold nanoparticle with time

3.2.2 Functionalization of Gold Nanoparticles

For surface functionalization, decanethiol (C10), hexadecanethiol (C16) and mercaptoundecanoicacid (COOH) was used. For monolayer coating, 4 mM of alkanethiols or carboxylic acid was prepared in ethanolic solution. When the surface nanoparticles were coated with mixed monolayer by using abovementioned chemicals, the composition of them was adjusted as 4:1, 1:1 or 1:4. After the chemicals were dissolved in ethanol, nanoparticles were added to the solution with the amount of 20% of the volume of ethanolic solution and stayed for overnight. Then, the suspension of gold nanoparticles (AuNPs) was centrifuged and supernatant was changed three times with ethanol and pure water, respectively to eliminate the excess amount of the chemicals which were not adsorbed on the surface of the nanoparticles (Figure 3.2).
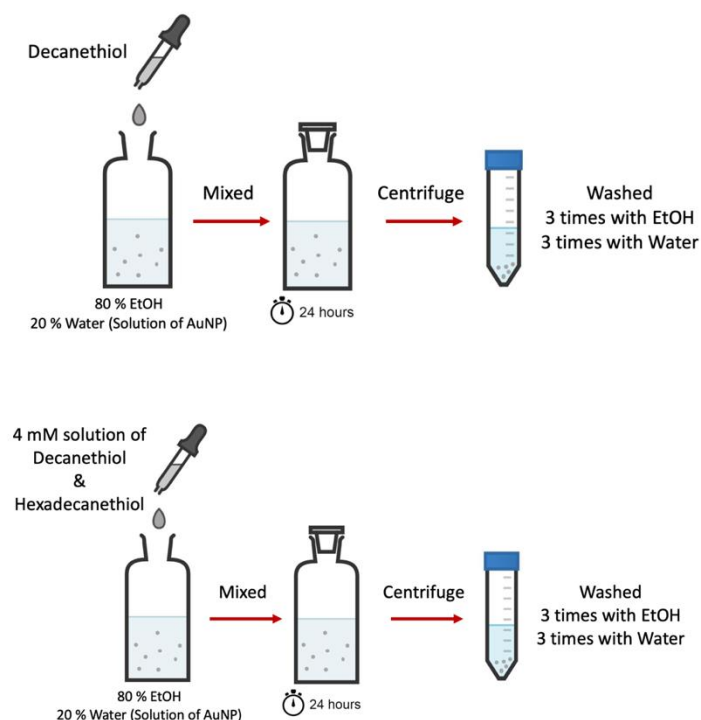
Figure 3.2 Schematic of the procedure for the functionalization of the gold nanoparticle by coating the surface with alkanethiol monolayer (top: decanethiol monolayer, bottom: mixed monolayer)

3.2.3   Preparation of LC-in-Water Emulsions

3 μl of 5CB was added to a vial containing 1 ml of aqueous AuNP dispersion. Then, by using vortex mixer for 30 seconds at 1500 rpm, LC droplets were formed in the size of 1-10 μm.

3.2.4   Polymerization of LC Droplets

20 wt% of RM257, 80 wt% of 5CB, and photoinitiator 1-hydroxylcyclohexyl phenyl ketone at 5 wt/wt % based on the mass of RM257 were mixed and homogenized in toluene by using a vortex mixer. After ensuring a homogenous mixture, toluene was evaporated under vacuum. 3 μl of the mesogen mixture was added to 1 mL of

27

aqueous suspension of gold nanoparticles and mixed by using a vortex mixer for 60 seconds. Then, LC droplets were polymerized under a 365 nm UV light source for 10 minutes. After polymerization, the particles were rinsed firstly with water to prevent additional adsorption and eliminate free nanoparticles. Then, in order to extract the unreacted mesogen, the particles were rinsed at least three times with ethanol.

3.2.5   Preparation of PDMS Micropillars

For the preparation of PDMS solution, the prepolymer was mixed with elastomer curing agent in 10:1 weight ratio. Then, the solution was poured on an OTS coated silicon wafer masks which have micron sized protrusions on the surfaces and then waited overnight at 80°C for curing, at the end, PDMS microwells were obtained. The surfaces of PDMS microwells were coated with trichloro(octyl)silane (OTS) with chemical vapor deposition method (CVD). For the replica of microwells, PDMS solution was poured on OTS coated PDMS microwells which have protrusions and after the curing of PDMS, molds with micropillars were obtained.

3.2.6   Preparation of Water Insoluble Microwells

An electronic grade commercial epoxy was dropped on a glass slide and the PDMS mold was placed on epoxy drop in such a way that preventing the bubble formation. Then, it was maintained at room temperature for 2 days for the curing. At the end, PDMS molds were peeled from the surface of the epoxy, so epoxy microwells attached on the glass pieces were obtained. The procedure was applied for square, rectangular, circular shaped microwells with the sizes in the range of 10-100 μm.

3.2.7 Coating the Surface of Microwells with DMOAP

After the curing of epoxy on the glass slides, they were peeled off from the PDMS molds and immersed in the aqueous solution of DMOAP with the concentration of 2% by volume for 1 hour. Then, rinsed with ethanol and water and dried by using nitrogen stream.

3.2.8 Measurement of Contact Angle

The contact angle of 5CB and water on bare and DMOAP coated epoxy films was measured by using DataPhysics OCA 200 (DataPhysics Instruments, Filderstadt, Germany) with Sessile drop method. 2 µl of 5CB and 2µl of pure water was dropped on the surface of bare epoxy and DMOAP coated epoxy by using a needle and the angle was measured with a camera and an image processing method.

3.2.9 Filling Microwells with Liquid Crystal

After preparation of microwells, in order to provide wetting of LC on the surface of the epoxy microwells, the surface was coated with DMOAP. Then, microwells were filled with 5CB by using a spin coater at 1000 rpm for 5 minutes.

3.2.10 Polymerization of LC Confined in Microwells

Microwells were filled with the mixture of 20% wt of RM257 and 5CB by using a spin coater. Then, it was photopolymerized using a 365 nm UV light source for 30 minutes under vacuum.

3.2.11   Synthesis of Silica Nanoparticles

Stöber method was used to synthesize silica nanoparticles with the size of 100 nm. Firstly, 3.6 ml of ammonium hydroxide was dissolved in 60 ml of ethanol by mixing for 1 hour. After that, 1.8 ml of TEOS was added slowly and then the solution was mixed for 1 hour at room temperature for 24 hours by using magnetic stirrer. Finally, the silica nanoparticles were settled down by using centrifuge and supernatant was replaced with ethanol to rinse the nanoparticles. Therefore, the chemicals were dissolved in ethanol and removed from the suspension of silica nanoparticles.

3.2.12   Preparation of Carboxylic Acid Terminated Silica Nanoparticles

Firstly, 0.138 ml of APTES and 25 ml of suspension of silica nanoparticles were stirred overnight at room temperature. Then, in order to remove the excess amount of silane molecules in the mixture, the nanoparticles were collected by using centrifuge and the supernatant was changed with ethanol for three times. A solution of 0.1 M succinic anhydride in DMF was prepared with the volume of 20 ml. Then, the silica nanoparticles dispersed in DMF was added to the solution of succinic anhydride slowly and stirred for 24 hours[94]. Lastly, the silica nanoparticles were rinsed three times with DMF and water, respectively.

3.2.13   Preparation of Silica Nanoparticles Functionalized with a Mixed-Monolayer

Firstly, 20 mg of previously synthesized silica nanoparticles was added to 1 ml of absolute ethanol and dispersed by using probe sonicator for 45 minutes. Then, a solution was prepared by mixing 1 ml of APTES and 200 µL of DMOAP in 9 ml of ethanol and suspension of nanoparticles were added in this solution and stirred for 1 hour at 80ºC. The next step was rinsing the nanoparticles with ethanol three times. Then, solution of 0.1 M succinic anhydride in DMF was prepared with the volume

of 20 ml. Then, the silica nanoparticles dispersed in DMF was added to the solution of succinic anhydride slowly and stirred for 24 hours. Lastly, the silica nanoparticles were rinsed three times with DMF and water, respectively.

3.2.14 Preparation of DMOAP Coated Silica Nanoparticles

The solution of 0.01% vol DMOAP in aqueous suspension of silica nanoparticles was prepared and sonication was applied for 15 minutes. After that the functionalized silica nanoparticles were collected by using centrifuge, rinsed with pure water and dispersed by using probe sonicator. This procedure was repeated for 10 times to remove the excess amount of silane molecules. In order to verify whether excess silane molecules were removed from the system, LC emulsion was formed in the final supernatant, and the configuration of the LC droplets was checked to ensure their bipolar configuration was maintained.

3.2.15 Measurement of Zeta Potential, Size and Concentration of Nanoparticles

The nanoparticles were dispersed in aqueous medium by using an ultrasonic probe and the zeta potentials and size of the nanoparticles were measured by using Dynamic Light Scattering (DLS, Zetasizer Ultra Malvern Instruments Ltd., US) at room temperature. For the measurement of concentration, firstly the size measurement of aqueous medium without nanoparticles was performed and "count rate" value was read to use in concentration measurement to eliminate the background.

3.2.16 Preparation of Mixture of Methyl Orange in Silica Nanoparticle Suspensions

DMOAP coated silica nanoparticle suspension was diluted to $\sim 10^9$ particles/ml. Desired concentrations of Methyl Orange (MO) were obtained by adding to the suspensions and stirred for 2 hours to equilibrate.

3.2.17 Synthesis of FITC Doped Core-Shell Silica Nanoparticles

1 mg of dye molecules FITC (Fluorescein-5-isothiocyanate) was dissolved in 1 ml of anhydrous ethanol by using ultrasonic bath. 5µl of APTES was added to solution and stirred for 24 hours while shielded from light. 3ml of TEOS, 2 ml of pure water and 4.8 ml of ammonium hydroxide and the conjugate was mixed for 3 hours at 40°C.

3.2.18 Analysis of Change in LC Orientation in Aqueous Medium

Epoxy microwells filled with 5CB was placed into a cuvette which is filled with the pure water. In the case of adsorption of surfactant molecules or the nanoparticles, the required concentration was calculated with respect to the total volume of pure water and the adsorbates were added gently to the medium by using micropipette. After waiting 1 hour, the images of the microwells were taken by using polarized optical microscope (Olympus BX53M microscope, Olympus Inc., Japan).

3.2.19 Imaging with Fluorescence Confocal Polarizing Microscopy (FCPM)

Images of microwells filled with the mixture of 1% wt of Nile Red ($\lambda_{ex} = 549$ nm, $\lambda_{em} = 628$ nm) and 5CB, and also FITC ($\lambda_{ex} = 495$ nm, $\lambda_{em} = 519$ nm) doped

silica nanoparticles adsorbed on the microwells were taken by using Zeiss LSM 900 (Zeiss, Jena, Germany) equipped with a rotatable linear polarizer and analyzer. For the mixture of Nile Red and 5CB the angle of polarizer and analyzer were changed and images were collected to understand the orientation of 5CB. Images were taken while pinhole was 78 μm, master gain was 750 V and intensity of the laser 561 nm was 2%. For FITC-doped silica nanoparticles, channel was selected as FITC and intensity of laser was 10%, pinhole was 78 μm and master gain was 750 V.

CHAPTER 4

RESULTS & DISCUSSION

The study described in this thesis was divided into three main parts. In the first part, we confined LCs into droplet geometry and analyzed the interparticle interactions of gold nanoparticles (AuNPs) and the positioning of them on LC-water interfaces. In the second part of the thesis study, we prepared water soluble microwells and developed a method for the determination of configuration of LCs confined in microwells in the case of LC-air interface. In addition, in order to analyze the LC configuration in the case of LC-water interface, we prepared stable and water insoluble microwells and determined the LC configuration by using previously developed method. Lastly, by using these microwells we performed the response tests to evaluate their usage in sensor applications.

4.1   Analyses on Interparticle Interactions and Positioning of Gold Nanoparticles at LC-Water Interfaces by Using LCs Confined into Droplet Geometry

In order to analyze the interparticle interactions and assemblies of the nanoparticles, we synthesized and characterized AuNPs whose surface was functionalized to control their surface properties. Then, we applied the response tests on 5CB droplets to analyze the effects of AuNP adsorption on the 5CB droplet configuration. We visualized the assemblies of nanoparticles on the polymerized LC droplet surface by using scanning electron microscope (SEM) and then correlated the positioning of nanoparticles with the results of configuration analysis performed by using polarized optical microscope. [95]

4.1.1   Synthesis and Characterization of Gold Nanoparticles

We synthesized citrate-capped AuNPs by using Turkevich method relied on reduction of chloroauric acid ($HAuCl_4$) with sodium citrate (TSC)[95]. After the synthesis of AuNPs, we analyzed the size distribution by using Dynamic Light Scattering (DLS). As shown in Figure 4.1, we achieved to synthesize monodispersed AuNPs in the sizes of nearly 40, 100 and 120 nm. In order to tune the size of the nanoparticles, the time for the heating step was adjusted such that when the solution was heated for longer time the size of the nanoparticles was increased.
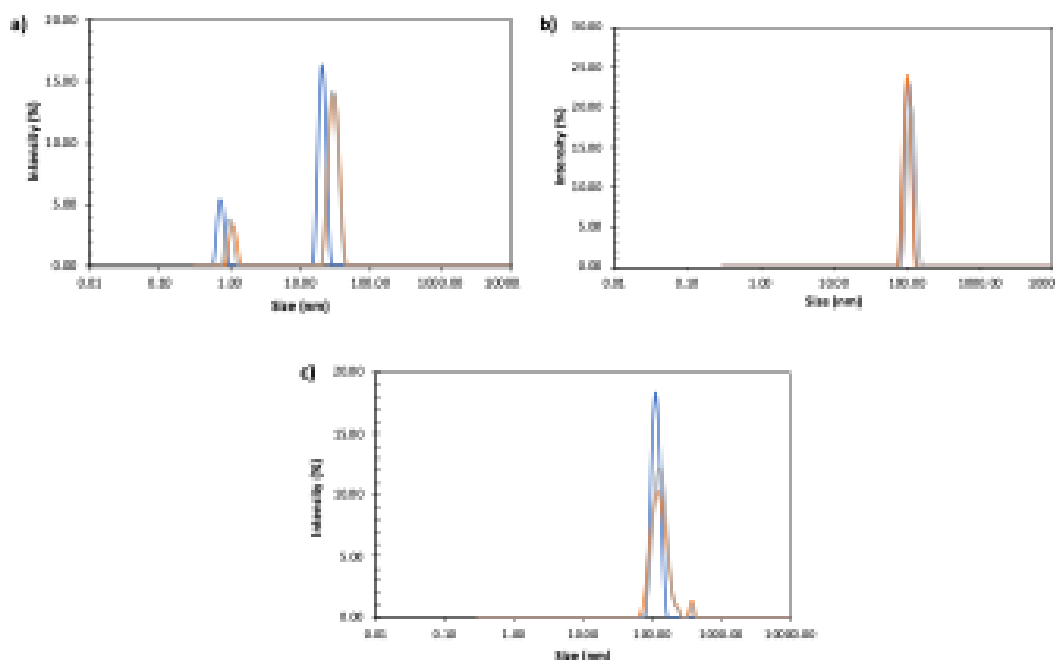
Figure 4.1 Results of size analysis of synthesized gold nanoparticles with the size of a) 40, b) 100 and) 120 nm

Then, we compared the results came from DLS and the analysis of SEM micrographs of AuNPs and found that the average size was 44.4 ± 9.3 and 39.5 ± 1.8 nm, respectively. The p-value was 0.46 which was higher than 0.05 (significance level), so it could be said that the same results were obtained with these methods. Therefore, there was no hydration layer around the nanoparticles affecting the size of AuNPs measured by DLS and it also showed that surface of nanoparticles was not

hydrophilic. In addition, when we performed elemental analysis with EDX, the signals came from gold elements were easily seen as shown in Figure 4.2 .
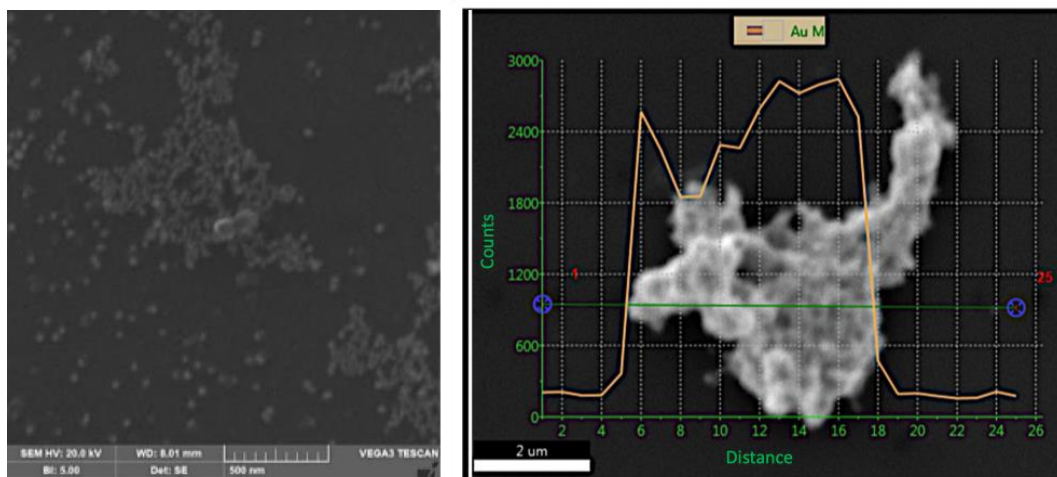
Figure 4.2 SEM micrograph and EDX analysis of aggregates of gold nanoparticles

4.1.2   Mixed Monolayer Coated Gold Nanoparticles

In addition to the size of nanoparticles, the surface property of them was another key parameter for the analysis of the behavior at LC-water interface. The surface property of nanoparticles determines the hydrophobicity/hydrophilicity, electrostatic interactions and surface anchoring of LC. Therefore, it was important to specify the surface property of the nanoparticles to control their effects on the adsorption of nanoparticles and the formation of their assemblies. For this purpose, we focused on the parameters which were chemicals used for the surface functionalization, composition of these chemicals, ion concentration and pH of the medium in the experiments.

4.1.2.1   Decanethiol (C10) and Hexadecane thiol (C16) Coated Gold Nanoparticles

It has been known that the carbon chain length of the molecules used for the surface functionalization plays an active role in controlling the properties such as

hydrophobicity/hydrophilicity of the surfaces, as well as the anchoring of the LC on the surfaces[96,97]. Therefore, we decided to examine the possible effects by coating the AuNP surface with decanethiol (C10) and hexadecane thiol (C16) molecules at certain compositions. In addition to the composition, we adjusted the ion concentration of aqueous medium by adding the salt (NaCl) to control the interparticle and also nanoparticle-LC interaction by adjusting the electrostatic interaction.

4.1.2.1.1 Effects of the Composition in the case of Mixed Monolayers Created with Hydrocarbons

With mixed monolayer (MML) structures formed by using the chemicals with carbon chains in different length which were C10 and C16, we aimed to investigate the effect of the composition on the surface properties of the particles and also the behavior at the LC-water interface.

In line with this goal, mixed monolayer structures were formed by using C10 and C16 with the molar ratios of [1:4], [1:1] and [4:1]. After the functionalization process, we measured the zeta potential values of the suspensions of mixed monolayer coated AuNPs in aqueous medium with the concentration of 10^7 particles/ml in the case of the compositions of C16 to C10 as [1:4], [1:1] and [4:1]. As shown in Figure 4.3, the zeta potential value was around -20 mV while the [C16:C10] ratio was [1:4], and moved towards the -30 mV with the increase in the C16 ratio. Since C10 and C16 molecules were neutral molecules, the reason of these small differences between the zeta potential value is the composition and arrangement of the chemicals adsorbed on the surface of nanoparticles[98].

Figure 4.3 Zeta potential measurement results of mixed monolayer functionalized gold nanoparticles with different C16:C10 values ([1:4], [1:1], [4:1])

The configuration of LC droplet depends on the interfacial anchoring. When there is an alteration at the interface such as adsorption of molecules or colloids, the interfacial anchoring of LC is modified and the configuration of LC droplets changes depending on the anchoring. The micrographs taken by polarized optical microscope and schematics of LC droplet configurations in the case of planar, tilted and homeotropic anchoring were represented in Figure 4.4. When the anchoring of the LC is planar, LC droplet has the "bipolar" configuration (Figure 4.4a). In this configuration, two topological defects locate at the poles of the droplet. As the interfacial anchoring changes from planar to homeotropic, the location of defect also changes and moves from poles to a point on the surface and a configuration is formed called as pre-radial during this transition (Figure 4.4b). When the interfacial anchoring is totally homeotropic, defect locates at the center of the droplet and this configuration is called as "radial" (Figure 4.4c)[35,36,78,99].
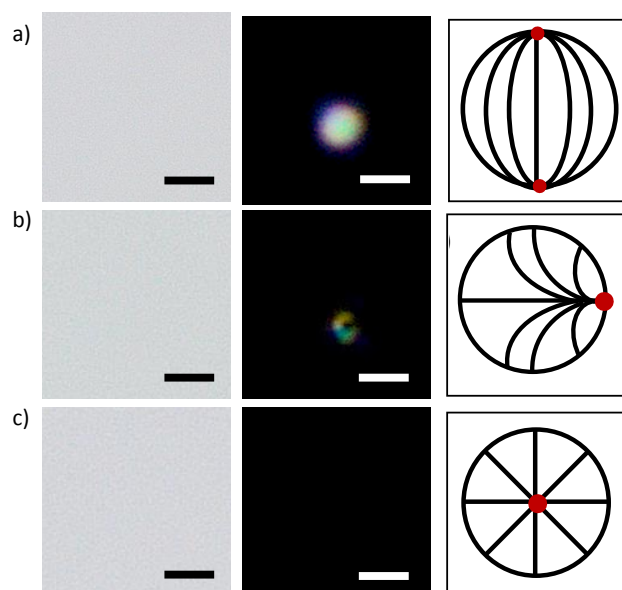
Figure 4.4 The optical microscope images and the schematics of the LC droplets in different configurations a) bipolar b) pre-radial c) radial configuration (red dots represent the defects)

When we examined the droplet configuration distribution after the adsorption of the nanoparticles, we found that the frequency of droplets with the pre-radial configuration increased with the increase of C16 composition as shown in Figure 4.5. The percentage of bipolar configuration, which was approximately 54.7 ± 3.5 % when the [C16:C10] ratio was [1:4], dropped to approximately 35.9 ± 3.7% when the ratio was [4:1]. When we increased the composition of C16 molecules in the medium during the surface functionalization of AuNPs, we had created an environment that promoted the adsorption of the molecule with a long carbon tail onto the surface. Therefore, we made the particles possess a more hydrophobic surface, which directly influenced their distribution in aqueous medium and their tendency to adsorb onto interfaces. The increased hydrophobicity of the particle surface might trigger movement towards the LC-water interface, thereby facilitating the adsorption of more particles. Moreover, it could cause the aggregation of particles suspended in an aqueous medium and the nanoparticles might be adsorbed at LC-water interface in the form of aggregates. Thus, AuNPs were not adsorbed

40

uniformly onto the droplet surface. As a result, the aggregates of AuNPs tended to preferentially adsorb to defect regions where the energy penalty was present. Therefore, interfacial anchoring was not subjected to a symmetric effect influencing the entire geometry and thus we observed more pre-radial configuration instead of radial configuration[71].
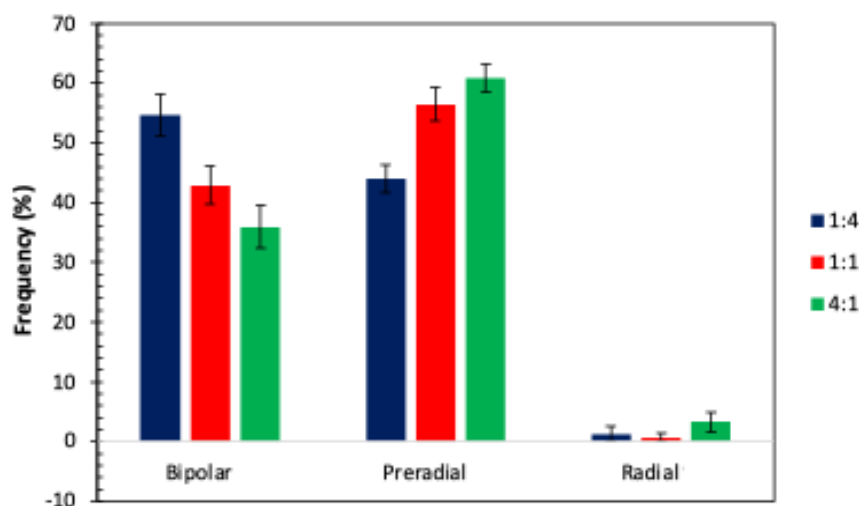
Figure 4.5 The results of the response tests of MML coated AuNPs for different compositions of C16:C10 which are [1:4], [1:1], [4:1]

Then, we used SEM to visualize the distribution of AuNPs on the surface of droplet after the adsorption. For this purpose, we polymerized the mixture of 20% wt of RM257 and 80% wt of 5CB after the adsorption of AuNPs. After the polymerization, we extracted 5CB by dissolving in ethanol and took the micrographs of the surface of polymerized droplets. Since AuNPs have the scattering property, the distribution of AuNPs on the surface of 5CB droplet could be visualized by imaging with backscattered mode. As shown in Figure 4.6, the distribution of nanoparticle assemblies on the 5CB droplet was dependent on the composition of alkanethiols forming the mixed monolayer on nanoparticles. When the composition of [C10:C16] was [1:4] in the medium used for the surface functionalization, we observed that the nanoparticles formed aggregates rather than dispersing homogenously in the aqueous medium.
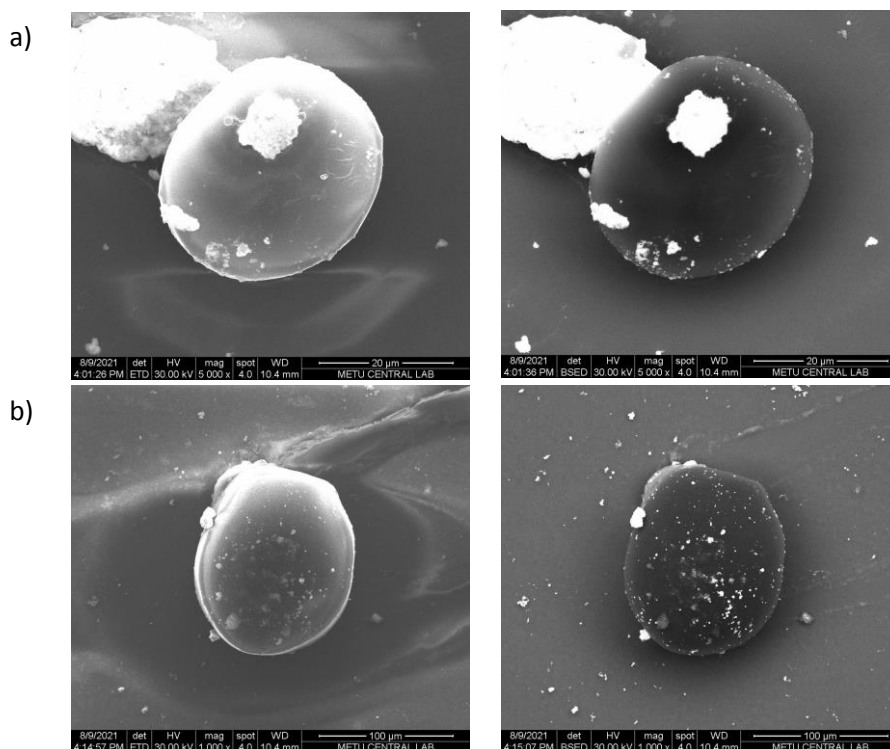
Figure 4.6 SEM images of polymerized droplets taken after functionalized gold nanoparticles were adsorbed with the ratio of [C10:C16] determined as a) [1:4], b) [4:1]

4.1.2.1.2 Effects of the Ion Concentration of Medium in the case of Mixed Monolayers Created with Hydrocarbons

Although C10 and C16 molecules are not charged molecules, due to the negative charge of the citrate-coated gold nanoparticles, there was an interaction between the particles. Therefore, we aimed to investigate the electrostatic interaction between particles by adjusting the ionic strength with addition of salt (NaCl) to the aqueous medium. In line with this goal, the characterization was carried out using 1, 5, 20, 50 and 100 mM NaCl medium.

Firstly, we measured the zeta potential values (Figure 4.7) with respect to the changed in salt concentration. In the absence of salt in an aqueous environment, the zeta potential value was about -35 mV and this value was decreased to a range

between -10 and -15 mV with the increase in the salt concentration. After 20 mM, there was no significant change in zeta potential values. In order to check whether the addition of salt to the medium has an effect on the nanoparticle distribution at the LC-water interface and thus on the LC droplet configuration, we investigated the distribution of droplet configuration when the salt concentration in the medium was 20 mM (Figure 4.8). As it can be seen in Figure 4.8, the percentage of pre-radial configuration, which was about 60 ± 3.3 % in the absence of salt, reached only about 64.7 ± 3.2 % when the salt concentration was increased to 20 mM. We interpreted this as the addition of 20 mM salt to the medium did not create a significant change in the LC droplet configuration. The reason of this was that the zeta potentials of both 5CB droplet and AuNPs were in negative region in the case of 20 mM salt concentration in aqueous medium and the interaction between 5CB droplet and AuNPs was limited at this condition.
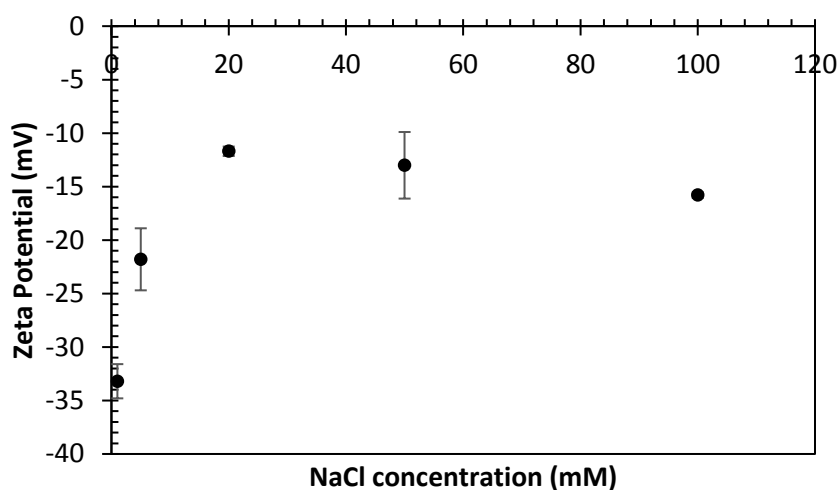
Figure 4.7 Zeta potential measurement results of gold nanoparticles functionalized with [C10:C16] ratio [1:4] at different salt (NaCl) concentrations.
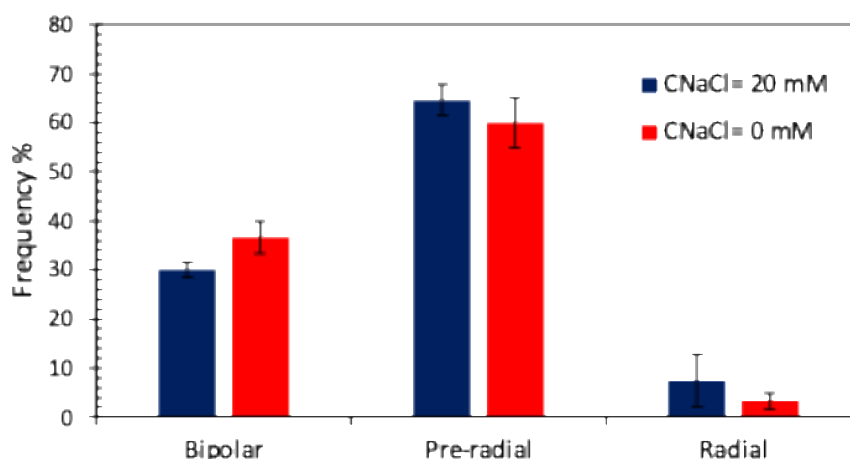
Figure 4.8 The distribution of configuration of 5CB droplets in the case of $C_{NaCl}=0$ and $C_{NaCl}=20$ mM

4.1.2.1.3 Effects of the Time in the case of Mixed Monolayers Created with Hydrocarbons

In order to investigate whether the time elapsed during the interaction of functionalized AuNPs and 5CB droplets has an effect on the droplet configuration or not, we examined the distribution of 5CB droplet configuration by polarized optical microscope with respect to the time. In this way, we aimed to examine whether the adsorption of nanoparticles on the 5CB droplet surface, or their possible movements on the droplet surface have an effect on the LC droplet configuration.

For this purpose, we analyzed the distribution of 5CB droplet configuration by collecting images under an optical microscope with cross polarizers at the end of the 10th minute, 1st hour and 2nd hour while LC droplets were exposed to the suspension of functionalized AuNP suspension. As seen in the graph represented in Figure 4.9, the frequency of bipolar droplets, which was about 46.7 ± 1.7 % after 10 minutes, decreased around 36.7 ± 3.3 % after the 1st hour and stayed around 41.7 ± 4.4 % after the 2nd hour. This was interpreted as the positioning of the particles on the LC-water interface was changed rapidly until the first hour (p-value was 0.02), and became more stable after the 1st hour (p-value was 0.2).

44
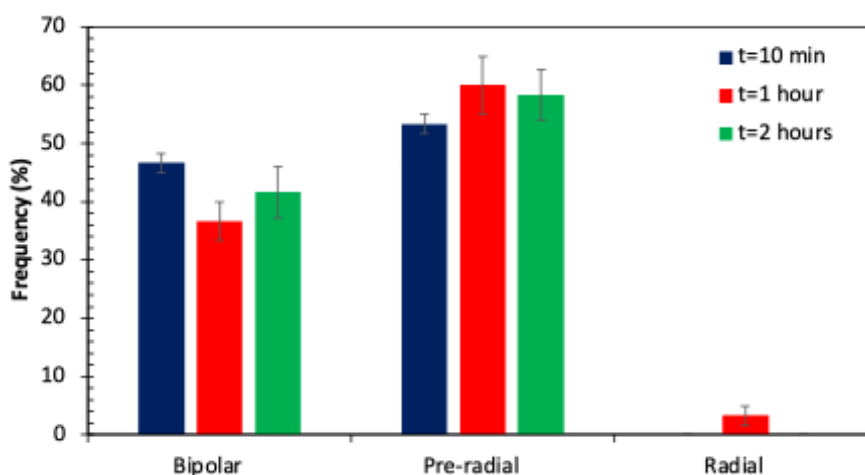
Figure 4.9 The results of the response tests at t=10 min, 1h, 2h in the case of mixed monolayer of the mixture of C16 and C10 with the composition of [4:1].

4.1.2.2 11-Mercaptoundecanoic acid (COOH) and Hexadecanethiol (C16) Coated Gold Nanoparticles

After studies with AuNPs functionalized with a mixed monolayer prepared with C10 and C16, we used COOH and C16 to functionalize the surface of AuNPs. The purpose of using carboxylic acid was providing pH dependent electrostatic interaction. In addition to the electrostatic effect, we aimed to reduce the aggregation due to its hydrophilic feature.

4.1.2.2.1 Effects of the Composition in the case of Mixed Monolayers Created with COOH and C16

We aimed to observe the effect of the hydrophilicity and electrostatic interactions on the nanoparticle adsorption and hence LC droplet configuration by changing the mixing ratio of COOH and C16. For this purpose, we adjusted the ratio of [COOH:C16] as [4:1], [1:1] and [1:4]. After the functionalization process, we investigated the effect of the composition change on the surface charge and stability by measuring the zeta potential. As given in Figure 4.10, while [COOH:C16] ratio

was changed as [4:1], [1:1] and [1:4], no significant change was observed in the zeta potential values, and it was observed that it remained at nearly -30 mV. AuNPs functionalized with the carboxyl group have a negative charge in the neutral regions of the medium in the case of the composition of [4:1], [1:1] and [1:4].
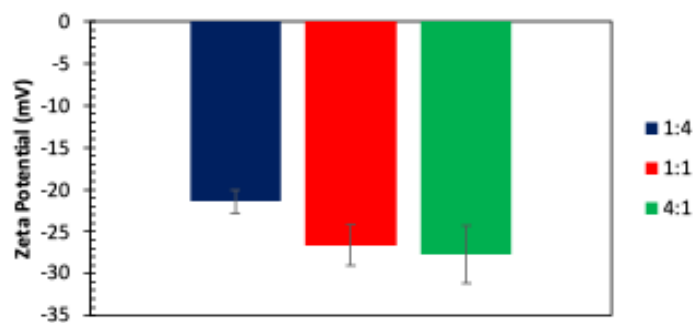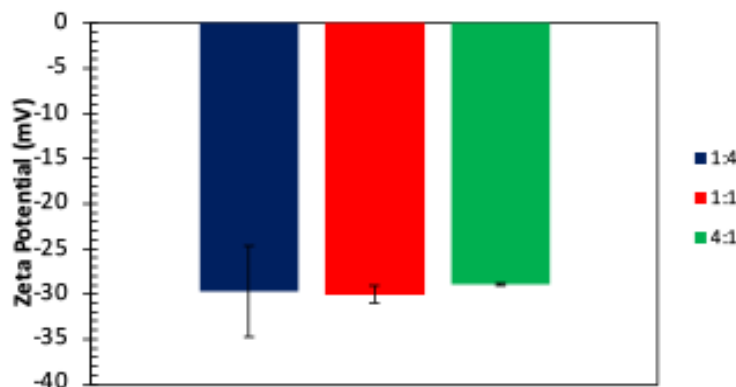

Figure 4.10 Zeta potential measurement results of mixed monolayer functionalized gold nanoparticles with different COOH:C16 values ([1:4], [1:1], [4:1])

After the zeta potential measurement, we investigated the change in distribution of droplet configuration in the case of adsorption of AuNPs functionalized with a mixed monolayer prepared by using a medium with compositions of [1:4], [1:1] and [4:1]. We found that in the cases of the composition of [COOH:C16] were [4:1] and [1:4], the frequency of droplets with pre-radial configuration was about 36.1 ± 2.0 % and 45.6 ± 3.0 %, respectively as represented in the graph shown in Figure 4.11. The reason for this increase was the fact that nanoparticles coated with [1:4] ratio were more hydrophobic and may have a greater tendency to adsorb on 5CB droplet, or that the aggregated nanoparticles may cause pre-radial configuration again. For this reason, we visualized the droplet surfaces by using SEM. As seen from Figure 4.12, when the ratio of [COOH:C16] in the medium for the functionalization was adjusted as [1:4] (Figure 4.12a) , and [4:1] (Figure 4.12b), the number of nanoparticles on the surface was lower when the ratio was [4:1]. We considered the reason for this situation that AuNPs with a more hydrophobic [COOH:C16] ratio [1:4] had a higher tendency to adsorb on the 5CB droplet.

46
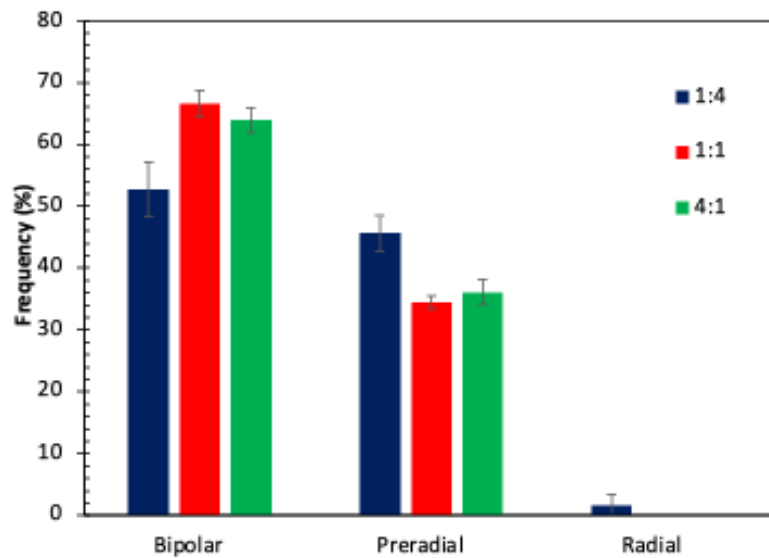
Figure 4.11 The results of the response tests of MML coated AuNPs for different compositions of COOH:C16 which are 1:4, 1:1, 4:1
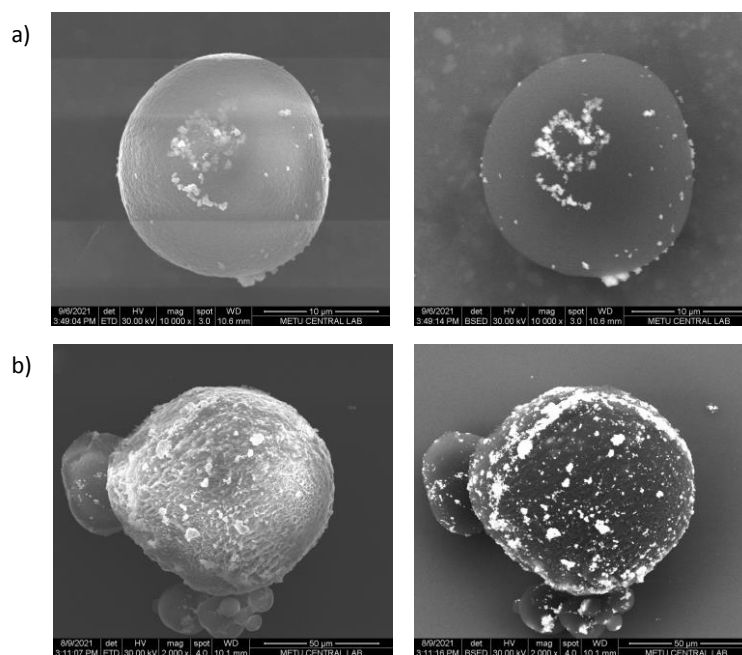
Figure 4.12 Scanning electron microscopy micrographs of polymerized droplets taken after the functionalized gold nanoparticles were adsorbed on droplets with the [COOH:C16] ratio determined as a) [4:1], b) [1:4]

4.1.2.2.2   Effects of the Ion Concentration of Medium in the case of Mixed Monolayers Created with CCOH and C16

Since the carboxyl group is a charged group, it paves the way for controlling nanoparticle interactions by adjusting pH and ion concentration in the medium. For this reason, in order to investigate the effect of the number of ions in the environment on the nanoparticle interaction, we aimed to examine the behavior of the nanoparticles at the LC-water interface by adding salt (NaCl) to the aqueous medium.

Zeta potential values were measured by adding NaCl in molarities of 5, 10, 20, 50, 100 mM to the aqueous medium. As shown in Figure 4.13, it was observed that the zeta potential value did not undergo a significant change after 20 mM and remained around -10 mV. Therefore, the salt concentration was set to 25 mM and we examined the distribution of droplet configuration by using polarized optical microscope. We observed that the bipolar configuration, which was approximately 55.7± 3.5%, increased to 63.3± 2.0 % when the salt concentration was 25 mM as shown in Figure 4.14. Considering that this situation might be caused by the movement of the adsorbed nanoparticles on the LC droplet surface or the decrease in the number of adsorbed nanoparticles, we visualized the polymerized LC droplet surface by using SEM. As it can be seen in the sample SEM micrograph shown in Figure 4.15, there was a decrease in the number of adsorbed nanoparticles and also, we observed an increase in the number of non-adsorbed aggregated nanoparticle. Therefore, we thought that the interparticle attraction was greater than LC-nanoparticle attraction and thus the tendency of the nanoparticles to adsorbed on 5CB droplet interface was decreased.
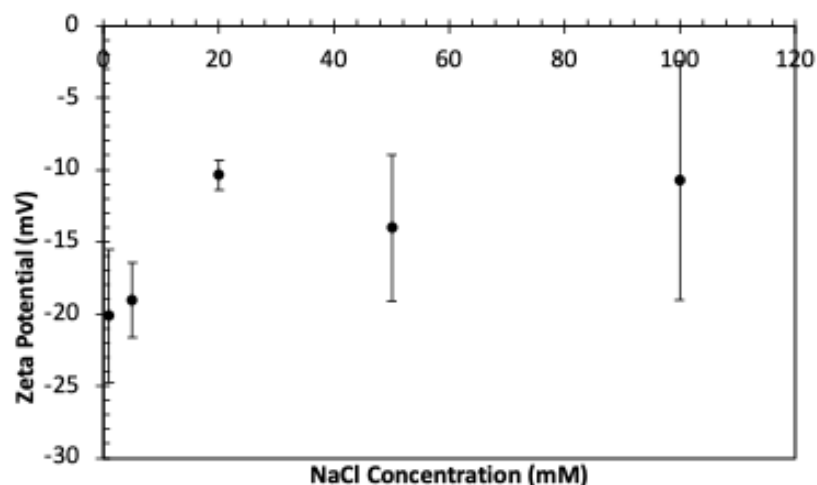
Figure 4.13 Zeta potential measurement results of gold nanoparticles functionalized with [COOH:C16] ratio [1:4] at different salt (NaCl) concentrations
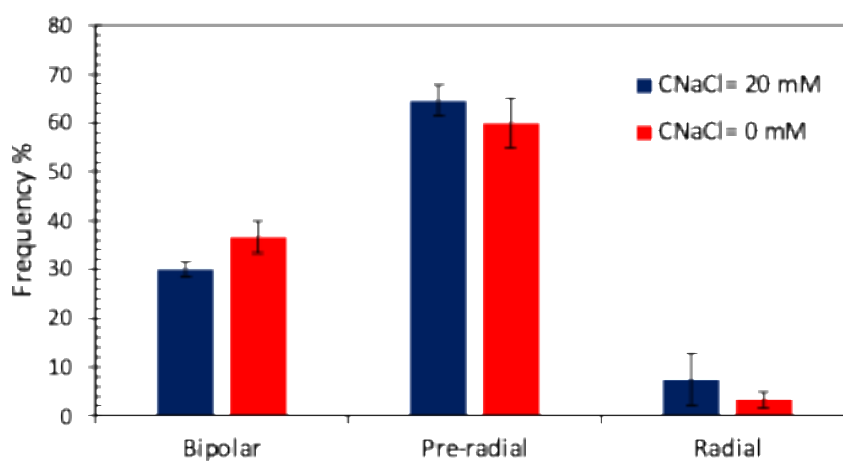
Figure 4.14 The distribution of droplet configuration after adsorption of the functionalized gold nanoparticles as a mixed monolayer when NaCl concentration of the aqueous medium was 0 mM and 25 mM, the [COOH:C16] ratio was [1:4]

49
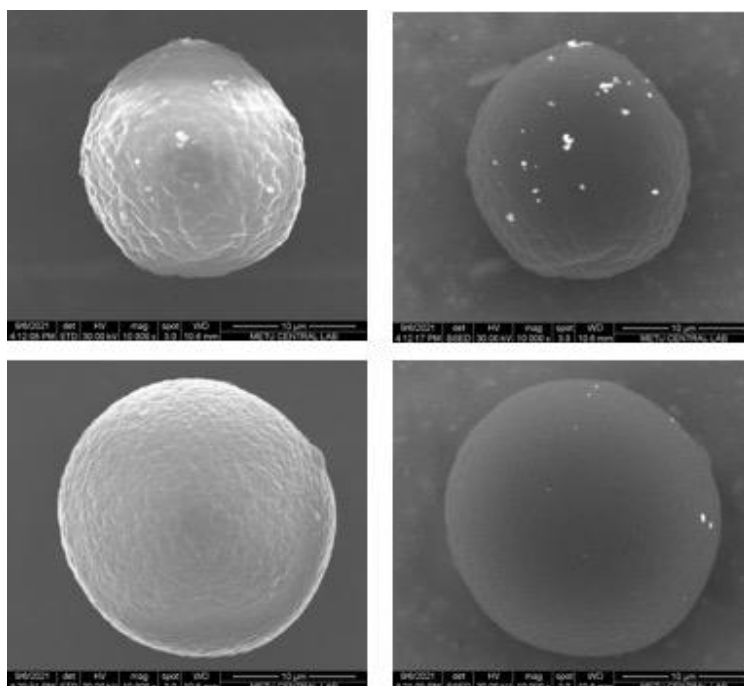
Figure 4.15 Scanning electron microscope images of polymerized droplets in the case of the adsorption of gold nanoparticles coated with a mixed monolayer with a [COOH:C16] ratio of [1:4] at a salt concentration of 25 mM in the medium.

In order to examine the effect of changing the salt concentration after adsorption on the 5CB droplet configuration, we adjusted the salt concentration of the medium by dilution and addition of salt.

Firstly, the salt concentration of medium was 100 mM and after 1 hour, we diluted to 50 mM and 25 mM, respectively. The configuration distribution was analyzed for each concentration value. With the dilution of the salt concentration in the environment, we observed a decrease in the pre-radial configuration (Figure 4.16). At 100 mM salt concentration, the percentage of pre-radial configuration was 55.0 % and it reached 49.3± 3.5 % and 33.3± 1.7 % by dilution to 50 and 25 mM salt concentrations, respectively. Since the energy required for the possible desorption process was at a high level such as $\sim 10^5$ k_BT, r, and this effect might be directly due to the salt concentration or the time elapsed during the waiting period.

Then, we increased the concentration of medium prepared as 50 mM to 65 and 75 mM after each 1 hour and analyzed 5CB droplet configuration at these

concentrations. We observed that the number of droplets with radial configuration increased with the increase in salt concentration. The percentage of radial configuration was 2.9± 1.7% and 21.9± 12.7% in the case of 50 mM and 75 mM salt concentration, respectively as represented in Figure 4.17.

Considering that these behaviors might be caused by the salt concentration or the time elapsed until the analysis with the optical microscope, we analyzed 5CB droplet configuration with respect to time.
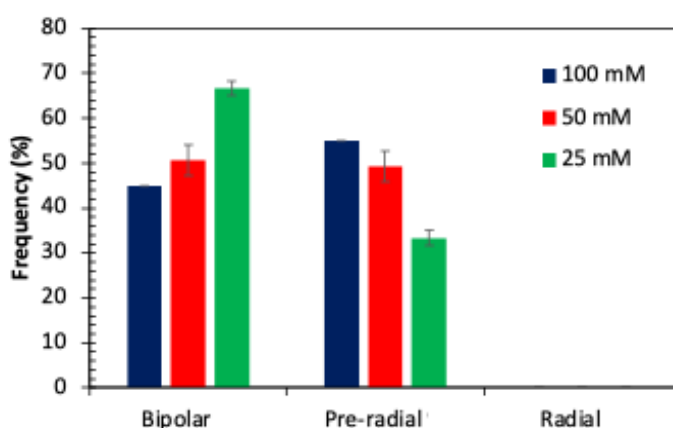
Figure 4.16 The distribution of 5CB droplet configuration when the salt concentration in the aqueous medium was 100, 50 and 25 mM (50 and 25 mM concentration was obtained by dilution of 100 mM medium.)
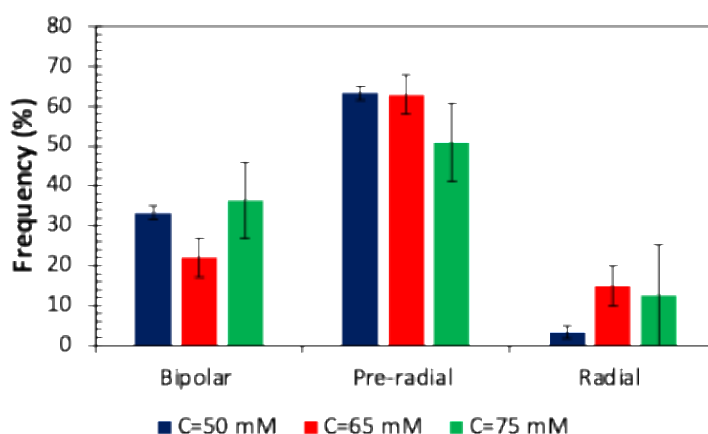
Figure 4.17 The distribution of 5CB droplet configuration while the salt concentration in the aqueous medium was 50, 65 and 75 mM, (65 and 75 mM concentration was obtained by increasing the concentration of 50 mM medium.)

4.1.2.2.3 Effects of the Time in the case of Mixed Monolayers Created with COOH and C16

In addition to the varying parameters in the experiments, we examined whether the elapsed time had an effect, as well as whether a steady-state condition was reached, by analyzing the time-dependent 5CB droplet configuration distribution under POM. For this reason, we performed 5CB droplet configuration analysis at different time intervals during the interaction of droplets with the functionalized gold nanoparticles. As seen in Figure 4.18, we observed a significant increase in the pre-radial configuration until the first hour (p-value was 0.04), but we did not observe any obvious change after the first hour (p-value was 0.8).

In order to simulate the time passed in the experiments performed to analyze 5CB droplet configuration in the case of varying salt concentration or nanoparticle addition, we captured the micrographs of LC droplets at 1st hour and 5th hour under POM as a control experiment. As seen in Figure 4.19, the pre-radial percentage, which was approximately $44.3 \pm 3.5\%$ at the 1st hour, decreased to approximately $19.7 \pm 2.9\%$ after the 5th hour.
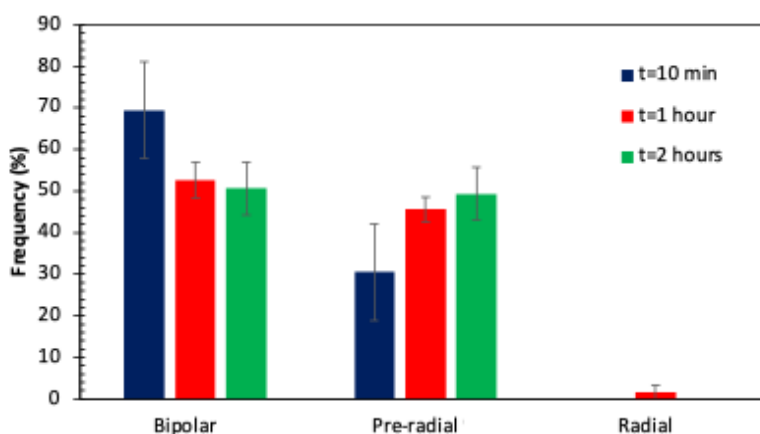
Figure 4.18 The distributions of the configuration of 5CB droplets after 10 minutes, 1 hour and 2 hours interaction of COOH and C16 with functionalized gold nanoparticles in a ratio of [1:4]
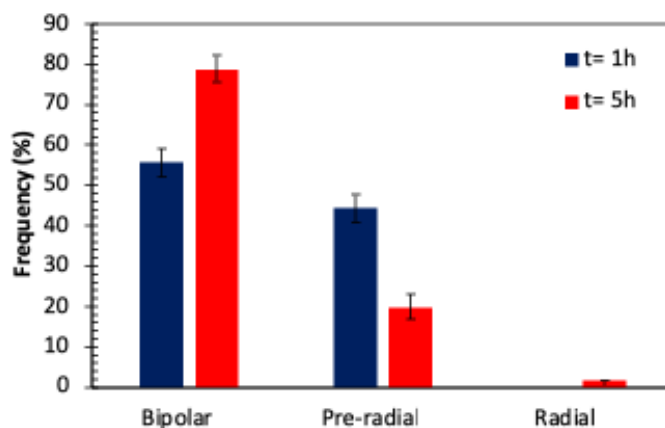
Figure 4.19 The distributions of 5CB droplet configuration after 1 hour and 5 hours of interaction of COOH and C16 with functionalized gold nanoparticles in a ratio of [1:4]

In order to clarify the reason of this decrease in the frequency of pre-radial configuration, we analyzed the 5CB droplet configuration distribution in the absence of any nanoparticles or salts in the medium. Thus, we aimed to understand whether there was a change in the configuration of 5CB droplets when there was no adsorbate in medium. As seen in Figure 4.20, in the absence of nanoparticles and salt, 5CB droplet configuration was almost the same after the 1st and 5th hours. Thus, it has been proven that there was no change in the configuration of 5CB droplets in the absence of adsorbates in the medium.
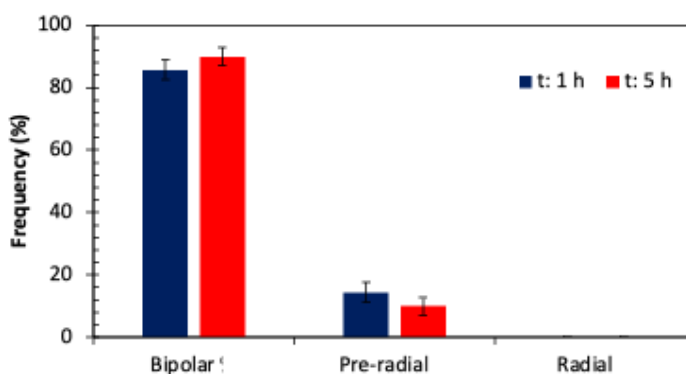
Figure 4.20 Configuration distributions of 5CB droplets after 1 hour and 5 hours in nanoparticle and salt-free environment

As another control experiment, we aimed to understand the effect of time on the configuration distribution by analyzing 5CB droplets in environments with different salt concentrations for certain time periods and examining the configuration distribution. As seen in Figure 4.21, there was no time-dependent change in 5CB droplet configuration even if the salt concentration increased in the absence of nanoparticles.
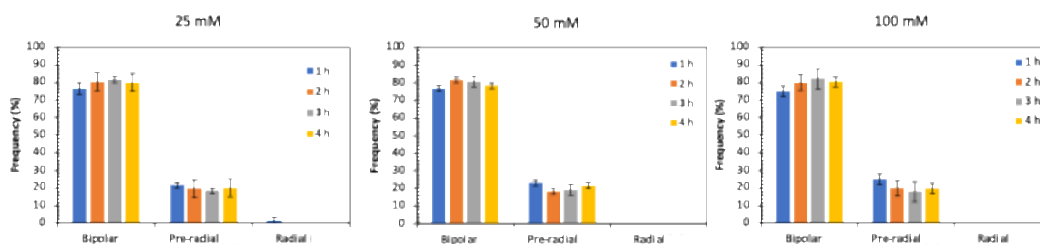
Figure 4.21 The distributions of configuration of 5CB droplets after 1, 2, 3 and 4 hours in environments without nanoparticles and at different salt concentrations (25, 50 and 100 mM)

Since in the case of absence of nanoparticles in the environment, there was no time-dependent change in 5CB droplet configuration, even if there was salt in the environment, new experiments were designed to investigate the behavior of AuNPs at 5CB-water interface. Within the scope of these experiments, we aimed to investigate the effect of nanoparticle surface properties on time-dependent behavior by using AuNPs that were functionalized using different methods.

The configurations of 5CB droplet were investigated in the case of the adsorption of AuNPs functionalized with the mixed monolayer of COOH and C16 with the ratio of [1:4] and [4:1] and also COOH monolayer comparing the distributions at 1st and 5th hour. As it can be seen in Figure 4.22, AuNPs which were functionalized with a mixed monolayer represented similar behavior with AuNPs functionalized with just only the molecule having highest composition in mixed monolayer. For example, in the case of [COOH:C16] ratio [1:4], the percentage of pre-radial configuration was 44.3± 3.5% after 1 hour and decreased to 19.7± 2.9 % after 5 hours. When we examined the results of the experiment with AuNPs functionalized with the C16 molecule, which was the molecule with the higher composition in mixed monolayer,

the percentage of pre-radial configuration decreased from approximately $23.3 \pm 7.3\%$ to 13.3 ± 6.0 % with time. Likewise, in the case of [COOH:C16] ratio [4:1], the percentage of pre-radial configuration was 39.3 ± 3.5 % after 1 hour and increased to $52.3 \pm 2.3\%$ after 5 hours. When we examined the results of the experiment with AuNPs covered with monolayer of COOH molecule to understand the effect of COOH molecules in the mixed monolayers while they have higher composition such that the ratio of [COOH:C16] was [4:1], the percentage of pre-radial configuration, which was 6.7 ± 1.7 % after 1 hour, increased to 14.7 ± 2.9 % after 5 hours.

We proposed that the reason of change in 5CB droplet configuration with the time in the case of adsorption of AuNPs functionalized with different methods might be the mobility of nanoparticles on the interface of LC-water due to the electrostatic interaction or hydrophilicity of the surface of nanoparticles. For this reason, we performed experiments to understand whether the electrostatic interaction triggers a nanoparticle movement that might have an effect on the configuration of 5CB droplets. For this purpose, the experiments whose results were presented in Figure 4.22 were repeated by using AuNPs which were functionalized with neutral hydrocarbon molecules. Thus, it was aimed to compare the behavior of AuNPs functionalized using uncharged C10 and C16 molecules with those of AuNPs functionalized with charged COOH molecule and to examine the electrostatic effect. We analyzed 5CB droplet configuration after the 1st and 5th hours in the case of adsorption of AuNPs functionalized as a C10 monolayer, a mixed monolayer with a [C10:C16] ratio of [1:4], and a C16 monolayer. Analysis results were given in Figure 4.23.
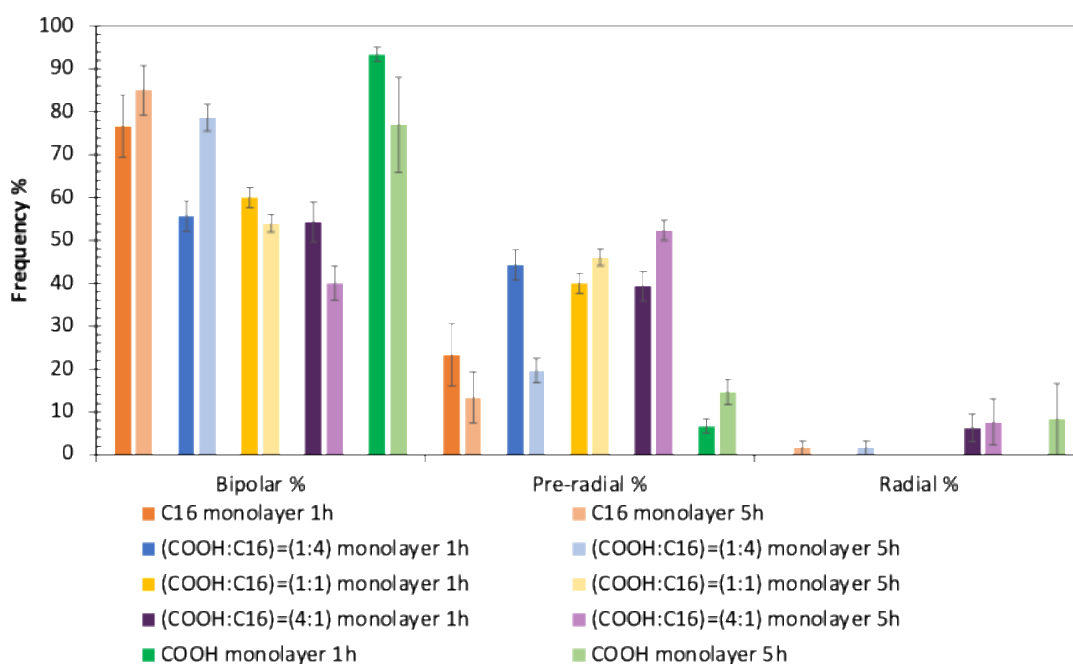
Figure 4.22 5CB droplet configuration distribution after exposure of liquid crystal droplets to gold nanoparticles functioning as C16 monolayer, [COOH:C16] ratio mixed monolayer and COOH monolayer for 1 and 5 hours

When we examined the graph in Figure 4.23, we observed that the time-dependent behavior of AuNPs coated with C10 and C16 as monolayer was different. In the cases where AuNPs functionalized with monolayers of C10 and C16 were used, the percentage of bipolar configuration that was almost the same after 1 hour is $80\pm 5.1\%$ and $76.7\pm7.3\%$, respectively, while in experiments using AuNPs functionalized with monolayer of C10, the percentage of bipolar decreases to approximately $57.3\pm 1.5\%$ after 5 hours. However, in the case of AuNPs coated with monolayer of C16, the frequency of bipolar droplets was increased to $85\pm 5.8\%$ after the 5th hour.
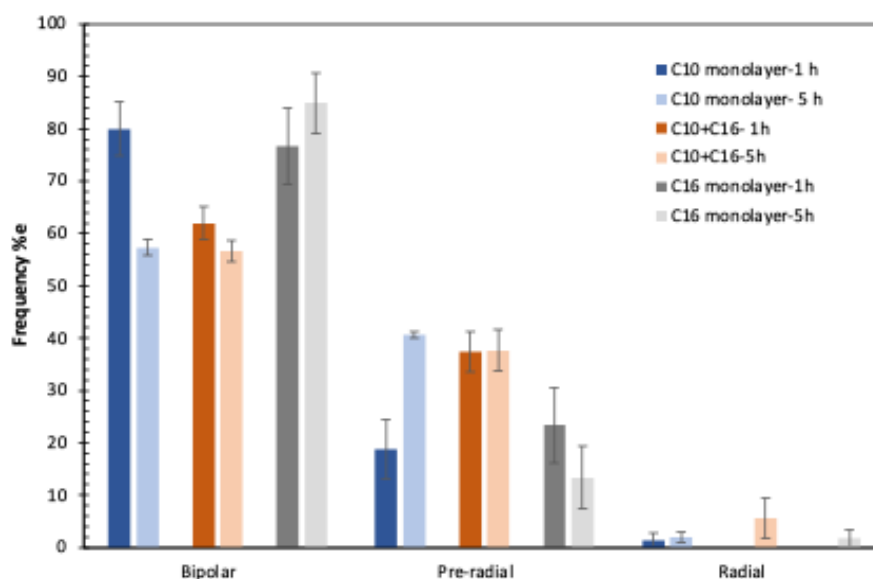
Figure 4.23 5CB droplet configuration distribution after exposure of liquid crystal droplets to gold nanoparticles functioning as C10 monolayer, [C10:C16] ratio mixed monolayer and C16 monolayer for 1 and 5 hours

When we compared the results obtained from the experiments consisting AuNPs functionalized with COOH and C10, we observed an increase in the pre-radial configuration was observed over time in the experiments with more hydrophilic gold nanoparticles, while the percentage of pre-radial droplets was decreased over time in the more hydrophobic gold nanoparticles. For this reason, we evaluated that the time dependent configuration change was due to the surface properties rather than the charge effect. In order to support these evaluations, we decided that surface images should have been taken with a scanning electron microscope to be able to have information about the positioning of the nanoparticles at the interface and to compare with the analyzes made with a polarized optical microscope. Therefore, we used an image processing method to determine the positions and also the size distribution of the gold nanoparticles adsorbed on the droplet surface. Figure 4.24 shows an example from the image processing method. With this method, we eliminated the background and measure the area where the gold nanoparticles located on the surface of the droplet. Therefore, we could calculate the size distribution of the aggregates on the surface and compare this distribution with time.
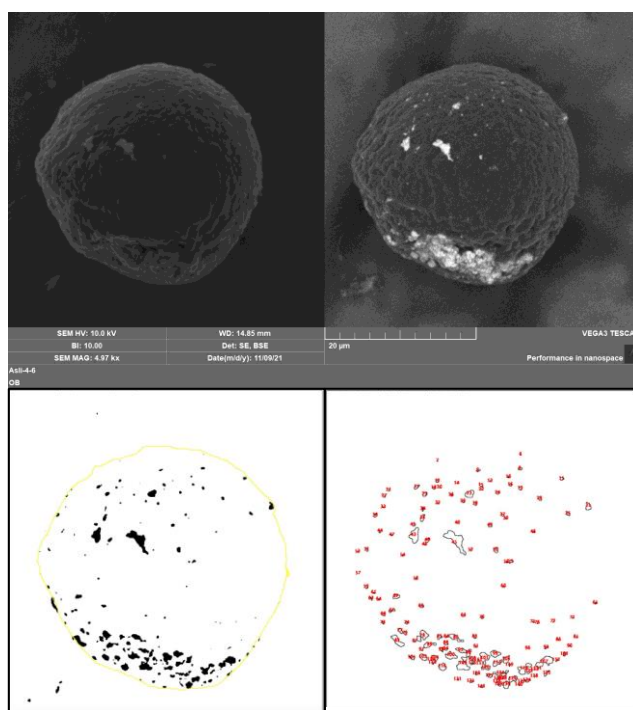
Figure 4.24 SEM images taken by using secondary electron detector and four quadrant back scattered detector in upper row, results of the image processing that show the position of the gold nanoparticles in second row.

As it can be seen from Figure 4.25, the frequency of the gold nanoparticles with the size in the range between 0-200 nm increases with the time. Since the size of a single nanoparticle was around 100 nm, this increase indicated an additional adsorption on the droplet surface. In addition, when we focused on the frequency of gold nanoparticles with the sizes higher than 2 μm, we observed that the number of larger aggregations was higher in the case of mixed monolayers and C16 monolayers comparing with COOH monolayer. We attributed this aggregation to the surface property of AuNPs because the surface of AuNPs functionalized with C16 and mixed monolayers was more hydrophobic than ones functionalized with COOH monolayer. Therefore, larger aggregates were formed, resulting in a pre-radial configuration of the droplets. When the size of the aggregates was large enough to create distortion in LC orientation, LC droplets might have an appearance of pre-radial configuration. When the sonication was not applied to the gold nanoparticles before the adsorption, we observed that the number of aggregates with the size larger than 2 μm was higher

than the case of sonication (Figure 4.26). Also, the number of gold nanoparticle with size in the range of 0-200 nm was decreased with time in the case of sonication. The reason of this decrease was that the aggregation of nanoparticles had started in 5th hour, whereas the nanoparticles had already formed in the case of no sonication. In addition, when we compared the results obtained from POM, the number of droplets with pre-radial configuration increased with time in the case of sonication whereas there was no significant change in the frequencies in the case of sonication.
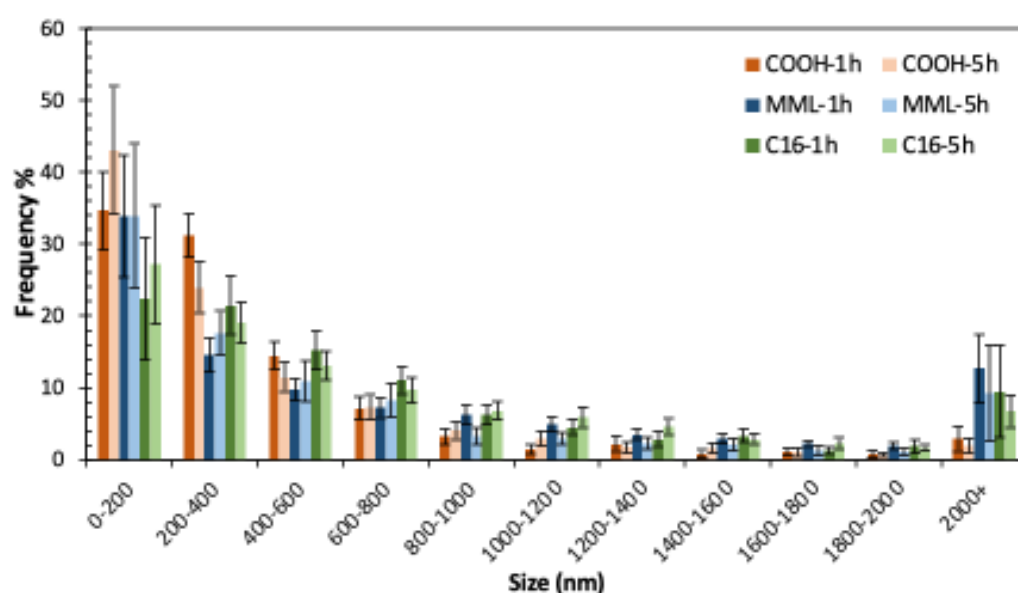
Figure 4.25 The size distribution of the gold nanoparticles located on the surface of droplet with respect to time for the gold nanoparticles functionalized as carboxyl monolayer, C16 monolayer and mixed monolayer with the composition of [COOH:C16] = [1:4] obtained from SEM images.
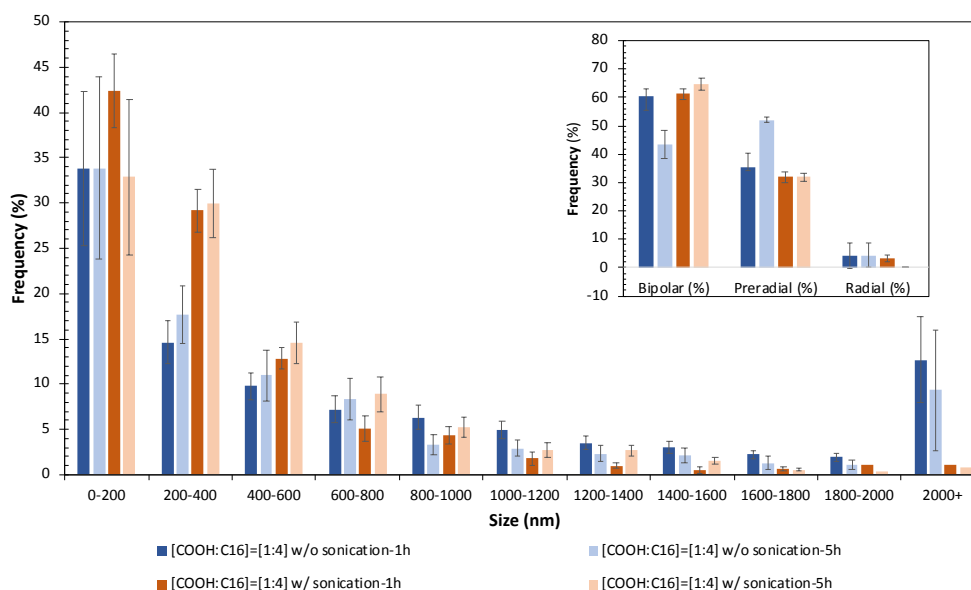
Figure 4.26 The size distribution from SEM images of the mixed monolayer coated gold nanoparticles on droplet surface with respect to time in the case of sonication and no sonication. Inset graph shows the distribution of configuration obtained under POM.

Another hypothesis was that ion concentration in the medium might affect the electrostatic interaction between particles and also LC-particle interaction. Therefore, the adsorption of AuNPs and their assemblies on the surface might be affected from ion concentration. In order to control the effect of charge, we added the salt, which was sodium chloride, to the medium to increase ion concentration. When the size distribution of the AuNPs adsorbed on the LC droplet was analyzed by using SEM, there was no significant difference in the size distribution with the salt addition (Figure 4.27). However, for the small sizes, which was in the range between 0 to 200 nm, there was an increase in frequency with time in the case of 50 mM salt concentration. This indicated the additional adsorption of AuNPs caused by salt addition.
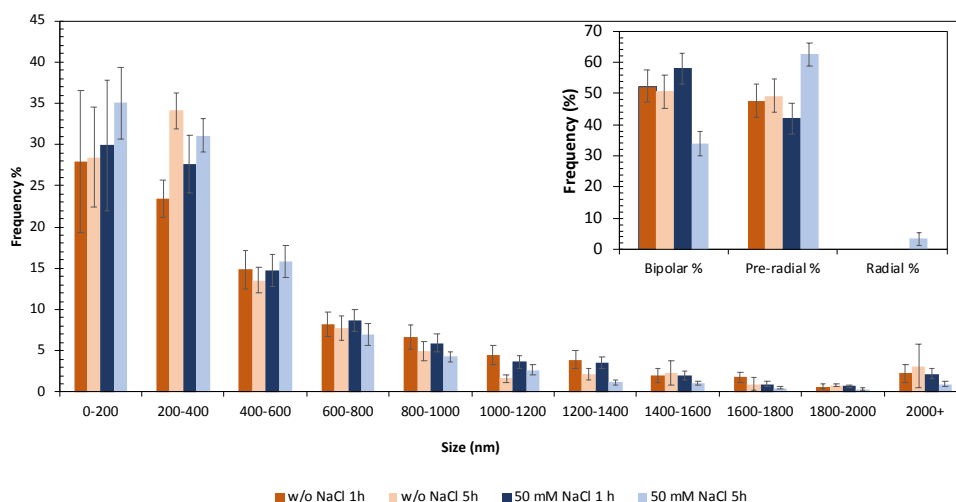
Figure 4.27 The size distribution from SEM images of the mixed monolayer coated gold nanoparticles on droplet surface with respect to time in the case of 0 and 50mM salt concentration. Inset graph shows the distribution of configuration obtained under POM.

When the results of these experiments which were performed to clarify the hypotheses were considered, we concluded that the dominant mechanisms that affect the LC droplet configuration with time were additional adsorption of the gold nanoparticles and the movement of the nanoparticle on the surface of LC droplet.

4.2 Development a Method to Define LC Configuration in Controlled, Three Dimensional, Confined Systems in Different Geometries

In this study, we developed a method to prepare a platform to confine LC in a specific, three dimensional geometry whose surface properties and thus the surface anchoring of LC was controlled. Firstly, we prepared microwells in different sizes and shapes by using a water soluble polymer (PVA) and developed the method for characterization and determination of LC configuration. Then, in order to be able to perform the analysis on LC-water interface we prepared water insoluble microwells by using a commercial epoxy and used the technique developed with PVA

microwells previously to determine the configuration of LC within the water insoluble microwells.

4.2.1 Determination of LC Configuration at LC-Air Interface by Confining in Controllable Geometry

4.2.1.1 Preparation of Microwells as a Confinement for LC

We designed a photomask containing patterns of different shapes and then a silicon wafer was processed by photolithography using this mask. After that these patterns were transferred to a PDMS mold by producing a replica from wafer. Therefore, we obtained PDMS mold with protrusions in the shapes of patterns that we designed (Figure 4.28). After this point, to prepare a confinement providing an opportunity to control over the anchoring when LC made contact with the surface, a material with a known surface anchoring should be used. Therefore, polyvinyl alcohol (PVA), which is water-soluble material providing planar anchoring to LC, was selected as the material of confinement. 5% wt of aqueous PVA solution was poured on to PDMS mold and after the evaporation of water, PVA microwells with the shape of square, rectangle, triangle, circle and star. SEM micrographs of the PVA microwells with the shape of triangle was represented in Figure 4.29 as an example. The reason of confining of LC in these specific shapes of microwells were to be able to analyze the LC configurations in different geometries which possess different physical properties such as sharpness, angle and symmetry that influence the elastic energy.
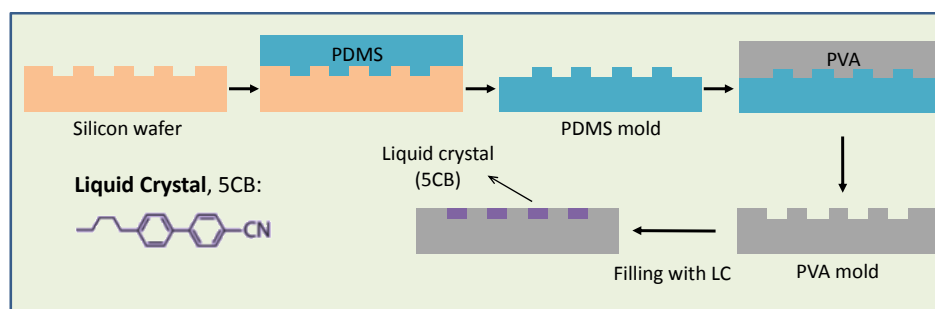
Figure 4.28 Preparation method of polyvinyl alcohol microwells made by soft-lithography
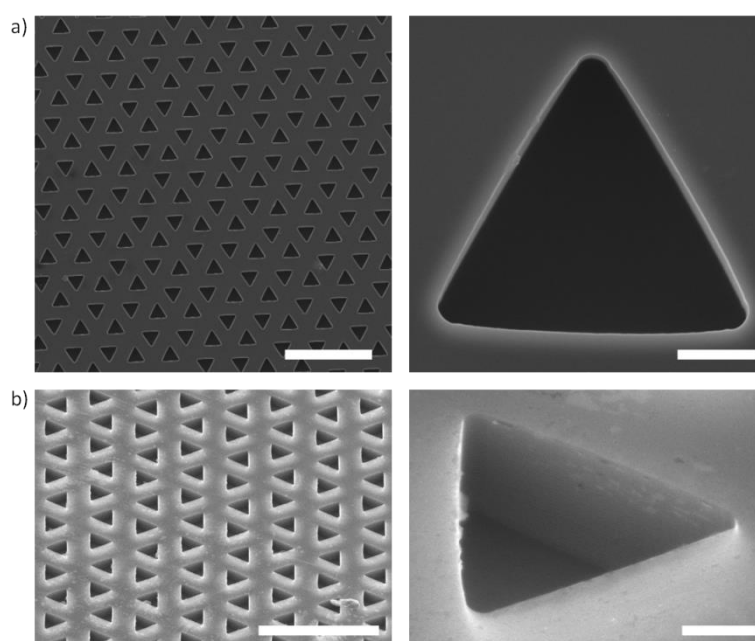
Figure 4.29 Scanning electron micrographs of empty PVA molds (a) top view (b) side view. Scale bars: a) 100 μm, 5 μm b) 100 μm, 5 μm

4.2.1.2   Configurations of Liquid Crystals Maintained in PVA Microwell

After the preparation of the microwells, they were filled with 5CB successfully and analyzed under polarized oprical microscope. In Figure 4.30, the micrographs of microwells with the shape of triangle, square, rectangle and star while they were empty and filled with 5CB in the case of both brightfield and polarized light were

63

represented. As it can be seen in micrographs, microwells were prepared with various shapes and 5CB was confined in these microwells successfully.

The anchoring conditions at the top and the other sides of the microwells filled with the nematic LC mixtures were different such that at the top LC was opened to air and had hometropic anchoring while at the interface with PVA, LC maintained planar anchoring. Although the same hybrid anchoring conditions were maintained within the microwells, the overall LC configurations may differ depending on the shapes and sizes constrained by the microwell geometry. Thus, we initially sought to determine the configurations of LCs as a function of size and shape of the microwells.
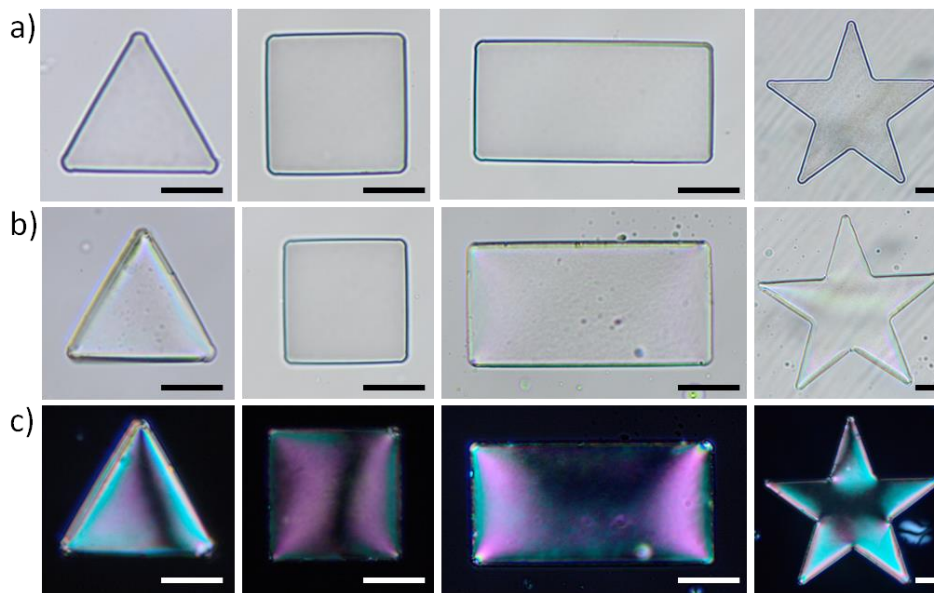
Figure 4.30 Polarized optical microscope images of a) empty microwells, b) filled with 20% wt of RM257 and 80% wt of 5CB in bright field and c) filled with 20% wt of RM257 and 80% wt of 5CB under polarized light. Scale bars: 20 μm

In order to characterize the configuration of LC confined in microwells with different shapes, the images of microwells were collected under polarized optical microscope while the stage was rotated to change the relative positions of the sample and polarizers. Then, by following the locations of dark brushes we determined the LC configuration as shown in Figure 4.31. In the case of triangle microwells, point

defects were located at each corners such that at two of them there were positively charged defects while one negative charged defect positioned at the third corner (Figure 4.31a). The point defects were positioned at the corners due to the lower elastic energy cost of maintaining defects at the corner when compared to the other locations within the microwell. When we confined 5CB in square shaped microwells, two different configurations were observed as shown in Figure 4.31b. It was found that in both configurations, two positive and two negatively charged defects were positioned at the corners of the square shaped microwells. The optical appearance of the microwells having these configurations were different resulted from whether the defects with the same charge were located on opposite or adjacent corners. As shown in Figure 4.31b, positioning of the defects with the same charge on the adjacent corners (top) or the opposite corners (bottom) created two different configurations in square shaped microwells. When we analyzed the distribution of these two configurations, the configuration inwhich the defects with the same charge were located on the opposite corners were more frequent such that their frequencies were nearly 60% and 40% of the total configurations, respectively. The distribution of defects may be attributed to their tendency to occupy positions where the total energy is minimized, primarily by reducing the elastic energy associated with strain in LC ordering. When the defects with same charge were positioned at the opposite corners, the distance between defects with the same charge was maximized and thus lower energy state was obtained comparing with the case of positioining at adjacent corners. Therefore, this explained why such configurations were predominantly observed in the microwells. In the case of rectangular microwells, LC maintained three different configurations (Figure 4.32a). In order to analyze the effect of size on these configurations, we repeated the experiments with the microwells with different sizes and the results were represented in Figure 4.32b and c. In the case of square microwells we could not observe any relationship between the size of the microwells and LC configuration but in the case of rectangular microwells the effect of size was more significant. For the large microwells of sizes 100×50 μm, the configuration where the two defects were located at the opposite corners (configuration-O) were

53.5 ± 8.6% of the total microwells. Besides, the configuration where the same charged defects were located at the adjacent corners corresponding to the ends of the long sides (configuration-L) consisted of 24.0 ± 2.8%, the configuration where the same charged defects were located at the adjacent corner corresponding to the ends of the short sides (configuration-S) consisted of 22.5 ± 9.4% of the total microwells. For smaller sized microwells (20 × 10 μm), we observed the configuration-O to be 41.8±4.7% of the total microwells and configuration L to consist the rest of the microwells, with no observation of the configuration-S (Figure 4.32b). This reduction of the frequency of the microwells with configuration-S for smaller sized microwells were due to the larger strain in the LC ordering caused by the microwells with configuration-S. As the size was decreased, the elastic energy penalty associated with the strain caused by the configuration-S became significant. Therefore, the configuration with the lower strain (configuration-L) became more frequent for rectangular shaped microwells.
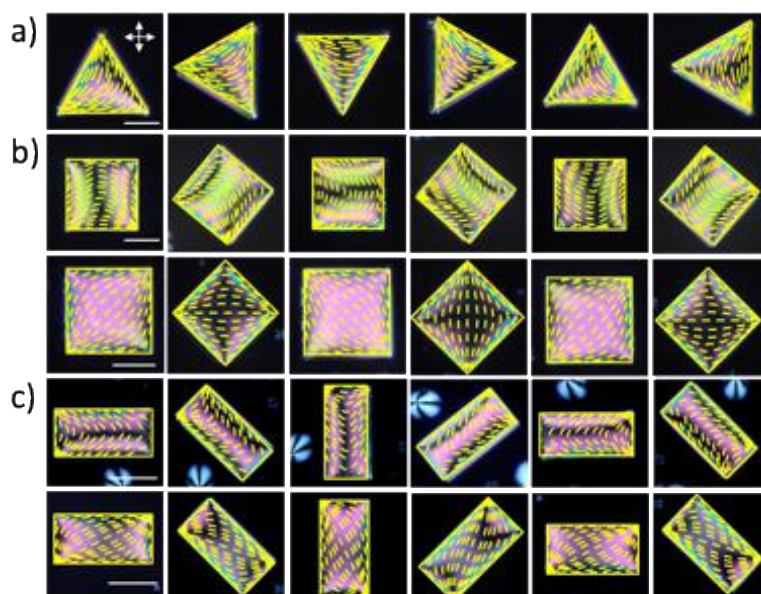
Figure 4.31 Polarized optical microscope images of the microwells filled with LC (5CB) which were taken by rotating 45°. a) Triangular b) Square c) Rectangular shaped PVA microwells filled with 5CB. Crossed white arrows show the directions of the polarizers. Yellow dashed lines show the LC configuration obtained optically. Scale bars: 25 μm

	Cross %	Parallel %	
50 μm	59.0 ± 8.7	41.0 ± 8.7	
20 μm	63.0 ± 1.1	37.0 ± 1.1	
10 μm	61.6 ± 3.8	38.4 ± 3.8	
	Configuration O %	Configuration L %	Configuration S %
100 x 50 μm	53.5 ± 8.6	24.0 ± 2.8	22.5 ± 9.4
50 x 25 μm	49.5 ± 2.1	43.1 ± 3.3	7.4 ± 1.6
20 x 10 μm	41.8 ± 4.7	58.2 ± 4.7	0
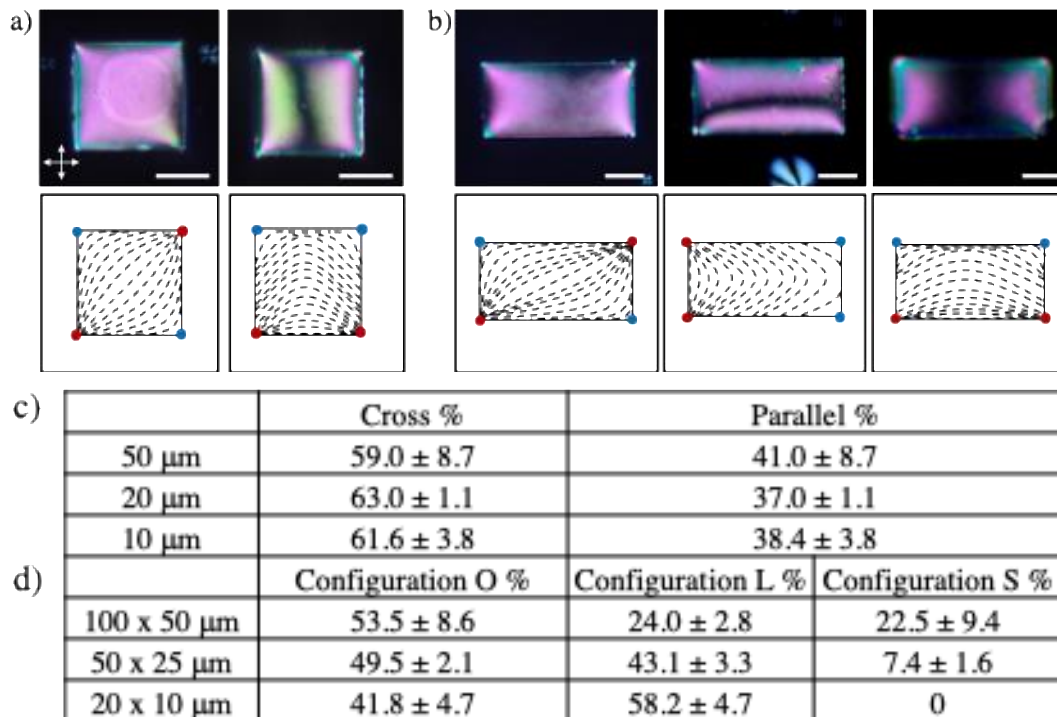
Figure 4.32 Polarized optical micrographs of the polymerized LC mixtures filled in (a) square wells with same charged defects at the opposite (left) and adjacent (right) corners and (b) rectangular shaped microwells with same charged defects located at the opposite-O (left), corners connected with short-S (center) and long-L (right) sides. Dashed lines in the sketches illustrated in the bottom row represent the LC configurations determined from optical micrographs. Red dots in the configuration sketches indicates the defects with positive charges and blue dots indicates the defects with negative charges. White cross arrows indicate the direction of analyzer and polarizer. Scale bars: 25 μm, Percentages of the frequencies of c) square shaped microwells having configuration in which the same charged defects located at cross corners and adjacent (parallel), d) rectangular shaped microwells having configuration-O, L and S with different sizes.

In addition to the shapes of triangle, square and rectangle we filled PVA microwells in circular shapes with 5CB to analyze how the absence of angular geometry influences strain, thus 5CB configuration and defect formation. When circular

shaped microwells were filled with 5CB, two point defects occurred like bipolar configuration of LC droplet configuration as shown in Figure 4.33a. However, these point defects were not always located at the poles such that the angle between them varied. Some examples of the microwells filled with 5CB having configurations with varying angle between the point defects were represented in Figure 4.33b.
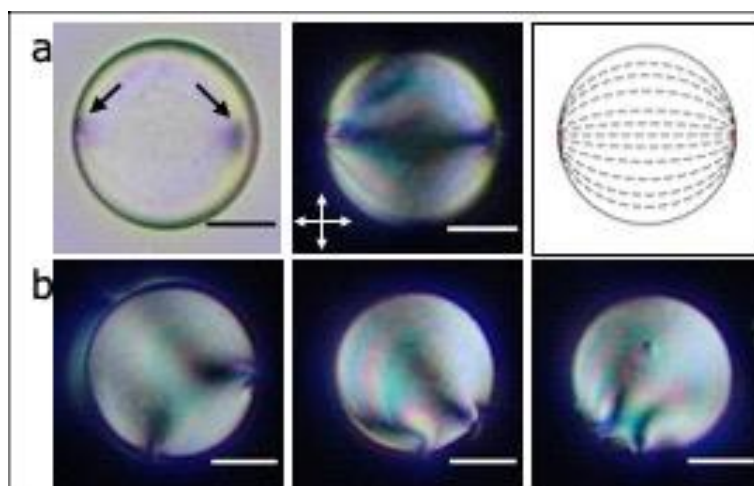
Figure 4.33 (a) Brightfield and polarized light photomicrographs of 50 μm sized LC-monomer mixture filled polymerized microwells. Crossed white lines (in a) represent the direction of analyzer and polarizer. The schematic representation of the LC ordering profile within the microwells which have two point defects near the poles is shown in the right panel where the red points represent the defect points. (b) Polarized light (PL) photomicrographs of 50 μm sized polymerized LC-monomer mixture within microwells with different defect locations. Scale bars: 20 μm.

When we measured the angle of separation of the defects in reference to the center of the microwell, it was observed that the angle ranged between 30º to 180º, averaging at 133.4 ± 4.9º, from 520 microwells. We reasoned that this variation in the defect positioning may arise from the imperfections in the surfaces of the PVA microwells where LC defects "pin". Such roughness that may lead to such pinning is apparent in the SEM images of the PVA microwells (Figure 4.29). When the microwells of 7 μm-in-diameter were filled with 5CB, we measured the angle of separation to be in between 120º to 180º, averaging at 165.1 ± 1.0º (n= 137

microwells). This separation was significantly larger than that we observed for LCs maintained in 50 μm-in-diameter microwells. In order to analyze the effect of the size of microparticles on determining of the location of defect points, the same procedure was applied for microwell sizes of 100, 50, 25 and 7 μm. For the analysis, the angle of separation of the two defect points formed within the microwells were measured and the distributions of the angles were plotted as shown in Figure 4.34. For smaller microwells, the average angle observed between defects were larger. For instance, the average separation angle of defects in 100 μm-sized microwells was 124.3° while this value was 165.1° for 7 μm-sized microwells. This can be explained by the fact that, for smaller sized microwells, the elastic free energy density which plays a crucial role on topological defect formation in LC medium was larger, thus, dominating the configuration of the LCs confined into the microwells, eventually resulting in distant positioning of the defects to reduce the effects of the strain caused by pinning of the defects at the surfaces. Thus, as the size of the microwells was decreased, narrow distribution of angles at a magnitude close to 180° in between defect points was obtained.
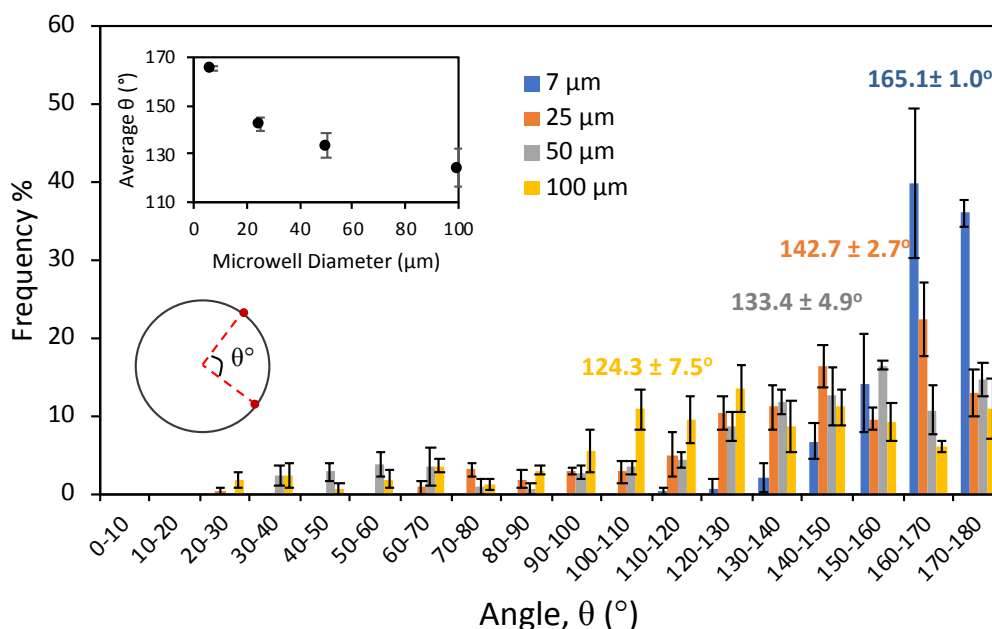
Figure 4.34 Distribution of angle between point defects and the center of the microwell as a function of the diameter of the microwell. Average of angles in

between defect points were indicated. Inset graph shows the average separation angle with respect to the microwell size. (N=3, n $\cong$ 200 for large particles, 50 for small particles).

As a control experiment, the microwells were filled with the mixture of 20% wt of 5CB and 80% wt of the monomer (RM257). The reason of filling with the mixture was to be able to make the analysis by using polarized optical microscope and then compare the results from these analyses with the implications obtained from the morphology of the polymer. After the polymerization of the mixture confined in microwells, we obtained the microparticles with the shape of particles but the shape of the particles varied with respect to the internal structures. The configuration of LC was represented with schematics in Figure 4.35a and the SEM micrographs of the microparticle were shown in Figure 4.35b. When the SEM micrographs were analyzed, we observed that the alignment of the surface roughness patterns was in the same direction with pre-determined LC configuration. The homeotropic surface formed on the LC-air interface was seen as porous structure aligned through outward direction (Figure 4.35c). Also, the negatively (Figure 4.35d) and positively (Figure 4.35e) charged defects localized on the corner of the particles and the symmetrical structures around these defects could be easily seen from SEM micrographs.
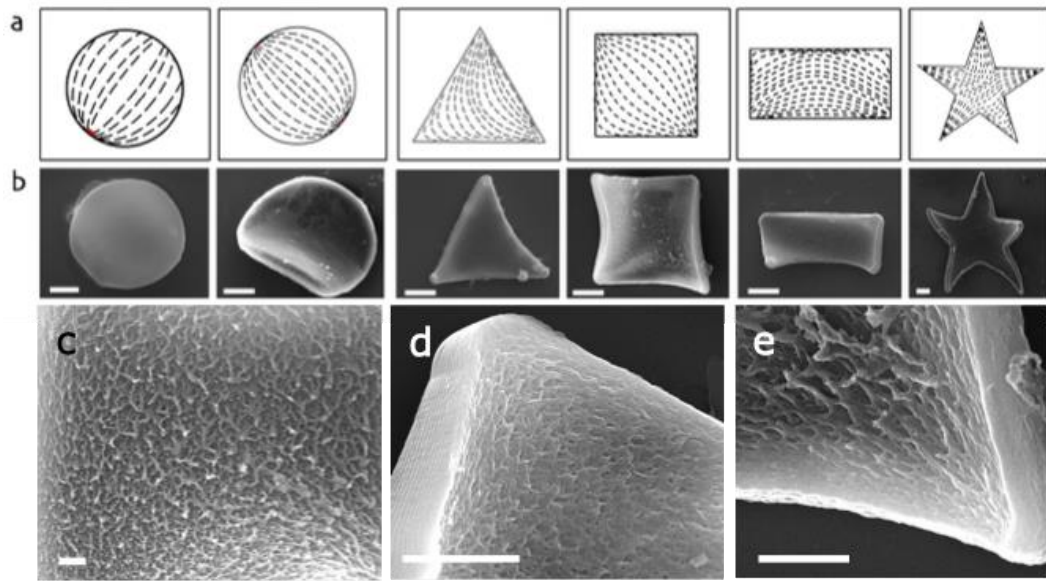
Figure 4.35 (a) Schematic representation of the configurations of the liquid crystalline, (b)scanning electron micrographs of LC extracted microparticles that have different shapes which are circle, triangle, square, rectangle, star. Scanning electron micrographs of the surfaces of the particles synthesized from mixtures of 20% wt RM257 and 80% wt 5CB. The image of (c) the surface corresponding to homeotropic surface anchoring, (d) the corner where negative charged defect is located, (e) the corner where positive charged defect is located Scale bars: for row b; 1 µm for first column, the others: 10 µm, for c,d,e: 5 µm

The method that developed in this part of the study provided determination of the configuration of LC confined in microwells with controlled geometry. Therefore, development of such a method has paved the way for the detection of LC configuration under different anchoring conditions and the preparation of microparticles with predetermined internal structures.

4.2.2   Stable LC Micro-Confinements as a Platform for
**   Analysis of Aqueous-Soluble Species**

After the development of a method for the determination of LC configuration in PVA microwells, in order to be able to make the analysis on LC configuration at LC-aqueous interface, water insoluble microwells were prepared.

4.2.2.1   Preparation of Water Insoluble Microwells for Analysis of
**   Aqueous-Soluble Species**

We fabricated these water insoluble microwells with sizes in the range of 10-100 μm with shapes of square, circle, rectangle or triangle (Figure 4.36a,b). When we compared the size in the template and final size obtained in epoxy microwell, we observed that the dimensions of the pattern initially processed onto the silicon wafer were almost exactly same with final dimensions of the microwells (Figure 4.36c). The ability to control of the dimensions of microwells might enable to make analysis of the LC configurations in geometries which possess controllable physical properties that influence the elastic strain of LC.
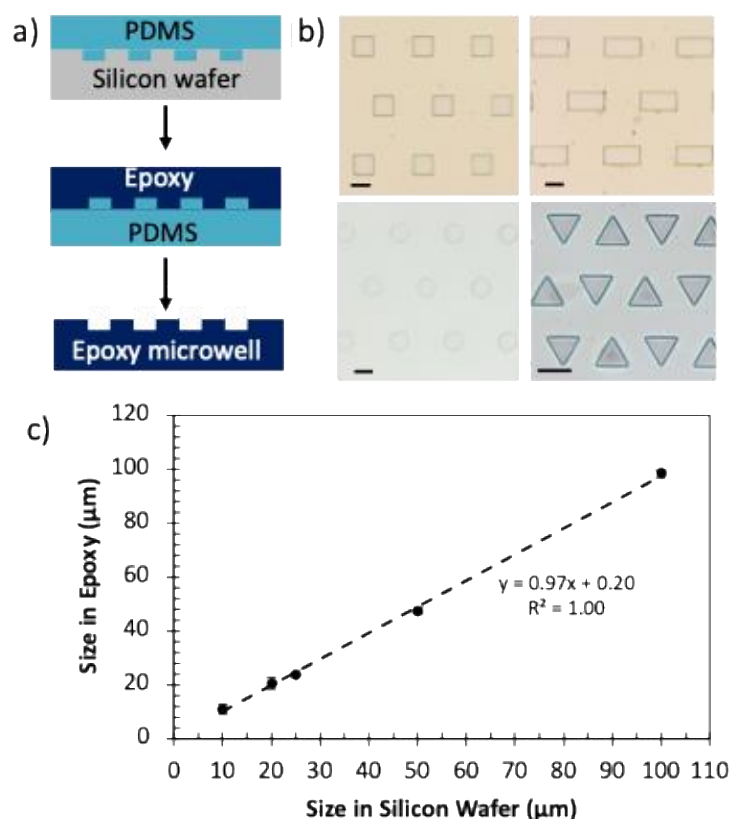
Figure 4.36 a) Schematic of the preparation method of epoxy microwell, b) the optical microscope image of rectangular shaped epoxy microwell. c) comparison of final size of the features in epoxy microwells with the template size. Scale bar: 50 μm

During the filling of the microwells, firstly we observed de-wetting of bare epoxy microwells (Figure 4.37a,b) and in order to solve this problem and improve the wetting of 5CB, the surface was coated with DMOAP[100]. After coating with DMOAP, the contact angle of water on the surface of epoxy film was remained nearly same when the medium was the air (Appendix A1). However, we measured the contact angle of 5CB on the surface of epoxy film after coating of DMOAP and it decreased from 57.4°±3.7 to 37.8°±9.8. When we repeated the same experiment in the case of aqueous medium, the contact angle of 5CB on the surface of DMOAP epoxy film was 86.6°±6.0, whereas it was measured as 98.7°±5.3 on the bare epoxy film. Therefore, coating the surface with DMOAP improved the wetting of 5CB on

epoxy film by enhancing the oleophilicity. After solving the dewetting problem, we tried to confine 5CB by using the microwells with the shapes of square, rectangle, triangle and circle and the dimensions in a range between 100 μm to 10μm and no problems were encountered during both the preparation of the pattern and filling with 5CB (Figure 4.37c-h). The ease of modifying shapes and sizes, along with the method's adaptability to each pattern, suggests that a wide variety of geometries can be created with different designs.
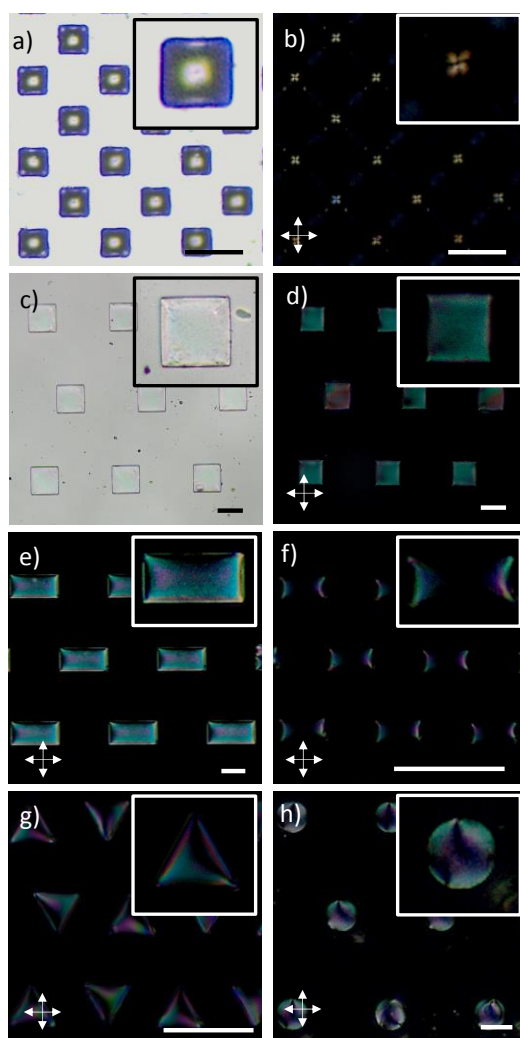
Figure 4.37 Polarized optical microscope image of bare epoxy microwells with the shape of square filled with 5CB a) brightfield, b) polarized light, square shaped epoxy microwell filled with 5CB in the case of coating with DMOAP c) brightfield,

74

d) polarized light, rectangular shaped microwells filled with 5CB with the size of e) 50x100μm f) 10x20μm. Polarized optical microscope images of g) triangular h) circular shaped microwells filled with 5CB. Insets show the images in higher magnification. Arrows indicate the direction of the polarization of the polarizer and analyzer. Scale bars: 50 μm

4.2.2.2   Analyses on LC Configuration and Defect Formation in LC Confined in Epoxy Microwells

Epoxy microwells, those filled with 5CB were analyzed under polarized optical microscope and their micrographs were captured in the case of 5CB-air and 5CB-water interfaces as shown in Figure 4.38. In the case of 5CB-air interface, the bright color was obtained under polarized optical microscope (Figure 4.38a) and this brightness under cross polarizers was caused by 5CB orientation within the microwells. The orientation of 5CB was created by the total effect of anchoring on epoxy microwell, interfacial anchoring at LC-air interface, and thus the deformation of 5CB to maintain such boundary conditions. Since the interfacial anchoring at LC-air interface is homeotropic, the alignment of 5CB near the top surface was expected to become perpendicular to the interface. On the other hand, in the regions close to epoxy surface, the 5CB orientation was deviated because of the surface anchoring on epoxy. When the 5CB molecules close to epoxy surfaces oriented in a direction, which was different from the directions of both analyzer and polarizers, a brightness was obtained in these microwells. Since the central regions of the microwells filled with 5CB whose top surface was opened to air did not appear dark, we reasoned that 5CB did not maintain homeotropic anchoring on the surface of epoxy even if it was coated with DMOAP (Figure 4.38a). In order to measure the angle by which the LC deviated from being perpendicular to the surface, conoscopic images of the sandwich cells, which were prepared with epoxy film and DMOAP coated glass slide, were collected. Tilt angle was calculated by using these images and we found that it deviated from homeotropic orientation by 23.6°± 6.2 (Appendix B.1). When LC-

water interface was created by immersing the 5CB filled microwells in water, the region near to center of the microwells appeared dark under crossed polarizers as shown in Figure 4.38b. However, these dark brushes repositioned based on the direction of the polarizers as shown in right column of Figure 4.38b because of the orientation of the 5CB molecules confined in microwells. In order to evaluate the stability of the microwells in aqueous medium, the microwells filled with 5CB were stayed in aqueous medium for one day and reimaged with crossed polarized microscope as shown in Figure 4.38c. When images taken at 1st hour and 24th hour after immersion in water were compared, there was no significant change in their optical appearance or issues hindering long-term analysis in the aqueous environment. When we analyzed the distribution of LC configuration at 1st and 24th hour to examine whether there have been any changes in configuration over time, the frequency of three different LC configurations remained unchanged from the first hour to the 24th hour in the absence of an external stimulus as shown in Figure 4.38d.
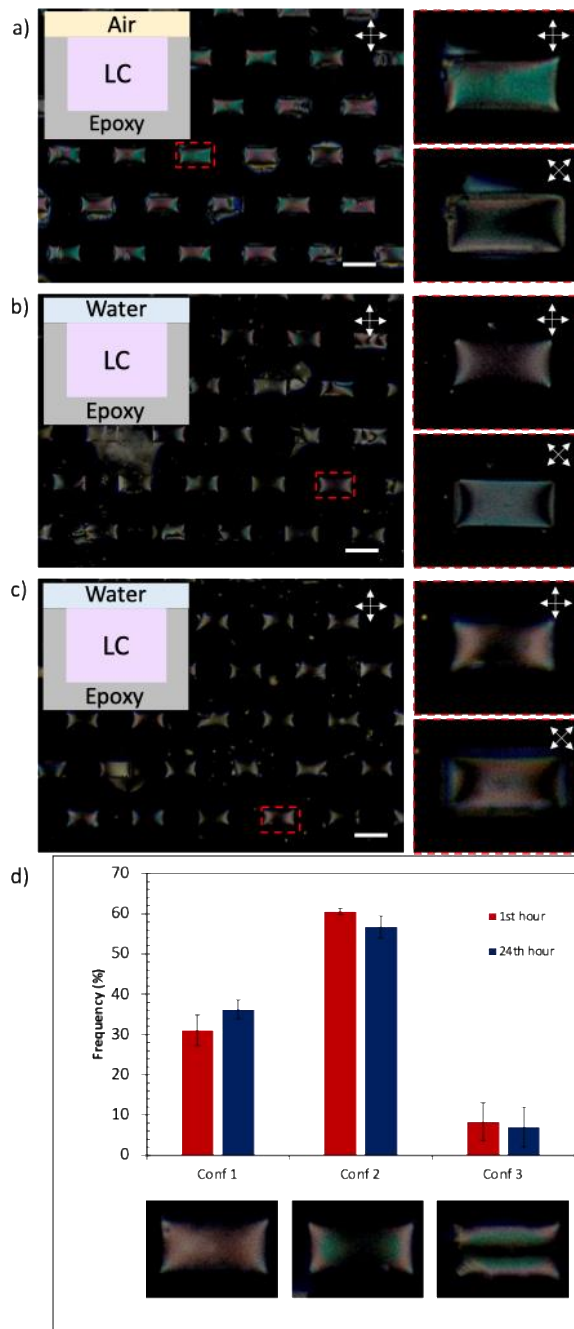
Figure 4.38 POM images of LC filled microwells in the case of a) LC-air, b) LC-water interface after 1 hour and c) LC-water interface after 24 hours d) distribution of microwells configuration with three configurations with respect to time (1h vs 24h). Insets are schematic representation of microwells showing the system configurations. Arrows indicate the direction of the polarization of the polarizer and

analyzer. Red rectangles show the microwells which are represented in higher magnification. Scale bars: 50 µm

LC orientation is affected by surface anchoring which depends on the material used for the confinement. For instance, polyvinyl alcohol (PVA) provides degenerate planar anchoring while polydimethylsiloxane (PDMS) offers homeotropic anchoring to LC[17,101,102]. To compare the optical appearances of microwells made from PVA and PDMS, providing specific surface anchoring to LC, we analyzed LC filled microwells under POM (Figure 4.39a, b). The optical appearance of PVA microwells filled with LC was bright and colors ranging between pink and blue were observed arising from the birefringence of LC as shown in Figure 4.39a. On the other hand, in the case of PDMS microwell, the optical appearance was totally different such that the center of the microwells remained dark while the polarizers were rotated with 45° as shown in the inset in Figure 4.39b which means the orientation of LC molecules was perpendicular to the surface. Then, in order to provide planar interfacial anchoring, we immersed PDMS microwells in aqueous medium. When we analyzed under polarized optical microscope, we observed that a point defect formed in the central region of the microwells as shown in Figure 4.39c with red arrows and also black dot in figure shown in Appendix C.1. The reason of this defect formation at the center was the energy penalty that occurred because of the boundary conditions such that strong homeotropic anchoring at LC-air interface to planar anchoring at the LC-water interface[29,30].

In addition to these experiments, further control experiments were performed to enhance our comprehension of the LC configuration within the microwells. In these control experiments, we filled the microwells with a mixture of 5CB and reactive mesogen (RM257) to confine and analyze the configuration within microwells. Before the polymerization, we analyzed under polarized optical microscope and observed that in the case of the interface with air, optical appearance of the microwells filled with the monomer solutions was similar with the PDMS microwells filled with LC as shown in Figure 4.39d which means that the center of microwells was dark indicating the perpendicular orientation from top to the bottom

surface. This showed that the surface anchoring of mixture of 5CB and RM257 was homeotropic on epoxy surface, unlike the surface anchoring of 5CB on epoxy. In order to verify that the surface anchoring of mixture on epoxy surface was homeotropic, we prepared sandwich cells with epoxy film and DMOAP coated glass slides and filled these cells with the mixture of monomer and 5CB. When we analyzed these cells under polarized optical microscope, we observed that the anchoring was homeotropic on epoxy surfaces since the appearance of the cell remained dark while the direction of polarizers was changed as shown in Appendix D.1. In addition, it has been known from literature that the addition of reactive mesogen to the nonreactive mesogen caused a transition to tilted anchoring at LC-water interface which was caused by the elastic energy and also the surface anchoring of the LC regarding the addition of monomer[35,71]. When the epoxy microwells filled with LC-monomer mixture were immersed in aqueous medium, the formation of "point" defect was observed again, similar to the formation occurred when PDMS microwells filled with LC were immersed into water as shown in Figure 4.39e with red arrow. After these analyses, in order to analyze the morphology of the polymer by using SEM to get more information about the configuration of LC-monomer mixture, we polymerized RM257 and 5CB mixture confined in epoxy microwell while it was immersed water. After the polymerization, the non-reactive mesogen (5CB) was extracted by dissolving with ethanol and polymer was dried with air. When the LC orientation was analyzed by considering the morphology of the polymer, we observed that the alignment of the pores was perpendicular to the edges of the microwell and there was a structure indicating the presence of a defect close to the center, which was pointed with re circle in Figure 4.39f, in a manner that provides additional support to the deductions made from the images obtained through optical microscopy. Thus, we performed all these experiments designed with the aim of adjusting the boundary conditions. We observed that altering the surface anchoring of 5CB on the material of confinement or interfacial anchoring affected the optical appearance of microwells filled with 5CB. These effects were formation of the dark brushes and also topological defects which were directly related with the

orientation of 5CB molecules in the microwells. We focused on the determination of internal structure in microwells because our main purpose was to use these microwells as a platform for the sensor applications. Therefore, in order to use the change in the orientation as a response against adsorption of a molecules or colloids, the configuration of the LC molecules should have been clarified.
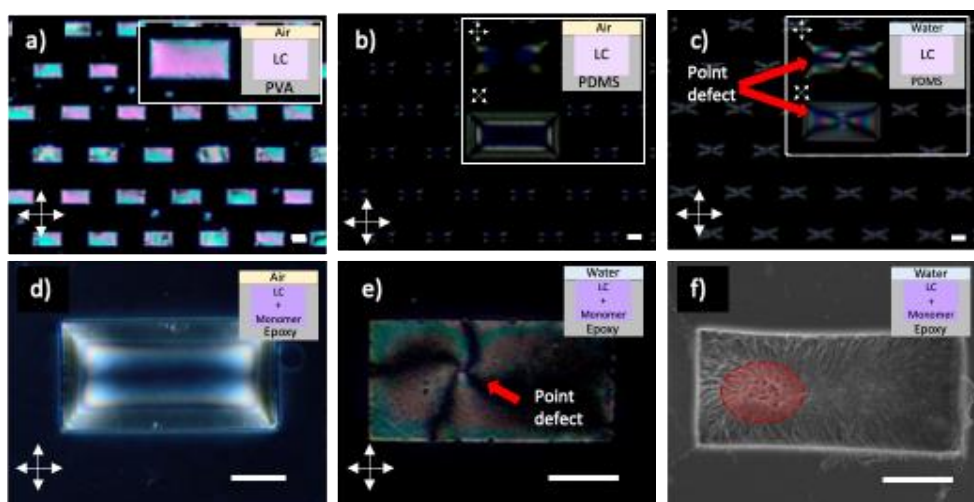
Figure 4.39 POM images of 5CB filled microwells made from (a) PVA microwells and (b) PDMS in the case of LC-air interface, (c) PDMS in the case of LC-water interface and POM images of epoxy microwells filled with 20% wt monomer solution in the case of interface with (d) air and (e) water. Polymerized form of the epoxy microwell filled with 20% wt monomer solution in water is shown in (f). Insets are schematic representation of and high magnification images of microwells showing the system configurations in the case of different interfaces. White arrows indicate the direction of the polarization of the polarizer and analyzer. Red arrows indicate the position of point defect formed in confined 5CB and red circle marks the region indicating position of a point defect occurred in the mixture of RM257 and 5CB. Scale bars: 25 μm

Since LC-filled epoxy microwells were stable under aqueous medium, it was possible to analyze the 5CB orientation as a function of concentration of the adsorbed molecules. In this study, we used sodium dodecyl sulfate (SDS) as a model molecule which is one of the well-known surfactants that causes changes in the orientation of

LC molecules. When SDS is added to the aqueous medium, the anchoring deviates from planar to tilted, depending on the concentration, and reaches homeotropic anchoring at a specific concentration (around 1mM)[27]. When SDS molecules were added to the aqueous medium systematically, such that the concentration of SDS was increased step by step, we observed that the color of the LC confined in microwells varied in such a way that a transition from soft tones of pastel colors to more bright, intense tones of vivid colors with respect to the concentration of SDS (Figure 4.40). The reason of this transition in the colors was thought as the change in LC orientation confined in microwells starting from the transition of interfacial anchoring from planar to tilted anchoring caused by the adsorption of surfactant molecules. When LC configuration was examined in more detail, remarkably surprising observations were obtained. These observations typically involved the formation of line defects extending between opposite edges, following the addition of SDS to the medium as shown in Figure 4.40. The percentages of microwells containing disclination lines in the case of LC-air, LC-water, LC-0.6 mM SDS solution and LC-1.0 mM SDS solution were 5.52 ± 2.1, 2.77 ± 4.0, 33.8± 11.9 and 53.1± 6.8 respectively. The frequency of microwells with a configuration containing disclination line was low when the interfacial anchoring was homeotropic and it was not increased by converting the interfacial anchoring to planar anchoring by suddenly immersing into water. However, when the interfacial anchoring was converted to tilted anchoring step by step, the frequency of the microwells with a configuration containing disclination lines was increased, significantly. Therefore, it was reasoned that the formation of the disclination lines was path-dependent. In order to analyze the dependency of disclination line formation on the concentration of SDS molecules and also the reversibility of orientation change of LC, we diluted the concentration of medium and observed under polarized optical microscope. When the images, which were taken at the same concentration while addition and dilution steps, were compared, we observed that almost identical images were obtained. The frequency of the microwells having disclination line was almost the same after the SDS concentration was diluted as shown in Appendix E.1. This means that changes in the

configuration (color change and defect formation) are reversible and directly related to SDS concentration. In this way, by adsorbing SDS molecules to the LC-water interface, we were able to observe how the LC configuration changed depending on the tilted anchoring created at the interface, and we also challenged the durability of LC confined within the epoxy microwell. When the similar experiments were repeated with the circular shaped epoxy microwells of 50 and 100 μm diameter, we obtained promising results for the controlling the sensitivity of these platforms by adjustment of the size and the geometry such that the color change and the defect formation started at lower concentration in microwells with smaller size (Appendix F.1). For example, in the case of 100 μm in diameter circular microwells, the frequency of the microwells with line defects at 0.2 and 0.4 mM SDS concentration was 25.0 ± 8.3 and 39.4 ± 4.2, respectively. However, in the case of 50 μm in diameter circular microwells, the frequency of the microwells with line defects at 0.2 and 0.4 mM SDS concentration was 56.3 ± 6.3 and 60.0 ± 7.5, respectively. Therefore, it indicated that the lower concentrations can be detected by using microwells having smaller size. The reason of this increase in the selectivity was increase in the strain within the geometry of the microwells by decrease in the size.
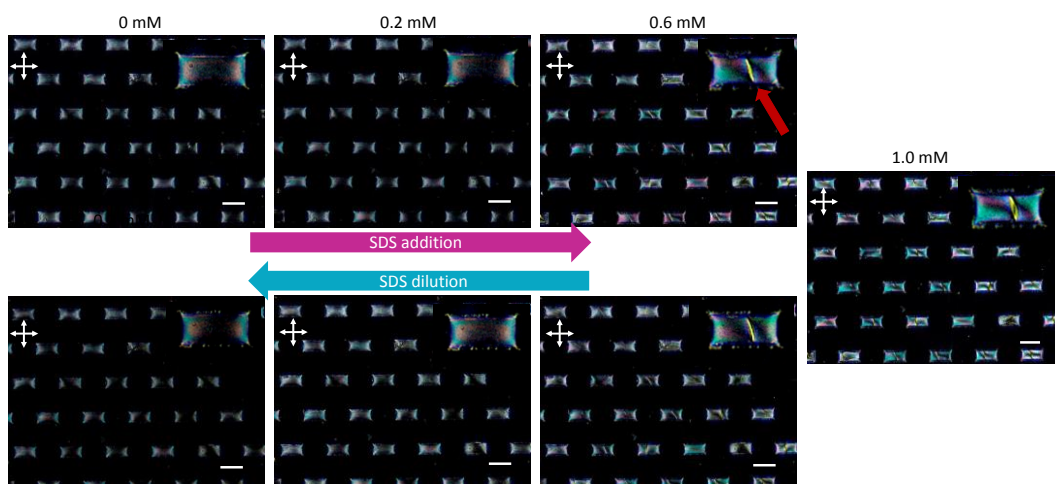
Figure 4.40 POM images of LC filled epoxy microwells immerged in aqueous medium having SDS concentration as 0, 0.2, 0.6, 1.0 mM in the case of SDS addition and dilution. Insets show the images in high magnification. Line defect was shown

by using red arrow. White arrows indicate the direction of the polarization of the polarizer and analyzer. Scale bars: 100 μm

In order to determine the LC configurations, dark brushes were analyzed by rotating the polarizer and analyzer, systematically. As a result, it was found that the LC configurations in the case of interfaces of LC-air, LC-pure water and LC- 0.6 mM SDS solution, might be as shown in Figure 4.41. As it can be seen from Figure 4.41, when these interfaces were created, the positions and types of defects were altered by changes in the interfacial anchoring. Type of the defect structures which are point or line defects and the positions of these defects in the microwells depended on the interfaces having planar, tilted, or homeotropic anchoring.

In the case of LC-air interface, it was found that the majority of the microwells maintained a configuration such that the point defects located at the corners instead of random positions as shown in Figure 4.41a. On the other hand, when the microwells were immersed in pure water, the surface anchoring deviated from homeotropic anchoring to planar anchoring at the interface and a point defect was formed because of the increase in the strain in LC. Since the shape of microwells and anchoring conditions were symmetrical, a single point defect might be formed at center of the microwells as shown in Figure 4.41b or multiple point defects might be located at the positions according to the conservation of charge law which claims that there should be equal number of the defects with opposite charges[103]. In the case of LC-0.6 mM SDS solution, the interfacial anchoring was changed from planar to the tilted. The transition to tilted anchoring caused a configuration change in such a way that the majority of the microwells had a disclination line located at the central region passing from the opposite edges as shown in Figure 4.41c. The reason of the formation of these disclination lines was considered as the equilibrium between the charge of the defects positioned at the corners and the middle of the edges. When the sign of charge of defect occurring at the middle of edge was the same with the charge of defects located at the corners, a repulsion occurred between them but the strain was high enough to prevent the annihilation. Therefore, a disclination line was occurred between the opposite edges as shown in Figure 4.41c. On the other hand,

when the charge of defect at the middle of edge had opposite sign of the charge of defects located at the corners, an equilibrium was achieved and point defects were located as shown in Figure 4.41d.

In order to perform the control experiments, microwells made from PDMS were used again to regulate the surface anchoring at the surface of microwell. In the case of PDMS microwells, the experiments with the interfaces of LC-air, LC-water and LC-SDS solution were repeated and the configurations were analyzed by using polarized optical microscope. With these experiments, we observed that when the strong anchoring condition was supplied to the system, the defects were located to the corner or just the center of the microwells, so it suggested that the configuration in which line defects occur was a metastable configuration, and the configuration where defects settle at the corners might be more stable and preferable configuration.

The formation of defects depends on the conservation of the charges and according to this rule the summation of the total charge should be vanish so the topological defects should be formed in such a way minimizing the total charge[21,22,63,104]. Therefore, it can be said that the formation of LC configurations might be explained by the conservation of charge because there might be more favorable configuration with respect to this law. As presented in Figure 4.41, when the charges of defects, which have been determined using optical methods, were summed, they were found to be zero. This demonstrated adherence to the conservation of charge law. In addition, in order to clarify the dependency of variety in LC configuration on the stability and to understand whether there were metastable states or not, LC filled rectangular shaped epoxy microwells were heated up to nematic-isotropic transition temperature and cooled down to room temperature to reset the LC orientation in microwells. The distribution of LC configuration before NI transition and after NI transition were analyzed for microwells with different sizes which were 10x20, 25x50 and 50x100 μm (Appendix G.1). We observed that with the NI transition the LC orientation reached a new configuration which was thought as more stable state. In this configuration, any point defects or line defects could not be seen at the edges and we reasoned that the point defects were located at the corners of the rectangle.

When the distribution of LC configuration was analyzed, we observed that the frequency of the microwells where the point defects located at the corners increased after NI transition.
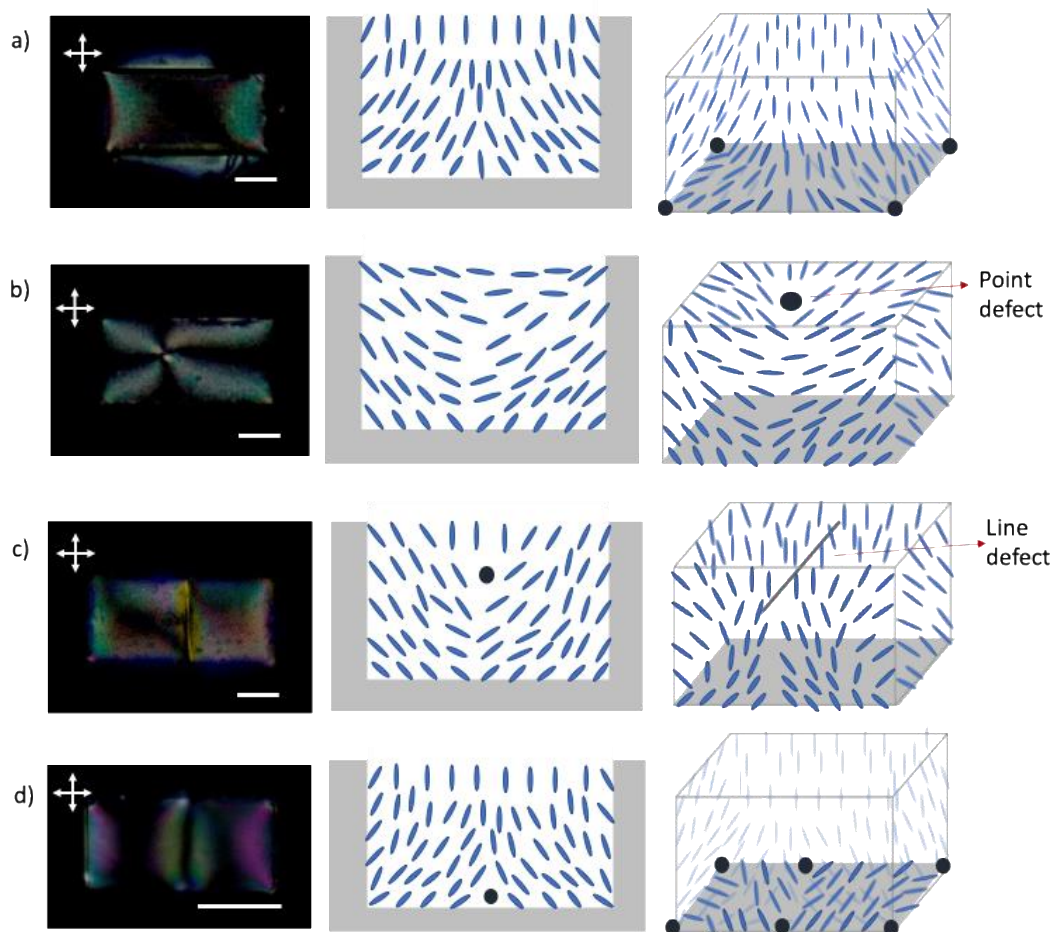
Figure 4.41 POM images of rectangular epoxy microwells filled with 5CB in the case of a) LC-air, b) LC- pure water, c,d) LC-SDS solution in the first column and schematic representation of orientation of LC confined in microwells in the second and third columns. Insets are schematic representation of microwells showing the system configurations in the case of different interfaces. Arrows indicate the direction of the polarization of the polarizer and analyzer. Scale bars: 25 μm

During the transition from isotropic phase to nematic phase, reorientation of LC molecules was analyzed under polarized optical microscope (Figure 4.42). While LC molecules reorient, the topological defects occurred and these defects moved to each

other and therefore the defect annihilation was occurred depending of the charge of the defects. The defect annihilations were categorized in 5 cases which are defect annihilation on long edge, on short edge, at corner-movement on short edge, at corner- movement on long edge, at corner-movement from bulk to corner. When the movement of the point defects were analyzed in detail, we observed that the velocity of the point defects differed depending on the distance between them as expected from the literature[105]. Therefore, the ratio of the velocity of point defects was calculated to analyze the behavior of the point defects during annihilation. We calculated that the ratio of the velocities of the point defects that annihilated was around 2 in both cases of the movement through long and short edges (Appendix H.1). The reason of the velocity difference between the point defects is that the charge of the defects, causing from the LC orientation around their vicinity, affects their speeds, so the defects with positive charge move faster than the negative ones[103,105,106]. As it can be seen from Figure 4.42, in the case of defects with opposite charges, if they were close enough not to create significant strain, they moved to each other and annihilation occurred. However, when the point defects occurred at the opposite edges, annihilation could not be occurred and the line defects were formed due to the impossibility of overcoming the resulting strain, a disclination line formed.
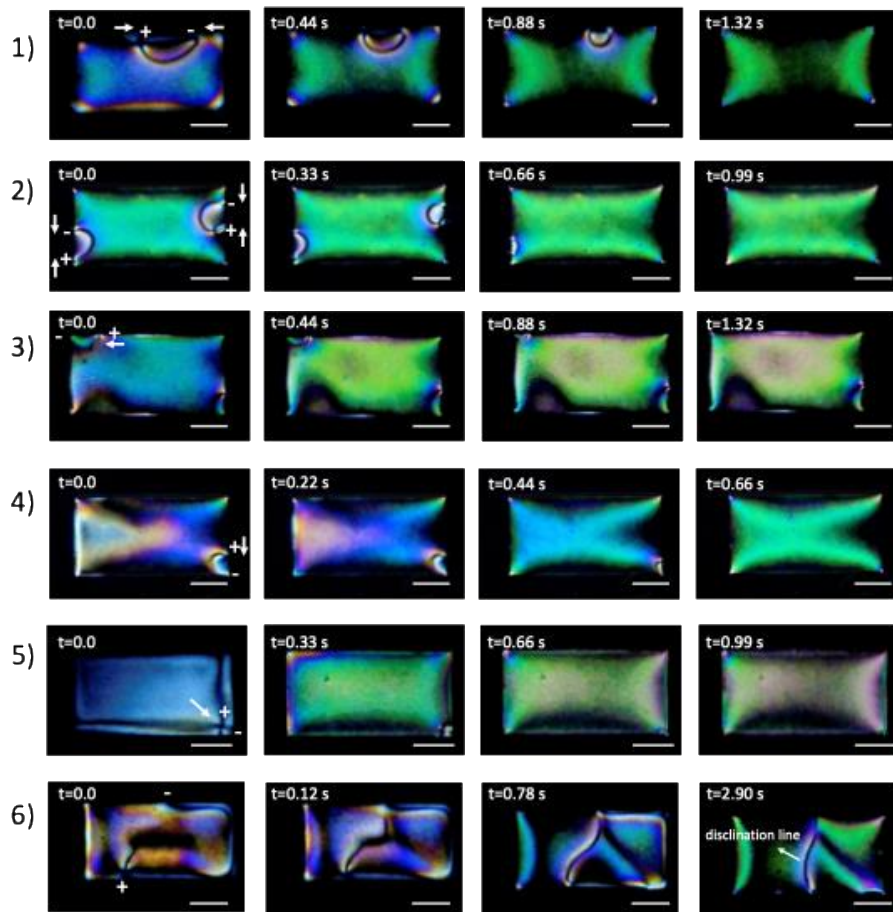
Figure 4.42 Schematic illustrations and polarized optical microscope images of the movement of the point defects in the case of rectangular shaped microwells. Scale bar: 25 μm.

4.2.2.3 Response Tests of LC Confined in Epoxy Microwells

LC responds to changes at the interfaces it interacts with by changing its orientation. This response can lead to new defect formation, changes in the defect type, as described so far, or changes in color due to alterations in the zenithal (tilt) angle without any change in the defect structure and all these responses can be easily detected under POM and this convenience opens the way for many sensor applications because it is so useful platform for collecting the response against the situations occurred at the interfaces. As it can be seen in Figure 4.43a, in the case of

LC-air, LC-water and LC-SDS solution, the colors of the LC-filled epoxy microwells were different because of the optical retardance. The value of the optical retardance can be approximated using a Michel-Levy chart[20]. Therefore, the color changes in the images obtained under POM can be converted into the numerical values by reading the retardance values from Michel Levy Chart. In order to convert the retardance values to tilt angle, we used the reduced form of Frank-Oseen expression by assuming the minimization of elastic free energy of LC slab geometry and calculated the tilt angle by relating with retardance[20,107,108] as shown in Figure 4.43b. There was a significant difference between the tilt angles such that the tilt angle at the LC-air interface was $20.7° \pm 0.9$ while at LC-water interface it was calculated as $70.1° \pm 4.1$. In order to create tilted anchoring SDS molecules were added to the aqueous medium with a concentration of 0.6 mM. The reason of selection of this concentration was that at this concentration interfacial anchoring was tilted as verified by the experiments on LC droplet configuration such that the majority of LC droplets had pre-radial configuration indicating tilted anchoring at 0.6 mM SDS concentration. We observed that the difference between the tilt angles decreased such that the tilt angle at LC- 0.6 mM SDS solution was calculated as $28.6° \pm 7.2$. These conclusions were supported statistically by applying the p-test as noted in Figure 4.43. When we considered the p-values to compare the tilt angle in the case of the interfaces of LC-air, LC-water and LC-SDS solution, it was evident that tilt angle values at these interfaces differed from each other ($p < 0.05$) and there was no evidence representing that the tilt angle was changed when the SDS solution was diluted and compared with its initial value ($p > 0.05$).
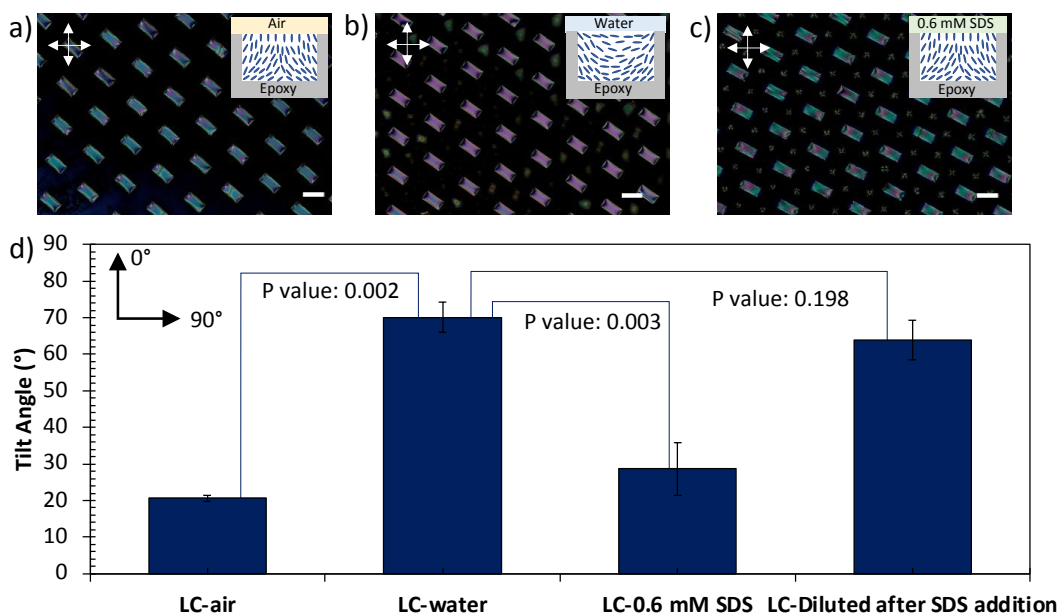
Figure 4.43 POM images of LC filled epoxy microwells and schematics of LC configuration in these microwells in the case of a) LC-Air, b) LC-Water, c) LC- 0.6 mM SDS solution and d) Graph which represents the tilt angle values in the case of different interfaces. Insets are schematic representation of microwells showing the LC orientation in the case of different interfaces. Scale bars: 50 μm

In addition to the adsorption of surfactant molecules, we analyzed the response of LC in the case of adsorption of nanoparticles. The reasons for preferring nanoparticles as a model and investigating the LC response dependent on the adsorption of nanoparticles were that they have high mobility and it is possible to adsorb and carry other compounds by using them. The surface properties and electrostatic interactions of silica nanoparticles with the size of nearly 100 nm were adjusted by surface functionalization methods. For this purpose, we prepared -COOH-terminated, COOH/DMOAP mixed monolayer coated and DMOAP coated silica nanoparticles. Therefore, we had ability to control the electrostatic interactions between nanoparticles and nanoparticle-LC by modifying the surface to mediate pH-dependent charge and also it was possible to manipulate the hydrophobicity of nanoparticle surface. It has been known from previous studies that functionalization methods affect the anchoring on the surface of the nanoparticles and also LC configuration when they are adsorbed on LC-water interface. In the case of

adsorption of -COOH-terminated silica nanoparticle does not cause a configuration change in LC droplet in aqueous medium while COOH/DMOAP mixed monolayer and DMOAP coated silica nanoparticles create a transition to planar to tilted/homeotropic anchoring[38]. As seen from Figure 4.44a, when the -COOH-terminated silica nanoparticles were adsorbed at LC-water interface, tilt angle was found as 70.0°± 4.9 but in the case of COOH/DMOAP mixed monolayer and DMOAP coated silica nanoparticles the tilt angles were 67.1° ± 4.3 and 46.0°± 4.0, respectively. Therefore, it means that the adsorption of DMOAP coated silica nanoparticles decreases the tilt angle since the surface anchoring of LC is more likely homeotropic comparing with the -COOH-terminated and COOH/DMOAP mixed monolayer coated silica nanoparticles. On the other hand, when the effect of -COOH-terminated silica nanoparticle adsorption on the LC orientation was analyzed by considering the change in the tilt angle of LC molecules in the case of LC- pure water interface, we did not observe any significant change in the tilt angle caused by the adsorption of nanoparticles. The reason behind this was reasoned that the adsorption of COOH-terminated silica nanoparticles, which have planar surface anchoring, onto the LC-water interface, which already has planar anchoring, without causing any change on LC orientation.

Recently, it has been shown that low-level concentrations of aqueous soluble species, in the range of ppb, could be detected by using nanoparticle-assisted LC droplet-based sensors[58]. Therefore, high sensitivity could be provided by using confined LC. In our study, in addition to the analysis of the response of LC confined in microwells against the adsorption of nanoparticles whose surfaces were functionalized to adjust the surface anchoring, it was also possible to get the response against the existence of chemicals which were carried by the nanoparticles. For this purpose, we used a dye molecule, which was methyl orange (MO), as a model molecule to adsorb on the surface of the nanoparticles and analyzed the response of the LC confined in the microwells with respect to the concentration of the dye molecules. Figure 4.44b showed the change in the tilt angle after the adsorption of silica nanoparticles carrying MO with different concentration to the LC-water interface. It can be seen

that when the concentration of dye molecules on the surface of DMOAP coated silica nanoparticles increased up to 1 ppb MO, the tilt angle of LC molecules at the interface of LC-water was increased from $46.0°\pm 4.0$ to $75.9°\pm 0.7$. In the case of low concentrations of MO which was around 0.01 to 0.1 ppb, there was no significant change in tilt angle but when the concentration of MO increased to 1 ppb the tilt angle reached to almost the same value with LC-water interface which has planar surface anchoring ($p>0.05$). This implies that there was a threshold in dye concentration beyond which we could not observe the significant change in the tilt angle without reaching a certain concentration and the reason for this transition concentration was likely directly related to the surface coverage of the particles. Therefore, all these results indicated that the phenomena occurred at the interface of LC confined within the microwell can be easily detected using optical methods and converted into numerical data and thus it can also be used as a sensor relying on the adsorption of molecules even if in the range of ppb and colloids having specific surface property.
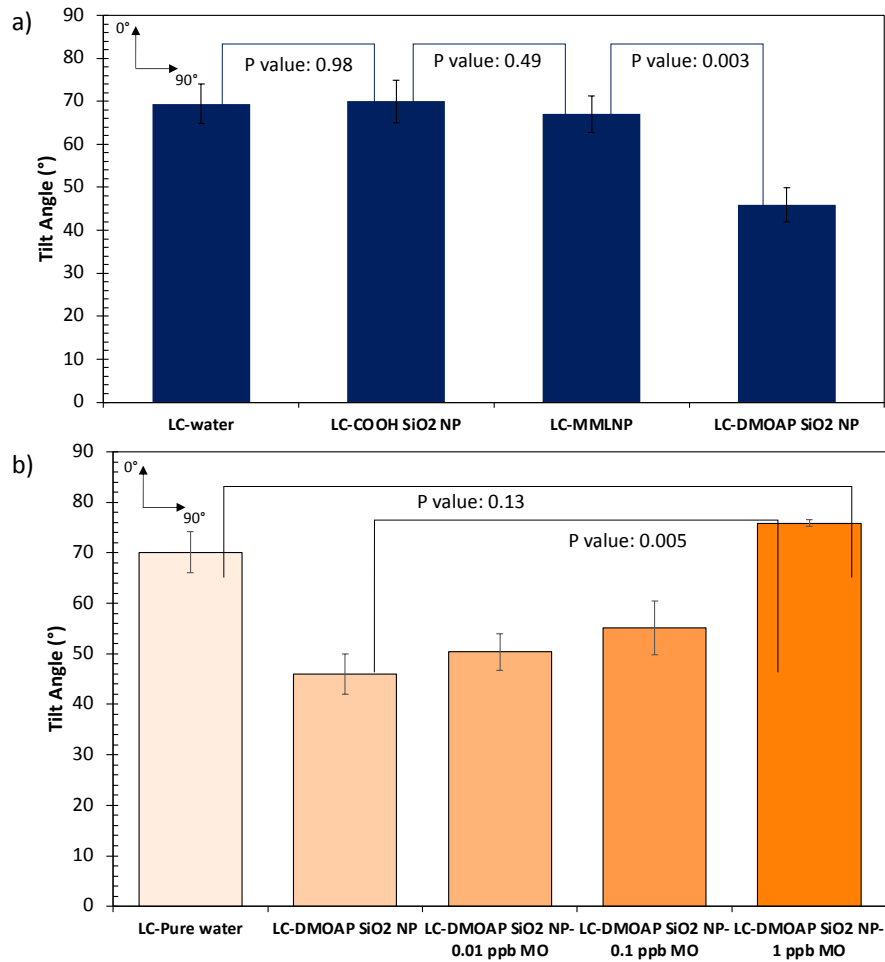
Figure 4.44 Tilt angles calculated from optical retardance in the case of a) adsorption of -COOH-terminated, COOH/DMOAP mixed monolayer coated and DMOAP coated silica nanoparticles. b) adsorption of DMOAP coated silica nanoparticles with MO concentration of 0.01, 0.1, 1 ppb (pH:5.0). The definition of the angles represented with arrows.

In order to display the assemblies of the nanoparticles that adsorbed on the LC-water interface, we adsorbed fluorescent labeled silica nanoparticles (FITC-SiNPs) on 5CB filled epoxy microwells in aqueous medium. As a preliminary result, when the FITC-SiNPs were adsorbed on LC-water interface and analyzed under fluorescence confocal polarized microscope, it was seen that nanoparticles were located with respect to the LC orientation. The patterns of the nanoparticles were consistent with

the LC configuration determined by using the method with polarized optical microscope. As seen in Figure 4.45, FITC-SiNPs were adsorbed on the positions along the LC orientation which was determined previously by using POM. It is known that the surface anchoring on bare silica nanoparticles is planar anchoring and also the anchoring on LC-water interface is planar anchoring. The assemblies of the nanoparticles on the LC-water interface might be created because of the elasticity. The reason of this behavior is that the size of the silica nanoparticles was around 400 nm and the size of the aggregates might be much more, so for this size range the elastic interactions play a dominant role in determining the overall interactions of the colloidal species. In order to perform a control experiment, we repeated the same experiment with the silica nanoparticles with the size of 100 nm instead of 400 nm (Figure 4.46). At the end of this experiment, we could not observe a pattern of the nanoparticle assemblies on LC-water interface. Therefore, it can be said that the nanoparticle assemblies shown in Figure 4.45, caused by the elastic interactions of nanoparticles because the pattern of adsorbed nanoparticles seen in the case of 400 nm could not be seen in the case of 100 nm nanoparticles since the influence of elastic interactions became less, the patterns could not be observed.
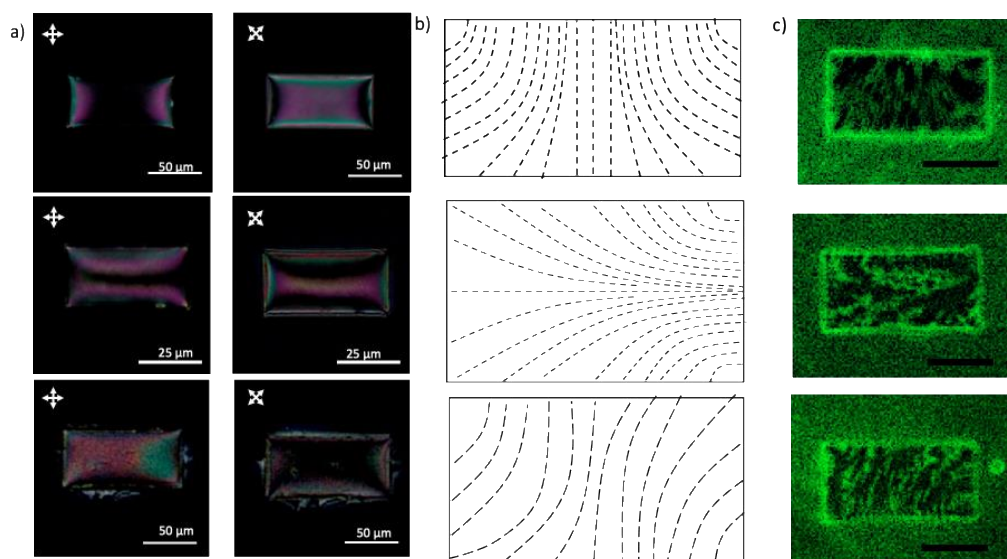
Figure 4.45 a) POM images of 5CB filled epoxy microwells in the case of medium of UP water, b) schematics of configuration of LC confined in epoxy microwells c)

images of 5CB filled epoxy microwells after the adsorption of FITC labeled silica nanoparticles at LC- water interface (Scale bar: 25 μm)
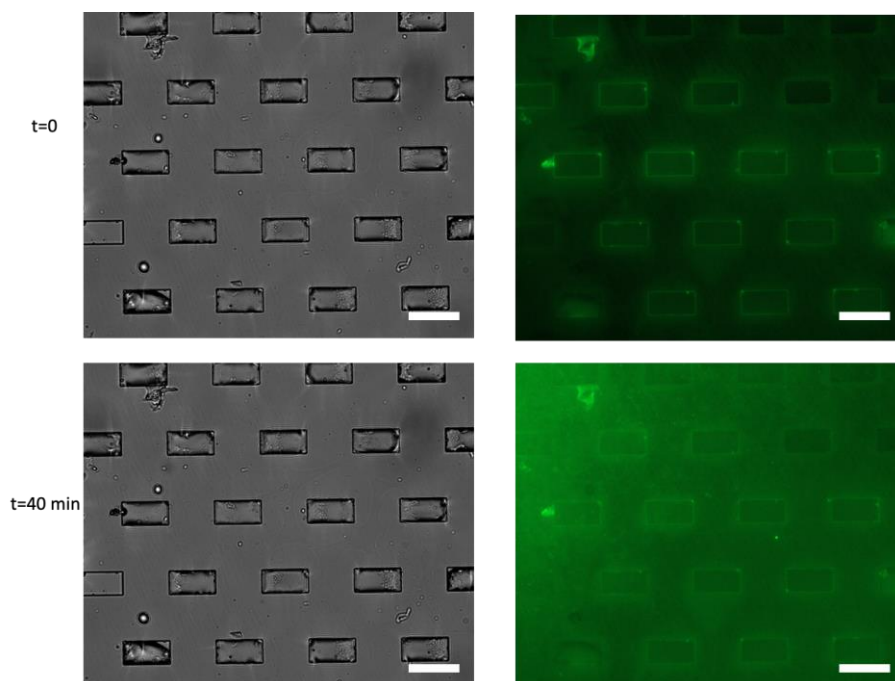
Figure 4.46 Bright field and FCPM images of 5CB filled epoxy microwells in the case of 100 nm FITC labeled silica nanoparticle adsorption (Scale bar: 50 μm)

Lastly, we conducted some analysis to investigate the configuration of 5CB within microwells in dynamic systems, in addition to studies conducted in static systems. For this purpose, we worked on creating microfluidic systems to understand how the orientation of 5CB changes in response to water flow and to examine these alterations under a polarized optical microscope as shown in Figure 4.47.In this system, the filling process of LC was different from the stationary form. In this case, 5CB flowed through the channel with a specified pressure and after the flow of 5CB, water flowed through the same channel, thereby removing the excess 5CB from the environment. Then by adjusting the pressure through the channel during the water flow, a shear stress was created and LC orientation with respect to this stress was monitored by capturing the images under polarized optical microscope. As illustrated in Figure 4.47, when the flow rate of the water was 1.5μl/min, a discernible variation

in the color of the microwells was evident, implying differences in the orientation or thickness of 5CB within these microwells. Conversely, when we increased the flow rate of water to 5μl/min, the microwells exhibited a more uniform appearance, with 5CB orientation appearing consistent across all microwells. This uniform appearance of the microwells with the increase of the flow rate also revealed that the microwells maintained their stability under flow and thus applied shear. Upon closer analysis of the images, it became apparent that the 5CB alignment followed the direction of water flow, as indicated by brightness at the upper and lower edges, while the middle remains dark under polarized optical microscopy. This observation aligned with the expectation that the surface anchoring of the microwell was not planar. These results indicated that dynamic analysis can be conducted at the LC-aqueous interface by integration LC confined within a microwell into flow containing systems, suggesting potential applications in sensor or diffusion analysis for various analyte.
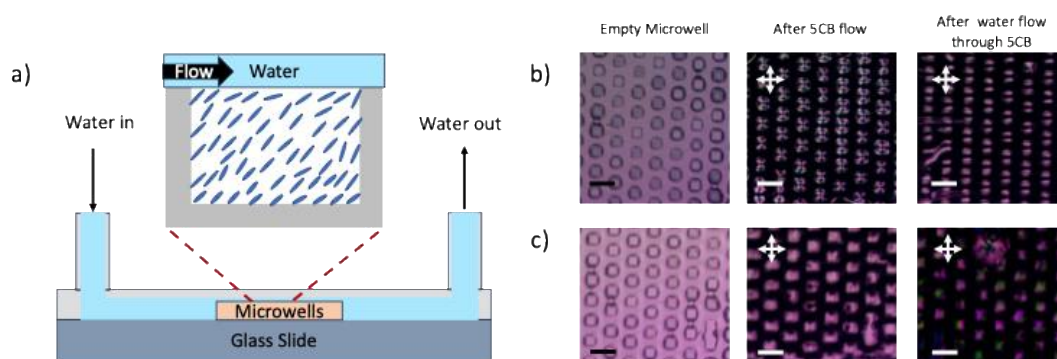
Figure 4.47 a) Schematic of the set up used for the dynamic analysis, Images of LC filled square shaped epoxy microwells in millifluidic systems under polarized optical microscope in the case of b) 5μl/ min and c) 1.5μl/ min. Scale bar:100μm

CHAPTER 5

CONCLUSION

In this study, in order to obtain the response to nanomaterials, we used LC droplets and microwells as confined systems and investigate the change in LC configuration in these systems.

Firstly, we used functionalized gold nanoparticles as a model to investigate the interparticle and LC-nanoparticle interactions at the LC-aqueous interface. We employed an LC emulsion as a confined system to provide a platform for the adsorption of gold nanoparticles. We analyzed change in the droplet configuration with respect to the adsorption of functionalized gold nanoparticles and adjusting the parameters selected by considering the interparticle interactions which are van der Waals, electrostatic and elastic interactions. We found that the dominant mechanisms that affect the LC droplet configuration with the time were the additional adsorption and the movement of nanoparticles at LC-water interfaces and these mechanisms were directly dependent on the surface properties of nanoparticles. Utilizing the LC droplet as a confined system provided the advantage of acquiring extensive data in a single experiment, while simultaneously enabling the observation of nanoparticle adsorption via a standard polarized microscope, all without the necessity of any labeling. In future studies, preventing aggregation could make the impact of the anchoring properties on the particle surface more discernible, thereby improving the ability to distinguish particles functionalized through various methods. In this regard, a novel approach could be developed that not only enables precise detection but also facilitates the advanced classification of nanoparticles based on their surface properties.

In the second part of this study, we aimed to develop a method to determine LC configuration in specified geometries to use this method for preparation of a platform for the analysis on NP-NP an NP-LC interactions. We prepared microwells

made from PVA with the shapes of a circle, square, triangle, rectangle, and star in the size range of 10-100 μm. Then, we determined the LC configuration and defect positions within these microwells in the case of LC-air interface. Determination of LC configuration, and in particular the defect positions, is crucial for a wide range of applications where LCs are used as templates. Due to the energy gap associated with defects, it becomes possible to adsorb colloids and molecules onto defect regions, enabling the assembly of desired structures. This capability holds substantial relevance for a wide array of biological and optical applications. We employed this method in the context of this thesis to determine the LC configuration; however, this approach is also applicable for the fabrication of polymeric particles with a pre-determined internal structure[109]. The ability to fabricate such particles opens avenues for robotic applications, where they can exhibit directional motion, as well as for on-demand release mechanisms and drug delivery systems, enabled by their anisotropic structures. Furthermore, the method developed in this study paves the way for exploring more complex defect structures through the use of cholesteric LCs, rather than nematic phases, in future investigations, thereby advancing knowledge in this field.

In the third part of this study, to confine LC in specified geometries and analyze the LC configuration in aqueous medium, we prepared water insoluble, stable microwells by using epoxy the size range of 10-100 μm. Under a polarized optical microscope, the LC orientation within microwells, interfacial tilting and defect formation were analyzed. Using SDS molecules as a model analyte, a deviation in interfacial tilting was created and metastable configurations with disclination lines and point defects as defect structures were formed based on the interfacial anchoring which can be related directly with SDS concentration. To convert color changes into numerical data and achieve a quantitative transformation of qualitative variations in LC orientation, retardation values were acquired for each case using the Michel-Lévy Chart. Consequently, the relationship between tilt angle and the colors observed in images captured under a polarized optical microscope was established. This correlation enables the potential utilization of this system in sensor applications.

Additionally, we investigated the change in LC configuration caused by the adsorption of silica nanoparticles functionalized with silane and dye molecules. We showed that variations in tilting at the LC-aqueous interface could be used to detect dye concentrations on the nanoparticle surface, which were in the range of ppb, showing that this platform is highly sensitive and stable for sensor applications based on LCs, enabling precise detection in aqueous environments. The platform developed in this study not only gave response to adsorption of colloids with distinct surface properties but also facilitates the detection of molecules at remarkably low concentrations. As such, this work opens new avenues for the development of advanced sensor technologies capable of detecting species such as viruses, as well as a wide range of chemical compounds. In addition, we visualized the self-assemblies of FITC-doped silica nanoparticles adsorbed on the LC-water interfaces by using FCPM and found that the nanoparticles were adsorbed in a manner that followed the LC configuration we had previously determined using optical microscopy. This finding has considerable significance, as it highlights the precise control over the arrangement of nanoparticles in a desired pattern. This method holds significant potential for optical applications and may also offer considerable benefits in various biological contexts. For instance, nanoparticles functionalized with drugs could be targeted to specific regions, or gold nanoparticles could be employed in photothermal therapy, enabling precise targeting for therapeutic purposes. Lastly, we investigated 5CB configuration within the microwells in dynamic systems, distinct from the studies conducted in static systems. As a proof of concept, we used millifluidic systems to understand how the orientation of 5CB changes in response to water flow and to examine these alterations under a polarized optical microscope. It was illustrated that stability can be maintained under flow conditions, and a more uniform distribution of the LC configuration can be obtained benefiting from the shear induced by the flow. Therefore, this work can be further expanded by developing lab-on-a-chip platforms using flow-based systems, such as microchannels, to detect various analytes and perform diffusion analysis.

REFERENCES

1   Malik, S., Muhammad, K., & Waheed, Y., *Molecules,* 2023, **28**, 661.

2   N. Baig, I. Kammakakam, W. Falath and I. Kammakakam, *Mater. Adv.*, 2021, **2**, 1821–1871.

3   N. Joudeh and D. Linke, *J. Nanobiotechnology*, 2022, **20**, 1–29.

4   N. I. Hulkoti and T. C. Taranath, *Colloids Surfaces B Biointerfaces*, 2014, **121**, 474–483.

5   I. Khan, K. Saeed and I. Khan, *Arab. J. Chem.*, 2019, **12**, 908–931.

6   P. Holister, J.-W. Weener, C. R. Vas, T. Harper and Cientifica, *Científica*, 2003, 11.

7   N. B. Singh, B. Kumar, U. L. Usman and M. A. B. H. Susan, *Nano-Structures and Nano-Objects*, 2024, **39**, 101299.

8   Y. C. Lu, Z. Xu, H. A. Gasteiger, S. Chen, K. Hamad-Schifferli and Y. Shao-Horn, *J. Am. Chem. Soc.*, 2010, **132**, 12170–12171.

9   K. Ganesh and D. Archana, *Am. J. Adv. Drug Deliv.*, 2013, **3**, 196–215.

10   W. J. Stark, P. R. Stoessel, W. Wohlleben and A. Hafner, *Chem. Soc. Rev.*, 2015, **44**, 5793–5805.

11   M. Segev-Bar and H. Haick, *ACS Nano*, 2013, **7**, 8366–8378.

12   E. Bukusoglu, M. Bedolla Pantoja, P. C. Mushenheim, X. Wang and N. L. Abbott, *Annu. Rev. Chem. Biomol. Eng.*, 2016, **7**, 163–196.

13   N. A. Lockwood and N. L. Abbott, *Curr. Opin. Colloid Interface Sci.*, 2005, **10**, 111–120.

14   J. M. Brake and N. L. Abbott, *Langmuir*, 2002, **18**, 6101–6109.

15   C. S. Mullin, P. Guyot-Sionnest and Y. R. Shen, *Phys. Rev. A*, 1989, **39**, 3745–3747.

16   T. Murashige, H. Fujikake, H. Sato, H. Klkuchi, T. Kurita and F. Sato,

Japanese J. Appl. Physics, Part 1 Regul. Pap. Short Notes Rev. Pap., 2005, **44**, 1862–1866.

17   A. Karausta and E. Bukusoglu, *ACS Appl. Mater. Interfaces*, 2018, **10**, 33484–33492.

18   X. Wang, Y. K. Kim, E. Bukusoglu, B. Zhang, D. S. Miller and N. L. Abbott, *Phys. Rev. Lett.*, 2016, **116**, 1–5.

19   D. S. T. Duong & C. H. Jang, C. H. , 2023, *Microchimica Acta*, **190**(4), 122.

20   D. S. Miller, R. J. Carlton, P. C. Mushenheim and N. L. Abbott, *Langmuir*, 2013, **29**, 3154–3169.

21   M. Kleman and O. D. Lavrentovich, *Philos. Mag.*, 2006, **86**, 4117–4137.

22   O. D. Lavrentovich, *Liq. Cryst.*, 1998, **24**, 117–126.

23   I. Dierking and P. Archer, *RSC Adv.*, 2013, **3**, 26433–26437.

24   W. Iglesias, N. L. Abbott, E. K. Mann and A. Jákli, *ACS Appl. Mater. Interfaces*, 2012, **4**, 6884–6890.

25   Q. Z. Hu and C. H. Jang, *Colloids Surfaces B Biointerfaces*, 2011, **88**, 622–626.

26   Y. Choi, D. Choi, J.-K. Choi, K.-S. Oh, E. Cho, J.-H. Im, D. P. Singh and Y.-K. Kim, *ACS Appl. Opt. Mater.*, 2023, **1**, 1879–1897.

27   N. A. Lockwood, J. K. Gupta and N. L. Abbott, *Surf. Sci. Rep.*, 2008, **63**, 255–293.

28   X. Yao, H. Zhang and J. Z. Y. Chen, *Phys. Rev. E*, 2018, **97**, 1–14.

29   K. Katayama, T. Yoshimura, S. Yamashita, H. Teratani, T. Murakami, H. Suzuki and J. I. Fukuda, *Soft Matter*, 2023, **19**, 6578–6588.

30   D. S. Kim, S. Čopar, U. Tkalec and D. K. Yoon, *Sci. Adv.*, 2018, **4**, 1–8.

31   M. Rahimi, T. F. Roberts, J. C. Armas-Pérez, X. Wang, E. Bukusoglu, N. L. Abbott and J. J. De Pablo, *Proc. Natl. Acad. Sci. U. S. A.*, 2015, **112**, 5297–5302.

32   M. A. Gharbi, M. Nobili and C. Blanc, *J. Colloid Interface Sci.*, 2014, **417**, 250–255.

33   F. Mondiot, X. Wang, J. J. De Pablo and N. L. Abbott, *J. Am. Chem. Soc.*, 2013, **135**, 9972–9975.

34   J. K. Gupta, S. Sivakumar, F. Caruso and N. L. Abbott, *Angew. Chemie - Int. Ed.*, 2009, **48**, 1652–1655.

35   X. Wang, E. Bukusoglu, D. S. Miller, M. A. Bedolla Pantoja, J. Xiang, O. D. Lavrentovich and N. L. Abbott, *Adv. Funct. Mater.*, 2016, **26**, 7343–7351.

36   D. S. Miller, X. Wang and N. L. Abbott, *Chem. Mater.*, 2014, **26**, 496–506.

37   A. Akman and E. Bukusoglu, *J. Colloid Interface Sci.*, 2023, **649**, 772–784.

38   S. Şengül, N. Aydoğan and E. Bukusoglu, *J. Colloid Interface Sci.*, 2022, **608**, 2310–2320.

39   H. S. Yun, Z. C. Meijs, G. Park, Y. Fu, L. Isa and D. K. Yoon, *J. Colloid Interface Sci.*, 2023, **645**, 115–121.

40   X. Wang, D. S. Miller, J. J. De Pablo and N. L. Abbott, *Soft Matter*, 2014, **10**, 8821–8828.

41   E. Bukusoglu, X. Wang, Y. Zhou, J. A. Martínez-González, M. Rahimi, Q. Wang, J. J. De Pablo and N. L. Abbott, *Soft Matter*, 2016, **12**, 8781–8789.

42   S. Zhong and C. H. Jang, *Soft Matter*, 2015, **11**, 6999–7004.

43   R. J. Carlton, J. T. Hunter, D. S. Miller, R. Abbasi, P. C. Mushenheim, L. N. Tan and N. L. Abbott, *Liq. Cryst. Rev.*, 2013, **1**, 29–51.

44   M. Khan and S. Y. Park, *Anal. Chem.*, 2014, **86**, 1493–1501.

45   R. R. Shah and N. L. Abbott, *Science (80-.).*, 2001, **293**, 1296–1299.

46   S. M. Malone and D. K. Schwartz, *Langmuir*, 2011, **27**, 11767–11772.

47   J. T. Hunter and N. L. Abbott, *Sensors Actuators, B Chem.*, 2013, **183**, 71–80.

48   J. T. Hunter, S. K. Pal and N. L. Abbott, *ACS Appl. Mater. Interfaces*, 2010, **2**, 1857–1865.

49   J. Uchida, B. Soberats, M. Gupta and T. Kato, *Adv. Mater.*, 2022, **34**, 1–33.

50   M. Nikkhou, M. Škarabot, S. Čopar, M. Ravnik, S. Žumer and I. Muševč, *Nat. Phys.*, 2015, **11**, 183–187.

51   H. K. Bisoyi and Q. Li, *Chem. Rev.*, 2022, **122**, 4887–4926.

52   W. Feng, D. J. Broer and D. Liu, *Adv. Funct. Mater.*, , DOI:10.1002/adfm.201901681.

53   A. Ryabchun, F. Lancia and N. Katsonis, *ACS Appl. Mater. Interfaces*, 2021, **13**, 4777–4784.

54   J. Kim, M. Khan and S. Y. Park, *ACS Appl. Mater. Interfaces*, 2013, **5**, 13135–13139.

55   Z. Wang, T. Xu, A. Noel, Y. C. Chen and T. Liu, *Soft Matter*, 2021, **17**, 4675–4702.

56   J. A. Moreno-Razo, E. J. Sambriski, N. L. Abbott, J. P. Hernández-Ortiz and J. J. De Pablo, *Nature*, 2012, **485**, 86–89.

57   S. He, W. Liang, C. Tanner, K. L. Cheng, J. Fang and S. T. Wu, *Anal. Methods*, 2013, **5**, 4126–4130.

58   S. Sezer and E. Bukusoglu, *Langmuir*, 2023, **40**, 2783–3274.

59   Y. K. Kim, X. Wang, P. Mondkar, E. Bukusoglu and N. L. Abbott, *Nature*, 2018, **557**, 539–544.

60   G. Park, A. Suh, H. Zhao, C. Lee, Y. S. Choi, I. I. Smalyukh and D. K. Yoon, *Adv. Mater.*, 2022, **34**, 1–10.

61   Y. Guo, S. Afghah, J. Xiang, O. D. Lavrentovich, R. L. B. Selinger and Q. H. Wei, *Soft Matter*, 2016, **12**, 6312–6320.

62   X. Wang, D. S. Miller, J. J. De Pablo and N. L. Abbott, *Soft Matter*, 2014, **10**, 8821–8828.

63   D. S. Kim, S. Čopar, U. Tkalec and D. K. Yoon, *Sci. Adv.*, 2018, **4**, 1–9.

64   C. K. Chang, C. M. W. Bastiaansen, D. J. Broer and H. L. Kuo, *Adv. Funct. Mater.*, 2012, **22**, 2855–2859.

65   X. Wang, E. Bukusoglu, D. S. Miller, M. A. Bedolla Pantoja, J. Xiang, O. D. Lavrentovich and N. L. Abbott, *Adv. Funct. Mater.*, 2016, **26**, 7343–7351.

66   W. Feng, D. J. Broer and D. Liu, *Adv. Mater.*, 2018, **1704970**, 1704970.

67   K. Bagchi, T. Emeršič, J. A. Martínez-González, J. J. de Pablo and P. F. Nealey, *Sci. Adv.*, 2023, **9**, 1–15.

68   S. Xie, R. He, Q. Zhu, M. Jin, R.Yang, S. Shen, ... & Shui, L. *Colloids and Surfaces A: Physicochemical and Engineering Aspect*s, 2022, 644, 128728.

69   J. K. Whitmer, X. Wang, F. Mondiot, D. S. Miller, N. L. Abbott and J. J. De Pablo, *Phys. Rev. Lett.*, 2013, **111**, 1–5.

70   W. Khan, J. H. Choi, G. M. Kim and S. Y. Park, *Lab Chip*, 2011, **11**, 3493–3498.

71   X. Wang, E. Bukusoglu and N. L. Abbott, *Chem. Mater.*, 2017, **29**, 53–61.

72   J. Zhou, Y. Dong, Y. Zhang, D. Liu, & Z. Yang,. *Nanomaterials*, 2016, **6**, 229.

73   E. Kurt and E. Bukusoglu, *Soft Matter*, 2022, **18**, 4009–4016.

74   D. Hartono, C. Y. Xue, K. L. Yang and L. Y. L. Yung, *Adv. Funct. Mater.*, 2009, **19**, 3574–3579.

75   K. J. Kek, J. J. Z. Lee, Y. Otono and S. Ishihara, *J. Soc. Inf. Disp.*, 2017, **25**, 366–373.

76   X. Ding and K. L. Yang, *Sensors Actuators, B Chem.*, 2012, **173**, 607–613.

77   M. A. Gharbi, M. Nobili and C. Blanc, *Journal of colloid and interface science,* 2014, **417**, 250-255.

78   J. K. Gupta, J. S. Zimmerman, J. J. De Pablo, F. Caruso and N. L. Abbott, *Langmuir*, 2009, **25**, 9016–9024.

79 X. Wang, Y. Zhou, Y. K. Kim, D. S. Miller, R. Zhang, J. A. Martinez-Gonzalez, E. Bukusoglu, B. Zhang, T. M. Brown, J. J. De Pablo and N. L. Abbott, *Soft Matter*, 2017, **13**, 5714–5723.

80 M. J. Shin, M. J. Gim and D. K. Yoon, *Langmuir*, 2018, **34**, 2551–2556.

81 G. Durey, Y. Ishii and T. Lopez-Leon, *Langmuir*, 2020, **36**, 9368–9376.

82 O. D. Lavrentovich and Y. U. Nastishin, *Epl*, 1990, **12**, 135–141.

83 I. Chuang, R. Durrer, N. Turok and B. Yurke, *Science (80-.).*, 1991, **251**, 1336–1342.

84 N. Kumar, R. Zhang, J. J. de Pablo and M. L. Gardel, *Science Advances*, 2018, **4**, 1–13.

85 X. Wang, D. S. Miller, E. Bukusoglu, J. J. De Pablo and N. L. Abbott, *Nat. Mater.*, 2015, **15**, 1–9.

86 I. Muševič, M. Škarabot, U. Tkalec, M. Ravnik and S. Žumer, *Science (80-.).*, 2006, **313**, 954–958.

87 G. M. Koenig, I. H. Lin and N. L. Abbott, *Proc. Natl. Acad. Sci. U. S. A.*, 2010, **107**, 3998–4003.

88 F. Mukherjee, A. Shi, X. Wang, F. You and N. L. Abbott, 2022, 1–15.

89 S. Zhong and C. H. Jang, *Soft Matter*, 2015, **11**, 6999–7004.

90 Z. Rouhbakhsh, A. Verdian and G. Rajabzadeh, *Talanta*, 2020, **206**, 120246.

91 Z. Yang and N. L. Abbott, *Langmuir*, 2010, **26**, 13797–13804.

92 X. H. Zhang and W. Ducker, *Langmuir*, 2008, **24**, 110–115.

93 P. Dhara and R. Mukherjee, *J. Phys. Chem. B*, 2020, **124**, 1293–1300.

94 Y. An, M. Chen, Q. Xue and W. Liu, *J. Colloid Interface Sci.*, 2007, **311**, 507–513.

95 J. Kimling, M. Maier, B. Okenve, V. Kotaidis, H. Ballot and A. Plech, *J. Phys. Chem. B*, 2006, **110**, 15700–15707.

96   K. D. Comeau and M. V. Meli, *Langmuir*, 2012, **28**, 377–381.

97   C. D. Bain and G. M. Whitesides, *J. Am. Chem. Soc.*, 1989, **111**, 7164–7175.

98   V. Velachi, D. Bhandary, J. K. Singh and M. N. D. S. Cordeiro, *J. Phys. Chem. C*, 2015, **119**, 3199–3209.

99   X. Wang, E. Bukusoglu and N. L. Abbott, *Chem. Mater.*, 2017, **29**, 53–61.

100   J. Marczak, M. Kargol, M. Psarski and G. Celichowski, *Appl. Surf. Sci.*, 2016, **380**, 91–100.

101   S. Baczyński, P. Sobotka, K. Marchlewicz, M. Słowikowski, M. Juchniewicz, A. Dybko and K. A. Rutkowska, *Applied Sciences*, 2021, **24**, 11593.

102   W. Zheng and Y. T. Hu, *Liq. Cryst.*, 2016, **43**, 327–335.

103   D. Cortese, J. Eggers and T. B. Liverpool, *Phys. Rev. E*, 2018, **97**, 1–10.

104   H. Yoshida, K. Asakura, J. Fukuda and M. Ozaki, *Nat. Commun.*, 2015, **6**, 7180.

105   I. Dierking, M. Ravnik, E. Lark, J. Healey, G. P. Alexander and J. M. Yeomans, *Phys. Rev. E - Stat. Nonlinear, Soft Matter Phys.*, 2012, **85**, 1–11.

106   M. Nikkhou, M. Škarabot and I. Mušević, *Phys. Rev. E*, 2016, **93**, 1–9.

107   J. K. Gupta and N. L. Abbott, *Langmuir*, 2009, **25**, 2026–2033.

108   J. M. Brake, A. D. Mezera and N. L. Abbott, *Langmuir*, 2003, **19**, 8611–9096.

109   A. Karausta, C. Kocaman and E. Bukusoglu, *J. Mol. Liq.*, 2021, **324**, 36–38.

APPENDICES

## A. Contact Angle Measurement of DMOAP Coated Epoxy Films

Epoxy films were prepared and contact angle of 5CB and water was measured by using DataPhysics OCA 200 model goniometer in the case of 5CB-air and 5CB-water interfaces.
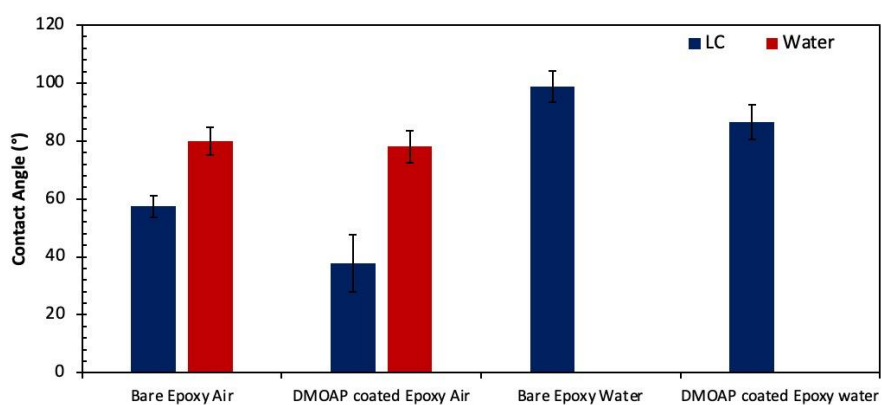
Appendix A.1 Contact Angle of UP water and LC (5CB) on bare and DMOAP coated epoxy surfaces

## B. Calculation of Tilt Angle of 5CB on Epoxy Surface

Sandwich cells were prepared with DMOAP coated glass slide and epoxy films. Then, polarized optical microscope images were taken with bright field, polarized light and by using conoscopic (Bertrand) lens. Then, deviation from the strongly homeotropic anchoring was calculated by comparing the cross with one perfectly located at the center.
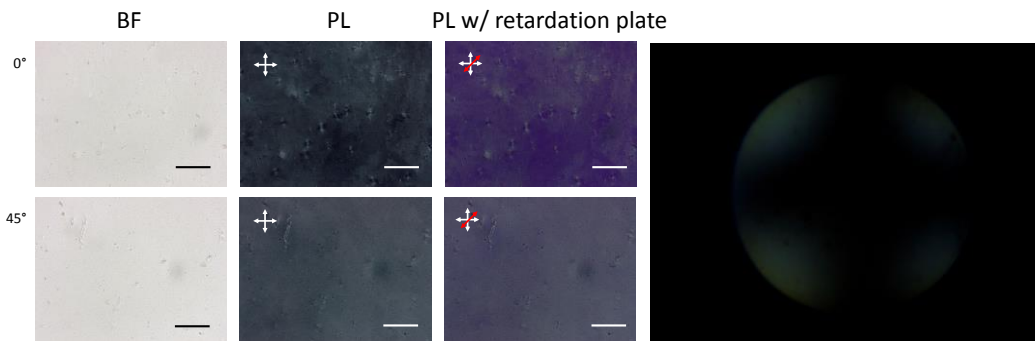
Appendix B.1 a) POM images of LC filled sandwich cells made with DMOAP coated glass slides and flat film of epoxy, b) cross obtained by using Bertrand lens. Arrows indicate the direction of the polarization of the polarizer and analyzer. Scale bar: 20 μm

C. Configuration of 5CB Confined in PDMS Microwells

In order to analyze the effect of surface anchoring on the configuration of 5CB, we prepared PDMS microwells because the surface anchoring of 5CB is homeotropic different from epoxy microwells. The configuration of 5CB was determined by analyzing the images of PDMS microwells filled with 5CB taken under polarized optical microscope in the case of the interfaces with air, pure water and SDS solution.
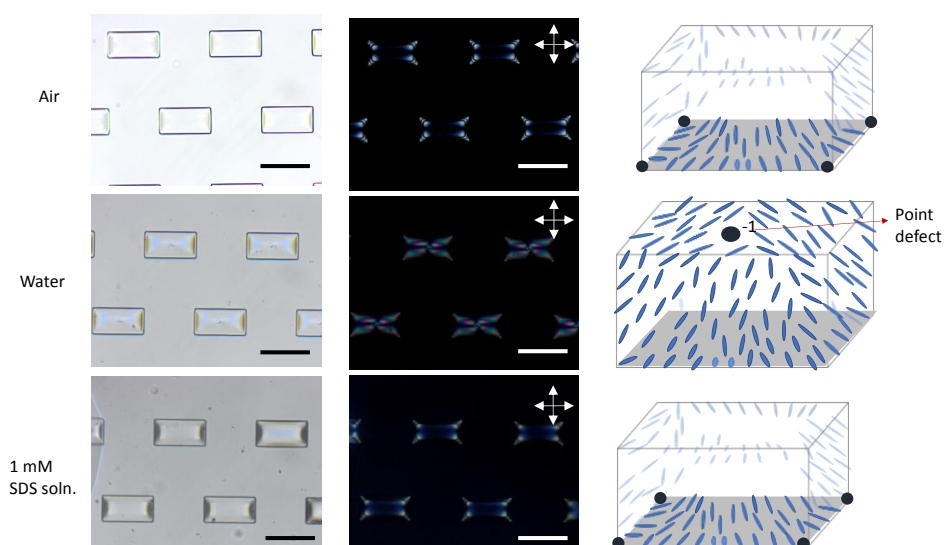
Appendix C.1 Optical microscope images of LC filled PDMS microwells in the case of LC-air, LC-water and LC-1 mM SDS solution and schematics of LC orientation in these microwells Arrows indicate the direction of the polarization of the polarizer and analyzer. Scale bars: 100 μm

## D. Determination of Surface Anchoring of 5CB on Surface of Epoxy Film

A sandwich cell was prepared by using DMOAP coated glass slide and DMOAP coated epoxy film and filled with 5CB and analyzed under polarized optical microscope. The orientation of the cross polarizers was changed and it was seen there was no significant change in appearance under cross polarizers which meant that surface anchoring was close to homeotropic anchoring. Also, Bertrand lens was used to calculate the angle showing deviation from strong homeotropic anchoring and it was calculated as

Appendix D.1 a,b) Micrographs of sandwich cell of DMOAP coated glass slide and epoxy film filled with the mixture of RM257 and 5CB under polarized optical microscope and c) image taken with Bertrand lens. White arrows show the direction of polarizers.

E. Dependency of the Formation of Disclination Line Defects on SDS Concentration

The number of microwells having a configuration with disclination line defect was collected in the case of SDS addition and dilution.
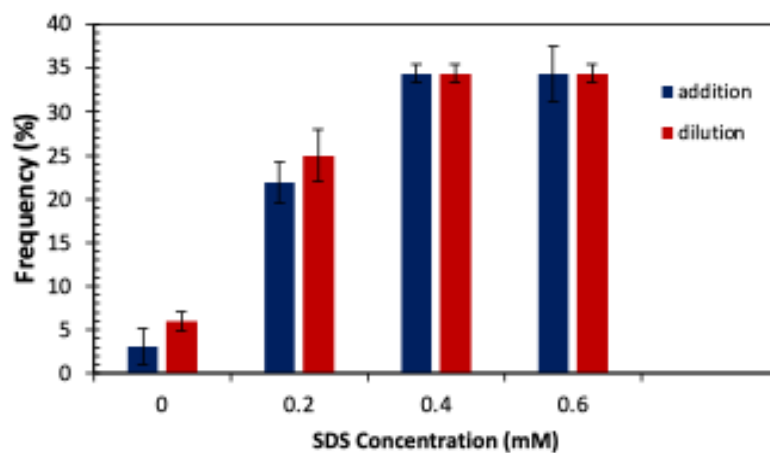
Appendix E.1 The frequency of the microwells having disclination line in the case of SDS addition and dilution

F. Dependency of the Formation of Disclination Line Defect on Microwell Size

The circular shaped microwells with the size of 50 and 100 µm was filled with 5CB and analyzed under polarized optical microscope.
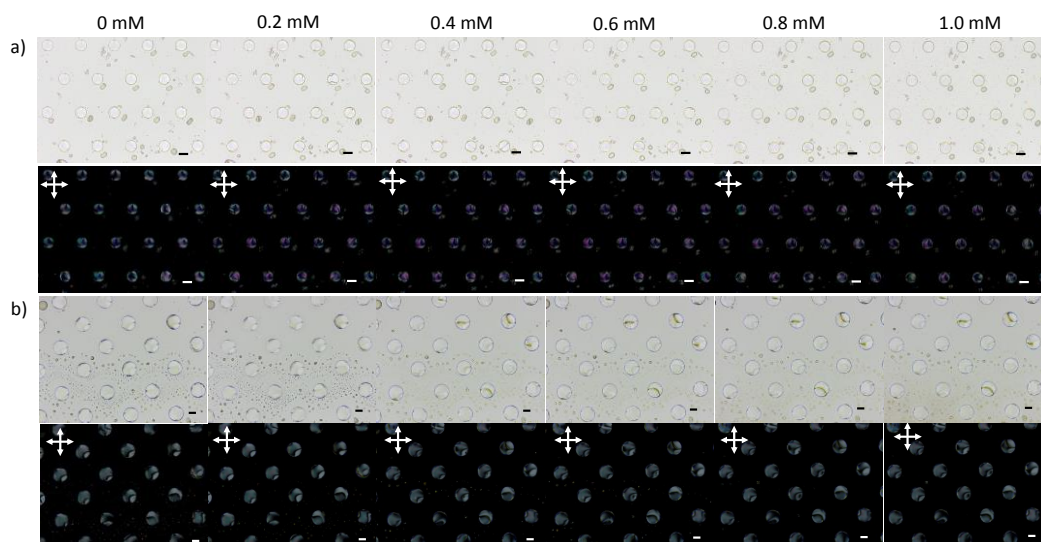
Appendix F.1 Brightfield and polarized light images of a) 50 µm and b) 100 µm circular shaped microwells during the SDS addition Scale bars: 50 µm

G. The effect of Nematic-Isotropic Transition to Configuration of 5CB Confined in Epoxy Microwell

The rectangular shaped epoxy microwells was filled with 5CB and heated to NI transition point. The configuration of the microwells were analyzed before and after NI transition to evaluate their stability.
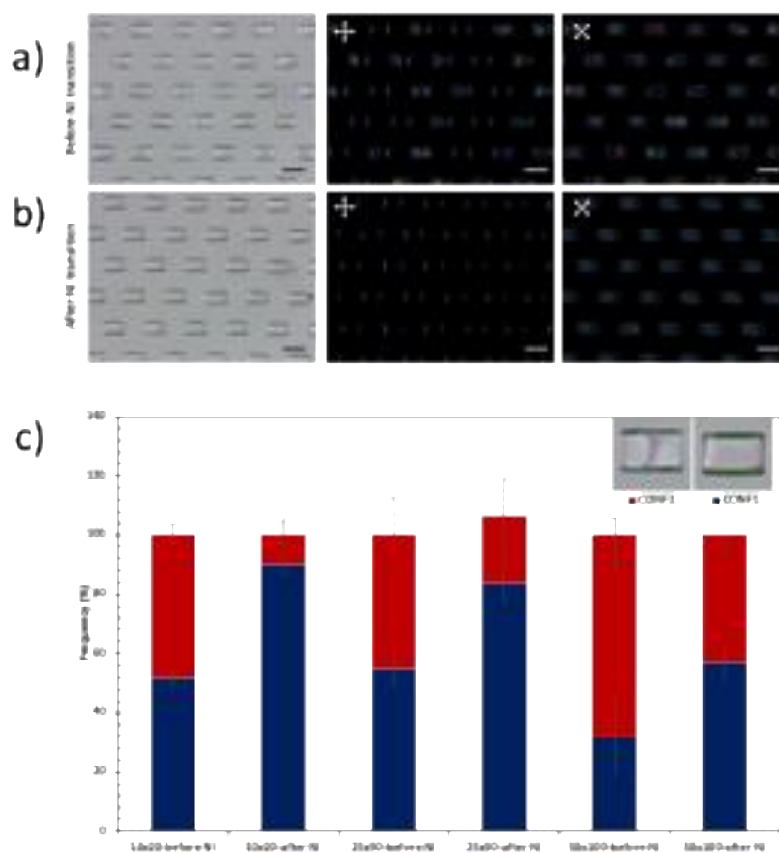
Appendix G.1 Polarized optical microscope images of LC filled rectangular epoxy microwells opened to air a) before NI transition, b) after NI transition, c) distribution of LC configuration in the case of microwells with the size of 10x20, 25x50 and 50x100 μm. Arrows indicate the direction of the polarization of the polarizer and analyzer. Scale bars: 100 μm

H. The Velocity of Point Defects with Opposite Charges During the Annihilation
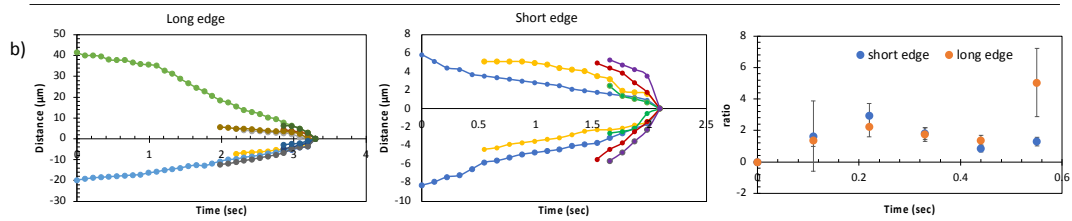
Appendix H.1 The graphs showing the distance traveled by the defects per unit time along the long edge and short edge and the ratio of the velocities of two defects that annihilate with respect to time

CURRICULUM VITAE

Surname, Name: Karausta, Aslı

EDUCATION

Degree	Institution	Year of Graduation
MS	METU Chemical Engineering	2018
BS	METU Chemical Engineering	2016
High School	Dr. Binnaz Ege-Dr. Rıdvan Ege Anatolian High School, Ankara	2011

FOREIGN LANGUAGES

Advanced English, Basic German

EXPERIENCES

- R&D Engineer, ASELSAN (07/2020- Present)
- Research & Teaching Assistant, Department of Chemical Engineering Middle East Technical University (01/2020 – 07/2020)
- Tübitak Project Assistant, Project No: 217M268 (2018-2020)

Internship:

- Limak Batı Cement, Ankara, Turkey (01-02/2016)
- TAI-Turkish Aerospace Industries Inc., Ankara, Turkey

Projects Accomplished in Classes:

- Design of Experiments (DOE) for Solar Panel Production
- Design of a Plug Flow Reactor
- Design of Maleic Anhydride Production Plant
- Design of an Indoor Pool Room

- Design of Methanol Reactor

PUBLICATIONS

1. Karausta, A., & Bukusoglu, E. (2018). Liquid Crystal-Templated Synthesis of Mesoporous Membranes with Predetermined Pore Alignment. ACS Applied Materials & Interfaces, 10(39), 33484-33492. doi:10.1021/acsami.8b14121

2. Karausta, A., Kocaman, C., & Bukusoglu, E. (2021). Controlling the shapes and internal complexity of the polymeric particles using liquid crystal-templates confined into microwells. Journal of Molecular Liquids, 324, 114710.

3. Karausta, A., & Büküşoğlu, E. (2021). Positioning of Cubic Shaped Particles with Different Edge Structures in Nematic Medium. Celal Bayar University Journal of Science, 17(2), 115-120.

CONFERENCES

1- "Liquid Crystal-Templated Synthesis of Anisotropic Ultrafiltration Membranes", 9th Eastern Mediterranean Chemical Engineering Conference (EMCC 9), Ankara, Turkey, September 2018 (Poster Presentation)

2- "Liquid Crystal- Templated Synthesis of Polymeric Films and their Potential Use in Chemical Processes", 27th International Liquid Crystal Conference (ILCC2018), Kyoto, Japan, July 2018 (Oral Presentation)